

2

AD-A267 268 PAGE

Form Approved
OMB No. 0704-0188

Public report on
gathering and
collection of
Davis Highway.



Open response, including the time for reviewing instructions, searching existing data sources, gathering and maintaining the data needed, completing and reviewing the collection of information, send comments regarding this burden estimate or any other aspect of this collection of information, including suggestions for reducing this burden, to Washington Headquarters Services, Directorate for Information Operations and Reports, 1215 Jefferson Road, Suite 1204, Paperwork Reduction Project (0704-0188), Washington, DC 20503

1. AGENCY USE ONLY (Leave blank)	2. REPORT DATE 7 May 1993	3. REPORT TYPE AND DATES COVERED Final Report August 1992-July 1993
----------------------------------	------------------------------	--

4. TITLE AND SUBTITLE (u)High Voltage Conductors in Spacecraft	5. FUNDING NUMBERS AFOSR-87-0340
---	-------------------------------------

6. AUTHOR(S) Daniel Hastings	AFOSR-TR- 88 0462
-------------------------------------	-------------------

7. PERFORMING ORGANIZATION NAME(S) AND ADDRESS(ES) MIT, Aeronautics and Astronautics 77 Massachusetts Avenue, Bldg. 37-451 Cambridge, MA 02139	8. PERFORMING ORGANIZATION REPORT NUMBER
---	---

9. SPONSORING / MONITORING AGENCY NAME(S) AND ADDRESS(ES) AFOSR/NA 110 Duncan Ave, Suite B115 Bolling AFB, DC 20332-0001	10. SPONSORING / MONITORING AGENCY REPORT NUMBER
---	---

DTIC
ELECTE
JUL 28 1993
S E D

11. SUPPLEMENTARY NOTES

12a. DISTRIBUTION / AVAILABILITY STATEMENT Approved for public release; distribution is unlimited.	93-16916
---	--------------

13. ABSTRACT (Maximum 200 words) Future solar arrays are being designed for much higher voltages in order to meet high power demands at low currents. Unfortunately, negatively biased high voltage solar cells have been observed to arc when exposed to the low earth orbit plasma environment. Analytical and numerical models of this arcing phenomenon on conventional solar cells have been developed which show excellent agreement with experimental data. With an understanding of a mechanism for arcing, it is possible to determine methods of arc rate mitigation and to predict arc rates for experiments. Using the previously developed models, it was determined that the arcing rate can be decreased by (1) increasing the interconnector work function, (2) increasing the thickness of the coverglass and adhesive, (4) decreasing the ratio of the coverglass/adhesive dielectric constants, and (5) overhanging the coverglass. Of these, methods (4) and (5) show the most promise in reducing or even eliminating arcing. In addition, arcing rates were predicted for the high voltage biased arrays of the Air Force's Photovoltaic and Space Power Plus Diagnostics experiment (PASP Plus) and NASA's Solar Array Module Plasma Interactions Experiment (SAMPIE). These predictions provide both expectations for the missions and a means to test the numerical and analytical models in the space environment for different solar cell technologies. Finally, a numerical model of the arc initiation process was also developed for wrap-through-contact cells, but experimental data is not available for comparison.
--

14. SUBJECT TERMS Arcing, high voltage solar array	15. NUMBER OF PAGES 90
---	---------------------------

16. PRICE CODE

17. SECURITY CLASSIFICATION OF REPORT Unclassified	18. SECURITY CLASSIFICATION OF THIS PAGE Unclassified	19. SECURITY CLASSIFICATION OF ABSTRACT Unclassified	20. LIMITATION OF ABSTRACT UL
--	---	--	----------------------------------

DTIC QUALITY INSPECTED 5

Accession For	
NTIS	CRA&I <input checked="" type="checkbox"/>
DTIC	TAB <input type="checkbox"/>
Unannounced <input type="checkbox"/>	
Justification	
By	
Distribution /	
Availability Codes	
Dist	Avail and/or Special
A-1	

**ARCING MITIGATION AND PREDICTIONS
FOR HIGH VOLTAGE SOLAR ARRAYS**

by

Renee Lynn Mong

Submitted to the Department of Aeronautics and Astronautics
on May 7, 1993 in partial fulfillment of the
requirements for the Degree of Master of Science in
Aeronautics and Astronautics

Future solar arrays are being designed for much higher voltages in order to meet high power demands at low currents. Unfortunately, negatively biased high voltage solar cells have been observed to arc when exposed to the low earth orbit plasma environment. Analytical and numerical models of this arcing phenomenon on conventional solar cells have been developed which show excellent agreement with experimental data. With an understanding of a mechanism for arcing, it is possible to determine methods of arc rate mitigation and to predict arc rates for experiments. Using the previously developed models, it was determined that the arcing rate can be decreased by (1) increasing the interconnector work function, (2) increasing the thickness of the coverglass and cover adhesive, (3) decreasing the secondary electron yield of the coverglass and adhesive, (4) decreasing the ratio of the coverglass/adhesive dielectric constants, and (5) overhanging the coverglass. Of these, methods (4) and (5) show the most promise in reducing or even eliminating arcing. In addition, arcing rates were predicted for the high voltage biased arrays of the Air Force's Photovoltaic and Space Power Plus Diagnostics experiment (PASP Plus) and NASA's Solar Array Module Plasma Interactions Experiment (SAMPIE). These predictions provide both expectations for the missions and a means to test the numerical and analytical models in the space environment for different solar cell technologies. Finally, a numerical model of the arc initiation process was also developed for wrap-through-contact cells, but experimental data is not available for comparisons.

Contents

Acknowledgements	3
1 Introduction	12
1.1 Background	13
1.2 Overview of This Research	19
2 Numerical and Analytical Models	21
2.1 Conventional Solar Cells	21
2.1.1 Numerical Model	21
2.1.2 Analytical Model	27
2.2 Wrap-Through-Contact Cells	33
3 Arc Mitigation Methods	42
3.1 Control Case	42
3.2 Interconnector Material	45
3.3 Dielectric Thickness	47
3.4 Secondary Electron Yield	48
3.5 Dielectric Constants	50
3.6 Overhanging the Coverglass	54
3.6.1 Numerical Results	54
3.6.2 Analysis	58
3.7 Arc Rate Results	61
4 PASP Plus and SAMPIE Predictions	66
4.1 PASP Plus	66
4.1.1 Experiment Description	67
4.1.2 Predictions	69
4.2 SAMPIE	79
4.2.1 Experiment Description	79

4.2.2	Predictions	83
5	Conclusions	85
5.1	Summary of Results	85
5.2	Recommendations for Future Work	87

List of Figures

1.1	Schematic of a conventional solar cell	13
1.2	Model of the conventional solar array used for numerical simulations . .	16
1.3	Arcing sequence of a high voltage solar array	18
2.1	Model system of the high voltage solar array and plasma interactions . .	22
2.2	Grid structure for conventional cell calculations	23
2.3	Typical electric potential contour plot for ambient ion charging of conventional cells	25
2.4	Typical surface charge density along side dielectrics after ambient ion charging of conventional cells	25
2.5	Electric field lines over a whisker on conductor surface	26
2.6	Geometry for EFEE charging	28
2.7	Typical electric field run-away versus time	29
2.8	Experimental data for ground and flight experiments	32
2.9	Schematic of a wrap-through-contact solar array	33
2.10	Wrap-through-contact solar array model used for numerical simulations .	34
2.11	Typical grid structure for calculations	35
2.12	Typical electric potential for ambient ion charging of WTC cells	36
2.13	Typical surface charge density along the side dielectric surface after ambient ion charging of WTC cells	37
2.14	Class 1 electric field at upper triple junction versus time	38
2.15	Class 2 electric field at upper triple junction versus time	39
2.16	Class 1 surface charge density over the coverglass (a) side surface, (b) front surface	40
2.17	Class 2 surface charge density over the coverglass side surface	41
3.1	Enhanced field electron emission charging time, τ_{eff} versus βV for the silicon conventional control case	44
3.2	Analytic arc rates for the silicon conventional control case	44

3.3	Enhanced field electron emission charging time, τ_{efee} , versus βV for different work functions, ϕ_w (eV)	46
3.4	Analytic predictions and numerical results for $\tau_{efee}/\tau_{efee}(\phi_w = 4.76\text{eV})$ versus βV	46
3.5	Enhanced field electron emission charging time, τ_{efee} , versus βV for different dielectric thicknesses, $d(\mu\text{m})$	47
3.6	Analytic predictions and numerical results for $\tau_{efee}/\tau_{efee}(d = 190\mu\text{m})$ versus βV	48
3.7	Enhanced field electron emission charging time, τ_{efee} , versus βV for different secondary electron yields, γ_{ee}	49
3.8	Surface charge density as a function of distance from the triple junction for different secondary electron yields, γ_{ee}	50
3.9	Enhanced field electron emission charging time, τ_{efee} , versus βV for different dielectric constant ratios	51
3.10	Dielectric side surface charge density before EFEE charging for different dielectric constants	52
3.11	Electron trajectories for $\epsilon_{d1}/\epsilon_{d2} = 2.7$	53
3.12	Electron trajectories for the control case of $\epsilon_{d1}/\epsilon_{d2} = 1.3$	53
3.13	Electron trajectories for $\epsilon_{d1}/\epsilon_{d2} = 0.74$	54
3.14	Average secondary electron yield over the adhesive versus time for different dielectric constants	55
3.15	Model of coverglass overhang	55
3.16	Enhanced field electron emission charging time, τ_{efee} , versus βV for different overhang lengths	56
3.17	Class comparison of τ_{efee} versus E_{TJ} for $\beta V = 3.5 \times 10^5 \text{V}$	57
3.18	Electron trajectories for $10\mu\text{m}$ overhang; $\beta V = 3 \times 10^5 \text{V}$	57
3.19	Electron trajectories for $50\mu\text{m}$ overhang; $\beta V = 3 \times 10^5 \text{V}$	58
3.20	Class 1 dielectric surface potential; $\beta V = 3 \times 10^5 \text{V}$, $d_o = 10\mu\text{m}$	59
3.21	Class 2 dielectric surface potential; $\beta V = 3.25 \times 10^5 \text{V}$, $d_o = 50\mu\text{m}$	59
3.22	Analytic arc rates for varying interconnector work functions, ϕ_w	62
3.23	Analytic arc rates for varying dielectric thicknesses, d	62
3.24	Predicted arc rates for varying secondary electron yields, γ_{ee}	63
3.25	Predicted arc rates for varying dielectric constant ratios, $\epsilon_{d1}/\epsilon_{d2}$	64
3.26	Predicted arc rates for varying coverglass overhang lengths, d_o (μm)	65
4.1	Deployed APEX spacecraft with PASP Plus experiment payload	68

4.2	Selected arc rate predictions with standard deviation errors for Si conventional array #1	73
4.3	Complete arc rate predictions in the differentiating voltage range for Si array #1	73
4.4	Selected arc rate predictions with standard deviation errors for Si conventional array #2	74
4.5	Complete arc rate predictions in the differentiating voltage range for Si array #2	74
4.6	Selected arc rate predictions with standard deviation errors for GaAs/Ge conventional array #4	75
4.7	Complete arc rate predictions in the differentiating voltage range for GaAs/Ge array #4	75
4.8	Selected arc rate predictions with standard deviation errors for GaAs/Ge conventional array #6	76
4.9	Complete arc rate predictions in the differentiating voltage range for GaAs/Ge array #6	76
4.10	Selected arc rate predictions with standard deviation errors for GaAs/Ge conventional array #11	77
4.11	Complete arc rate predictions in the differentiating voltage range for GaAs/Ge array #11	77
4.12	Selected arc rate predictions with standard deviation errors for APSA (#36)	78
4.13	Complete arc rate predictions in the differentiating voltage range for APSA (#36)	78
4.14	Arc rate prediction comparison for all PASP Plus conventional arrays at 350km	80
4.15	SAMPIE experiment package	81
4.16	SAMPIE experiment plate layout	82
4.17	SAMPIE arc rate predictions with standard deviation error bars for the silicon conventional array and APSA	84

List of Tables

3.1	Conventional silicon cell data used in numerical simulations	43
4.1	PASP Plus data used for arc rate predictions	70

List of Symbols

A	Fowler Nordheim coefficient ($1.54 \times 10^{-6} \times 10^{4.52\phi_w^{-1/2}} / \phi_w$ A/V ²)
B	Fowler Nordheim coefficient ($6.53 \times 10^9 \phi_w^{1.5}$ V/m)
C_{diele}	capacitance of dielectric (F/m ²)
C_{front}	capacitance of coverglass front surface (F)
d	thickness of dielectric (m)
d_1	thickness of coverglass (m)
d_2	thickness of adhesive (m)
d_{gap}	gap distance between cathode and anode (m)
d_i	distance of electron first impact point from triple junction (m)
d_o	overhang distance of coverglass (m)
d_o^c	critical overhang distance of coverglass (m)
E_e	electric field at emission site (V/m)
E_i	electron incident energy on dielectric plate (eV)
E_{max}	electron incident energy for maximum secondary electron yield (eV)
E_{TJ}	electric field at triple junction (V/m)
E_1	electric field of coverglass (V/m)
E_2	electric field of adhesive (V/m)
j_{ec}	electron current density from conductor (A/m ²)
j_{ee}	secondary electron current density from dielectric (A/m ²)
j_{FN}	Fowler-Nordheim current density from the conductor (A/m ²)
j_{id}	ion ram current density to the dielectric (A/m ²)
n_e	plasma number density (m ⁻³)
n_{es}	emission site number density (m ⁻²)
m_e	electron mass (kg)
m_i	ion mass (kg)
\dot{R}	arc rate (sec ⁻¹)
r_s	sheath radius (m)
S_{FN}	emission site area determined from F-N plot (m ²)

S_{real}	emission site area determined by accounting for electron space charge effects (m^2)
T_e	electron temperature (eV)
T_i	ion temperature (eV)
V_{arc}	voltage at which last arc occurred V
V_{bias}	bias voltage of interconnector/conductor V
V_e	voltage which minimizes arcing time V
V_i	initial voltage before solar cell charging V
v_{ion}	mean speed of ions entering sheath (m/sec)
v_x	electron velocity in the x direction (m/sec)
v_y	electron velocity in the y direction (m/sec)
y	distance of emission site from the triple junction (m)
β	field enhancement factor
ΔQ	charge lost from one coverglass by one discharge (C)
ϵ_{d1}	relative dielectric constant of coverglass
ϵ_{d2}	relative dielectric constant of adhesive
\mathcal{E}_l	energy at $\gamma_{ee} = 1$ (eV)
ϕ_c	potential of conductor (V)
ϕ_i	potential of coverglass-adhesive interface (V)
ϕ_w	work function (eV)
γ_{ee}	secondary electron yield
γ_{max}	maximum secondary electron yield at normal incidence
η	factor accounting for difference in electric field at emission site and triple junction
θ_i	incident impact angle of electron onto the dielectric surface
σ	surface charge density (C/m^2)
τ_{arc}	time between arcs (sec)
τ_{efee}	EFEE charging time (sec)
τ_{ion}	ion charging time (sec)
τ_{exp}	experiment time (sec)
ξ	factor accounting for difference of dielectric constants between coverglass and adhesive

Chapter 1

Introduction

In the past and present, solar arrays used in space have been operating at low voltage levels, typically biased at 28V. Future solar arrays, however, are being designed for much higher voltages in order to meet high power demands of the order of 10kW to 1MW. High current levels could be used instead to achieve these increased power demands, but the power distribution cables would need to be more massive and the resistive losses would be greater. Consequently, the current is maintained at a low value while the voltage is increased to attain the necessary power level.

A schematic of a conventional solar cell is shown in Fig. 1.1. The coverglass and substrate shield the solar cell from the environment, mainly to reduce radiation degradation. These are attached to the cell with adhesives. The solar cell itself is a semiconductor of two parts, a p-type semiconductor which has an abundance of electrons and an n-type semiconductor which has an abundance of electron holes. This construction allows the solar cell to use the photoelectric effect to convert solar energy into electric power. A photon with energy equal to or greater than the energy gap of the solar cell it enters will free an electron. This creates an electron-hole pair. If the pair is in the p-type semiconductor, the electron will be accelerated across the p-n barrier to the n-type semiconductor where it will recombine. The hole, however, will be repelled by the barrier because of the excess of holes in the n-type semiconductor. Likewise, if the electron-hole pair is in the n-type semiconductor, the hole will be accelerated across the p-n barrier and the electron repelled. Consequently, metal interconnectors connect the n-type semiconductor of one cell to the p-type semiconductor of the adjacent cell to utilize the current created by the electron and hole movement. Solar cells are connected in parallel with metal interconnectors to obtain desired current levels and connected in series to obtain desired voltage levels.

The solar array, along with other surfaces of the spacecraft which can allow the passage of current, collects current from the ambient plasma. In steady state, the spacecraft is

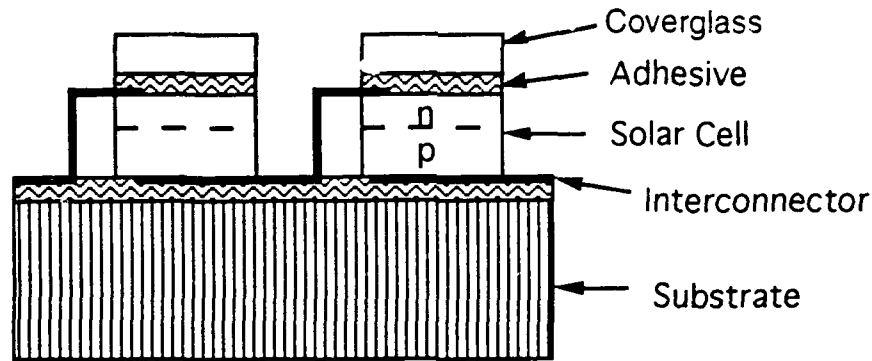


Figure 1.1: Schematic of a conventional solar cell

grounded with respect to the plasma by the zero net charging condition

$$\frac{\partial \rho}{\partial t} + \nabla \cdot \vec{j} = 0, \quad (1.1)$$

which is derived from Ampere's Law and Gauss's Law. To obey this condition, most of the solar array floats negatively with respect to the plasma. This is because the random thermal flux of the lighter electrons to the spacecraft is greater than the random flux of the heavier ions. Therefore, the spacecraft surfaces must be negatively biased in order to maintain zero net current collection.

High voltage solar arrays, however, have been observed to interact with the plasma environment of low earth orbit in two undesirable manners. For positive voltages, the current collection can be anomalously large, possibly leading to surface damage [25]. This phenomenon, known as "snap-over", occurs when the dielectric surface potential becomes positive, attracting electrons. Above a certain potential, more than one secondary electron is released by the incident electrons. These excessive secondary electrons are collected by the interconnector and seen as a current increase, which then incurs a power loss. For large negative voltage biases, arc discharges can occur [11]. Arcing observed in experiments has been defined as a sharp current pulse much larger than the ambient current collection which lasts up to a few microseconds. This current pulse is usually accompanied by a light flash at the edge of the solar cell coverglass. Arc discharges can cause electromagnetic interference and solar cell damage [26], so there is a need to study mitigation methods and to be able to predict arcing rates with models.

1.1 Background

Arcing has been studied in many experiments and theoretical arguments. The Plasma Interactions Experiments have been the only space experiments so far, though several

space experiments are planned for the near future. Arcing has also been observed in many ground tests conducted in vacuum plasma chambers. Two different theoretical explanations were given by Parks et al. [21] and Hastings et al. [10]. Cho and Hastings [3] used ideas from both to present a more complete theory of the arcing sequence of events.

Arcing on solar cells was originally observed by Heron et al. [11] in 1971 during a high voltage solar array test in a plasma chamber. The array was biased to -16kV, and arcing was observed as low as -6kV in a plasma density of 10^8m^{-3} .

In 1978, the first Plasma Interactive Experiment (PIX) [6] confirmed that arcing occurs in space. As an auxilliary payload on Landsat 3's Delta launch vehicle, PIX operated for 4 hours in a polar orbit around 920km. A solar array of twenty-four $2\text{cm} \times 2\text{cm}$ conventional silicon cells was externally biased to -1000V. Arcing discharges began at -750V.

In 1983, PIX II [7] was launched also as an auxilliary payload aboard a Delta launch vehicle into a near circular polar orbit of approximately 900km in altitude. The five hundred $2\text{cm} \times 2\text{cm}$ silicon conventional cells, biased to -1000V, experienced arcing as low as -255V and at densities as low as 10^3cm^{-3} . The results also found arcing to be the most detrimental effect of negative biasing.

Ferguson [4] studied the PIX II ground and flight results. The interconnectors collected current proportional to the applied voltage bias. The arc rate \dot{R} was determined to scale as

$$\dot{R} \approx n_e \left(\frac{T_i^{1/2}}{m_i^{1/2}} \right) V_{bias}^a, \quad (1.2)$$

where $a \simeq 5$ for the ground experiments and $a \simeq 3$ for the flight experiments, n_e is the ambient plasma number density, T_i is the ambient ion temperature, and m_i is the ambient plasma ion mass. The dependence of the arc rate on these parameters indicates that the coverglass surface is recharged by the thermal flux of ions.

Ground experiments revealed more characteristics of the arcing phenomenon. Experiments by Fujii et al. [5] showed that dielectric material near the biased conductor in the plasma environment is essential for arcing to occur. Fujii et al. tested material plates biased to high negative voltages in a plasma environment. The plate partially covered by a $200\mu\text{m}$ thick coverglass experienced arcing at -450V while the uncovered plate did not arc, except at -1000V when the arc occurred at the substrate. Snyder [22] measured the electric potential on the coverglass and found that it decreased significantly when an arc occurred. This indicates that the negative charge created during arcing discharged the positive surface charge accumulated on the coverglass surface. Both Snyder and Tyree

[23] and Inouye and Chaky [15] observed electron emission from the solar array that could not be explained by the ambient plasma. Finally, electromagnetic waves generated from the arcing current were measured by Leung [19].

The first theoretical model was proposed by Jongeward et al. [16] and later expanded by Parks et al. [21]. Jongeward et al. attributed Snyder's [22] experimental observation of the decrease in coverglass potential prior to arcing to enhanced electron emission from the interconnector, which corresponds to the electron emission observed in Refs. [23] and [15]. They suggested the emission is due to a thin layer of ions deposited on the interconnector, causing the electric field to be significantly increased. The time for positive charge build up is then dependent on the ambient density n_e , the interconnector size, and the bias voltage. The arc discharge is proposed to occur by a positive feedback mechanism from electron heating which leads to a space charge limited discharge. At low ion densities, other surface neutralizing effects are said to dominate, thus inhibiting the positive charge build up. Jongeward et al. also modeled the arc discharge decay time by assuming space charge limited conditions and showed that the peak current magnitude agrees well with this assumption.

Parks et al. [21] concentrated on further detailing the theory proposed by Jongeward et al. [16] on the prebreakdown electron emission current. They accepted Jongeward's theory of positive charge build-up in a thin insulating layer on the interconnector and of arcing originated from interconnector electron emission instead of from the ambient plasma. Parks et al. proposed the addition of the phenomena presented by Latham [17, 18], namely that nonmetallic emission processes are significantly responsible for electron emission by nominally metallic surfaces. Therefore, Parks et al. claimed that the arc rate must be proportional to the electron emission current density and the bias voltage. They further suggested that electron emission is controlled by the vacuum electric field at the surface of the insulator. Given these assumptions, they determined that the rate of field build-up in the insulator is

$$\epsilon_o \frac{d}{dt} (\epsilon_{ins} E_{ins} - E_{ins-vac}) = j_i + j_{FN} (e^{adP} - 1), \quad (1.3)$$

where ϵ_{ins} is the dielectric constant of the insulator layer, E_{ins} is the electric field inside the insulator, $E_{ins-vac}$ is the electric field at the insulator-vacuum interface, j_i is the ion current density, j_{FN} is the Fowler-Nordheim emission current at the metal-insulator interface, a is the rate of ionization per unit distance inside the layer, d is the thickness of the insulator layer, and P is the probability that electrons are emitted from the insulator-

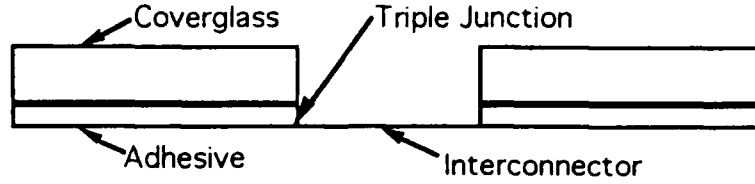


Figure 1.2: Model of the conventional solar array used for numerical simulations

vacuum interface. The emission current from the metal-insulator interface is given by

$$j_{FN} = A E_{ins}^2 e^{-\frac{B}{E_{ins}}}, \quad (1.4)$$

where A and B are the Fowler-Nordheim emission coefficients, given in Eqns. 1.8 and 1.9. This expression for the electric field accounted for experimental observations of the characteristics of the voltage threshold, the prebreakdown electron emission current, and the arcing rate.

Hastings et al. [10] did not try to explain the prebreakdown electron emission current but instead proposed a model for the gas breakdown seen as the arc discharge. They suggested that neutral gas is desorbed from the sides of the coverglass by electron bombardment, a phenomena known as electron stimulated desorption (ESD). The bombarding electrons are emitted from the interconnector, as determined from Snyder's experiments [22], and from the coverglass as secondary electrons which return to the side surface. The desorbed neutrals then accumulate in the gap between the coverglasses over the interconnector, forming a potentially high-pressure gas layer which can break down from the electron emission current flowing through it. This was in contrast to the previous theory which suggested that the arc occurs in an insulator on the surface of the interconnector.

Recent work by Cho and Hastings [3] combined some of the ideas from these two theories and studied the charging of the region near the plasma, dielectric, and conductor triple junction. The model that they studied is shown in Fig. 1.2. The dielectric consists of both the coverglass and the adhesive bonding the coverglass to the solar cell. The conductor is the interconnector, which is usually placed between the cell and substrate on one end and between the cell and cover adhesive in the adjoining cell. The solar cell itself was neglected since the potential drop across it is at most a few volts while the potential drop across the coverglass and adhesive is hundreds or even thousands of volts for high voltage operation.

Cho and Hastings developed a numerical simulation of the arc initiation processes. They studied charging of the dielectric surfaces by three sources: ambient ions, ion-induced secondary electrons, and enhanced field electron emission. From numerical

results, they determined the following arc sequence, illustrated in Fig. 1.3:

- (1) ambient ions charge the dielectric front surface, but leave the side surface effectively uncharged;
- (2) ambient ions induce secondary electrons from the conductor which charge the side surface to a steady state unless enhanced field electron emission (EFEE) becomes significant;
- (3) EFEE will charge the side surface if there is an electron emission site close to the triple junction with a high field enhancement factor, β ; and
- (4) EFEE can result in collisional ionization of neutrals desorbed from the coverglass, which is what is observed as the arc discharge.

They also found that the electric field at the triple junction is not bounded during EFEE charging.

Cho and Hastings used the numerical results to develop analytical formulas describing the arcing rate [3, 9]. They suggested that the time between arcs is the minimum of the sum of the ambient charging time τ_{ion} and the enhanced field electron emission charging time τ_{efee} , so that the arc rate \dot{R} is given by:

$$\dot{R} = \min(\tau_{ion} + \tau_{efee})^{-1} \quad (1.5)$$

For the ion charging, Cho and Hastings showed that ambient ions mainly charge the front surfaces of the coverglass, not the side surfaces. They expressed this time as

$$\tau_{ion} = \frac{\Delta Q}{en_e v_{ion} A_{cell}}, \quad (1.6)$$

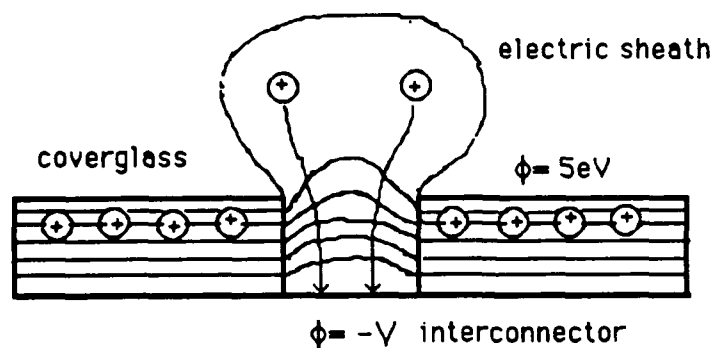
where ΔQ is the charge lost by the coverglass due to an arc discharge, which must be recovered; $en_e v_{ion}$ is the ambient ion flux to the front surfaces, with v_{ion} as the mean speed of ions entering the sheath surrounding the solar array; and A_{cell} is the frontal area of the coverglass. Assuming a constant secondary electron yield and constant voltage bias, they derived the following analytical expression for the EFEE charging time, τ_{efee} :

$$\tau_{efee} = \frac{C_{diele} d_i^2}{(\gamma_{ee} - 1) \sqrt{S_{real}} \eta \xi A \frac{S_{EN}}{S_{real}} B \beta} \exp\left(\frac{Bd}{\beta V \eta \xi_0}\right), \quad (1.7)$$

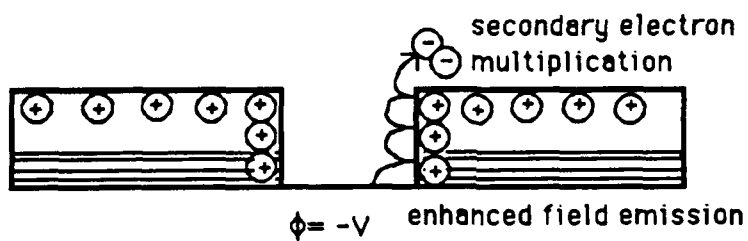
where A and B are the Fowler-Nordheim coefficients given by

$$A = \frac{1.54 \times 10^{-6} 10^{4.52/\sqrt{\phi_w}}}{\phi_w}, \quad (1.8)$$

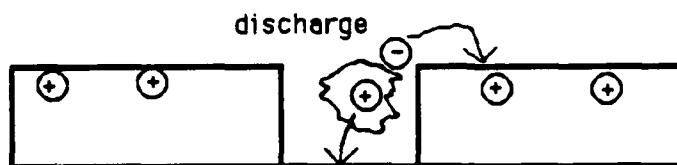
$$B = 6.53 \times 10^9 \phi_w^{1.5}, \quad (1.9)$$



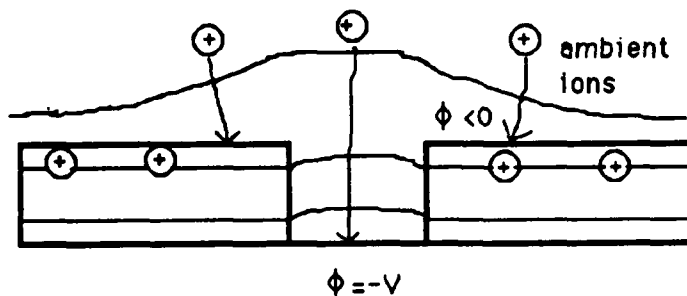
charging
of front
surface



charging
of side
surface



discharge



recharging
by ions

Figure 1.3: Arcing sequence of a high voltage solar array

ξ is a factor to account for the difference in dielectric constants and is given by

$$\xi = \left[\frac{d_2}{d_i} + \frac{\epsilon_{d_2} (d_i - d_2)}{\epsilon_{d_1} d_i} \right]^{-1}, \quad (1.10)$$

ξ_0 is ξ evaluated with $d_i = d$, d_i is the distance from the triple junction of the first impact by an electron emitted from the conductor, C_{diele} is the capacitance of the dielectric at this impact site, γ_{ee} is the secondary electron yield of the dielectric, S_{real} is the real area of the emission site, S_{FN} is the Fowler-Nordheim "effective" area of the emission site, η is a factor to account for the difference in the electric field at the emission site from the triple junction, d_1 is the thickness of the coverglass, d_2 is the thickness of the adhesive, $d = d_1 + d_2$, V is the voltage at which the arc occurs, and β is the field enhancement factor. From comparison with experiments, Hastings et al. [9] suggested that β must be greater than a few hundred, so they assumed that the field enhancement is due to a thin dielectric layer on the conductor surface rather than microprotrusions. They later updated their views as explained in Section 2.1.1.

From experimental observations, Hastings et al. [9] suggested other characteristics of the arcing processes, such as the discharge wave hypothesis and the occurrence of one arc at a time within a certain area. The discharge wave hypothesis suggested that at arc initiation emitted electrons form a plasma cloud over the solar array. Some of the electrons, attracted by the positive surface potential, strike the coverglasses in the local area until they are discharged. Experimental results also showed that the arc current is more likely to be carried by electrons, consistent with the hypothesis that arcing is initiated by electron emission from the interconnector. In addition, as the temperature increased fewer neutral gas molecules were desorbed from the dielectrics and the arc rate was seen to decrease, consistent with the hypothesis that ionization of the neutral gases also plays a role in arc initiation.

1.2 Overview of This Research

Power requirements for space systems are increasing significantly. As the most reliable power source, high voltage solar arrays will be needed to meet these requirements. Since arcing degrades the array performance and causes electromagnetic interference which affects nearby instruments, it is imperative to study arcing. Recent studies by Cho and Hastings [3, 9] determined an arcing sequence of events and an arcing rate based on numerical and theoretical work which has been shown to agree well with experimental results. With these models it is possible to determine methods of arc rate mitigation and

to predict arc rates for experiments. This research can then be used in the design of new solar cells and in the design of high voltage solar arrays.

The focus of this research is twofold: to identify and study mitigating effects on arc rates and to present arc rate predictions for two space experiments soon to be launched. In Chapter 2 the numerical and analytical models developed by Cho and Hastings are reviewed, and the numerical model modified for the wrap-through-contact solar cell geometry is presented. Based on the analytical model for conventional solar cells, arc rate reduction methods are studied using the corresponding numerical model in Chapter 3. In Chapter 4, arcing rates are predicted for the high voltage biased arrays of the Air Force's Photovoltaic and Space Power Plus Diagnostics experiment (PASP Plus) and NASA's Solar Array Module Plasma Interactions Experiment (SAMPIE). Finally, conclusions are summarized and future work is suggested in Chapter 5.

Chapter 2

Numerical and Analytical Models

2.1 Conventional Solar Cells

A schematic of a conventional solar cell is shown in Fig. 1.1. In high voltage operation, the voltage differential over the coverglass and adhesive can be hundreds or even thousands of volts while the voltage differential over the cell itself is at most a few volts. For modeling purposes, the cell semiconductor can therefore be neglected, as shown in Fig. 1.2. In this model, the interconnector is a conductor and the coverglass and adhesive are dielectrics. The numerical and analytical models used for conventional cells were developed by Cho and Hastings [3, 9], as briefly described in Section 1.2.

2.1.1 Numerical Model

The numerical model incorporates all relevant physical characteristics and processes for solar cell charging from the ambient plasma, electron emission from the interconnector, and secondary electron emission from the dielectrics. A representation of this system is shown in Fig. 2.1. The coverglass and adhesive surface charge densities are affected by the ion ram current density j_{id} , the electron emission current density from the conductor j_{ec} , and the secondary electron current density from the surface j_{ee} . After arc initiation, the current densities from the ionization of neutral gases may also be significant. These are not considered, however, as only the time to arc initiation is the focus of this research. The rate of change of the dielectric surface charge density can then be expressed as

$$\frac{d\sigma}{dt}(x, t) = j_{id}(x, t) - \int P(x, y, t)j_{ec}(y, t)dy - \int P(x, x', t)j_{ee}(x')dx' + j_{ee}(x, t), \quad (2.1)$$

where $P(x, y, t)$ is the probability that an electron emitted from position y on the conductor hit the dielectric at position x at time t , and $P(x, x', t)$ is the probability that an electron emitted at x' hits the dielectric at x .

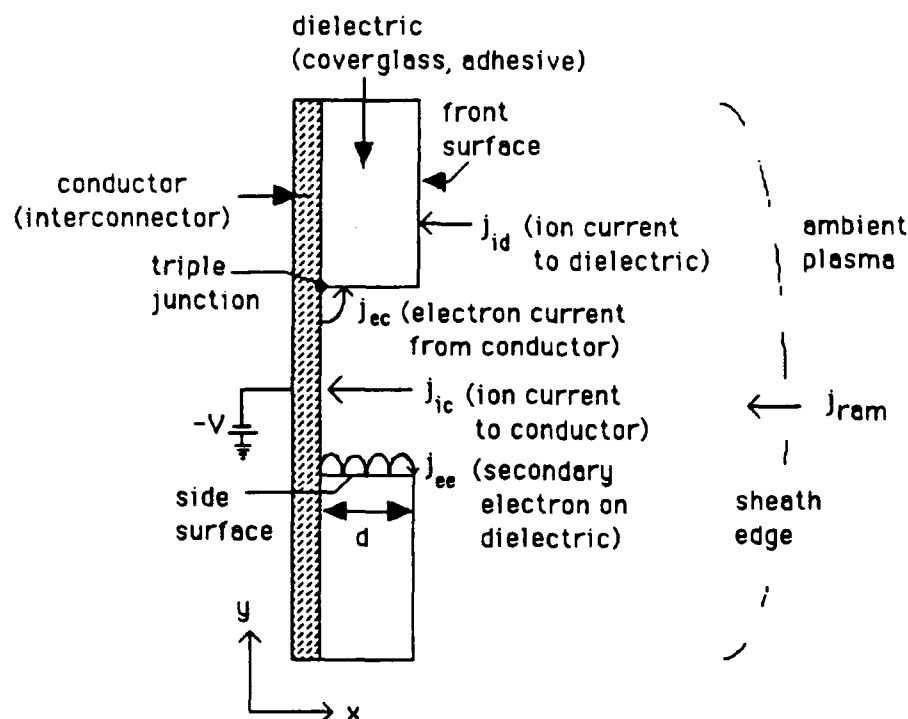


Figure 2.1: Model system of the high voltage solar array and plasma interactions

The numerical model consists of three schemes. The first scheme uses the capacitance matrix method to obtain a preliminary electric potential distribution along the dielectric surfaces. The second scheme involves a particle-in-cell (PIC) method which is used for ambient ion charging. Once a steady state is obtained from the ion charging, a space-charge-free orbit integration scheme calculates the electron charging by enhanced field electron emission (EFEE).

All schemes use the same computational domain and grid. The phase space of the domain consists of two position coordinates and three velocity coordinates. As shown in Fig. 2.2, the domain includes two halves of solar cells with the interconnector forming the lower boundary of the gap between the cells. The boundary condition far from the cells at $x = 0$ is $\phi = 0$, simulating the far field. In these simulations, any electrons leaving the domain at $x = 0$ will also leave the sheath. The boundaries are thus Dirichlet in the x direction and periodic in the y direction to simulate a solar array. The grid is clustered along the dielectric sides and near the interconnector for better resolution of the large electric potential gradients in these areas.

The capacitance matrix method is used to obtain an initial condition for the PIC code, thus reducing the simulation time. In employing this method, which is given in

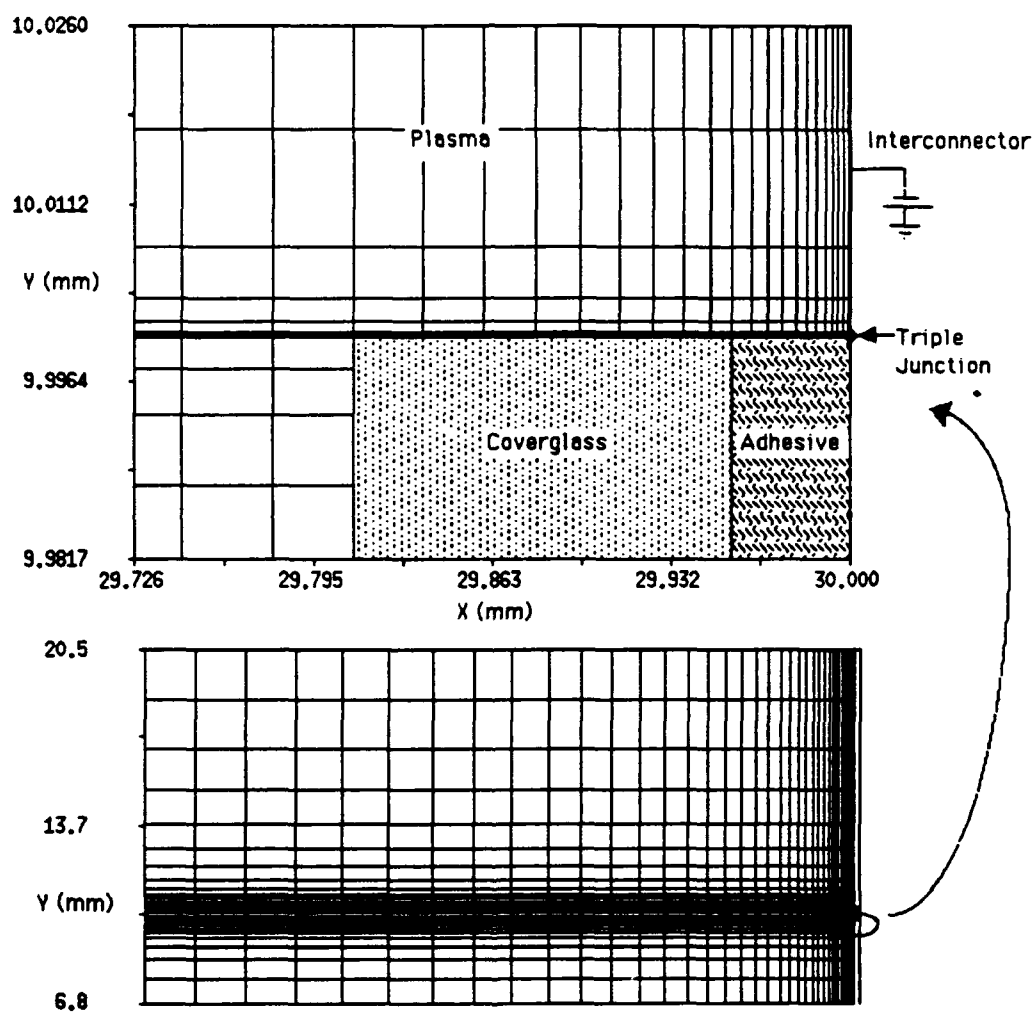


Figure 2.2: Grid structure for conventional cell calculations

Ref. [14], a unit charge is ascribed to one cell on the dielectric surface while all other cells have zero charge. The Poisson equation is then solved to determine the electric potential in every cell on the dielectric surface due to this unit charge. This process is repeated for each grid cell along the surface of the dielectrics. Afterwards, the array containing all of the potential values calculated is inverted to determine the capacitance value for each grid cell. This matrix is stored for use as the initial conditions of the PIC code, so that the simulation can be started from any charging state described by only the surface charge or the surface potential.

With the capacitance matrix calculated for unit charges, the PIC code calculates the space potential based on a pre-determined surface potential. The initial conditions for the dielectric potential are $\phi = 0$ on the front surface and a linear distribution of ϕ on the side surface with the conductor voltage at one end and the front surface zero voltage at the other end. The ram velocity is oriented 90° to the dielectric front surfaces and conductor. To save computational time, an artificial ion mass is used such that $m_i/m_e = 100$. Ions and electrons are initially inserted uniformly throughout the domain according to the ambient density. After the space potential is calculated using the Poisson equation, the ions and electrons are moved according to the new potential. A new space charge density for each grid point can then be calculated based on the new ion and electron positions. This loop is then repeated with the potential being re-calculated based on the new charge density. The PIC code is run for a time equivalent to the inverse of the ion plasma frequency to adjust the space charge completely with the surface potential.

The results from the PIC scheme are the initial conditions for the dielectric charging scheme. A typical contour plot of the initial electric potential is shown in Fig. 2.3, and the corresponding surface charge density is shown in Fig. 2.4.

No electron emissions from the conductor or dielectric are taken into account in the PIC code since they are negligible. The electron emission which leads to arc initiation was determined to be enhanced field electron emission (EFEE) by Cho and Hastings [3]. They described this current density from a finite emission site on the conductor surface as

$$j_{ec}(y) = A \frac{S_{FN}}{S_{real}} \beta^2 E^2 \exp\left(-\frac{B}{\beta E}\right), \quad (2.2)$$

which is the Fowler-Nordheim expression for field emission due to a thin dielectric layer with the added factor S_{FN}/S_{real} to account for the negative space charge effect near the emission site. The electric field E in this expression is the electric field at the dielectric-vacuum interface. A and B are the Fowler-Nordheim emission coefficients given by Eqns. 1.8 and 1.9. The field enhancement factor β is assigned to the emission site

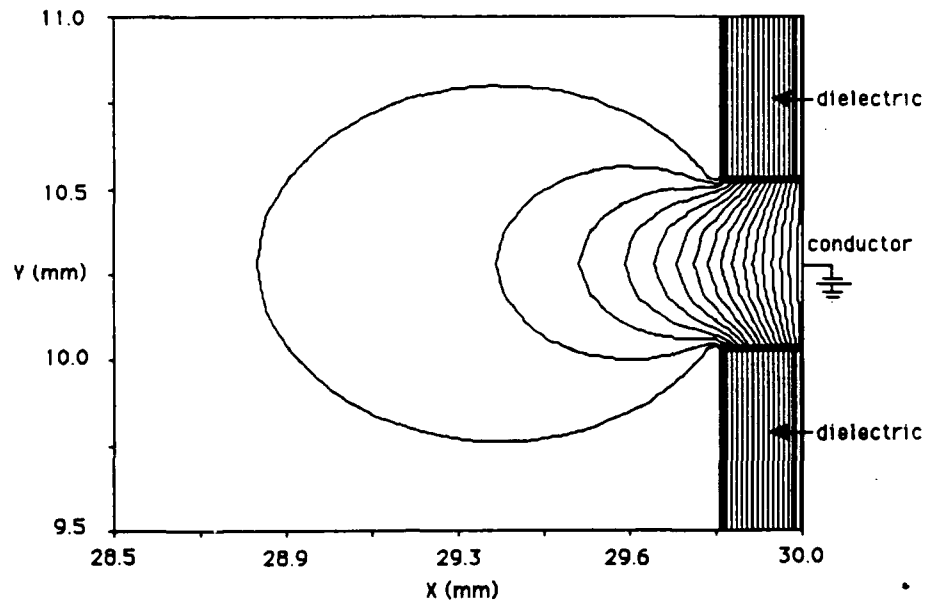


Figure 2.3: Typical electric potential contour plot for ambient ion charging of conventional cells

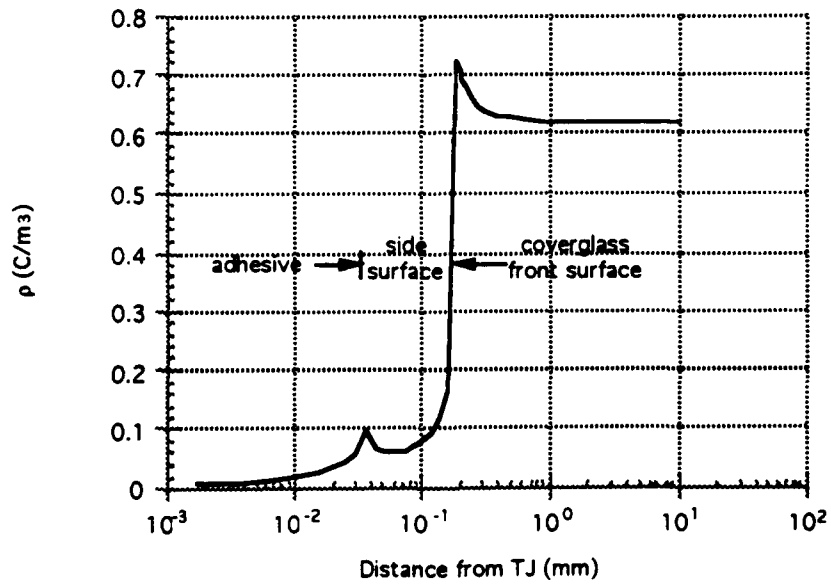


Figure 2.4: Typical surface charge density along side dielectrics after ambient ion charging of conventional cells

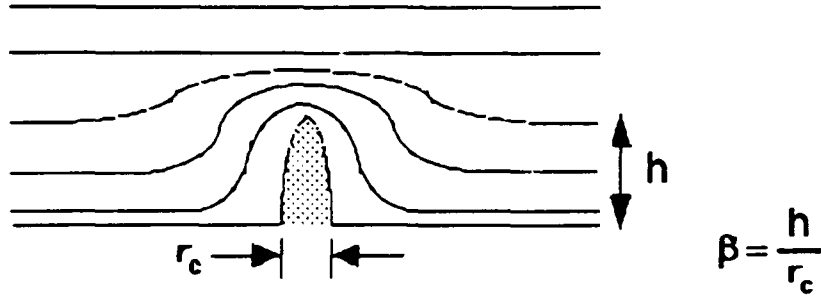


Figure 2.5: Electric field lines over a whisker on conductor surface

to represent an enhancement due to manufacturing defects or impurities. As shown in Fig. 2.5, the protrusion causes a higher electric field gradient which enhances the electric field at its tip. From electrostatic theory for a whisker, β is the factor of the enhanced electric field at the tip of the whisker defect relative to the average electric field in the vicinity is equivalent to the ratio of the height of the protrusion to its radius of curvature. This factor can be of the order of 1 to 10^3 , with typical values of interest in the hundreds. The secondary electron current density at each point x is given by

$$j_{ee}(x, t) = \int \gamma_{ee}(x, y) P(x, y, t) j_{ec}(y, t) dy + \int \gamma_{ee}(x, x') P(x, x', t) j_{ee}(x') dx'. \quad (2.3)$$

In the orbit integration scheme, the first term in Eqn. 2.1 is neglected since it was shown to be insignificant during electron charging [3]. Using Eqn. 2.3, the surface charge density equation can be rewritten as

$$\frac{d\sigma(x, t)}{dt} = \int (\gamma_{ee}(x, y) - 1) P(x, y, t) j_{ec}(y, t) dy + \int (\gamma_{ee}(x, x') - 1) P(x, x', t) j_{ee}(x') dx'. \quad (2.4)$$

The orbit integration scheme then consists of

- (1) obtaining the surface potential by using the capacitance matrix method;
- (2) solving Laplace's equation to obtain the space potential;
- (3) integrating test electron orbits from the conductor to calculate γ_{ee} and the impact probabilities P for a given electron current density from the conductor;
- (4) solving Eqns. 2.1 and 2.3 for the secondary electron current density j_{ee} and the rate of change of the surface charge density;
- (5) renewing the surface charge density;
- (6) obtaining the new potential for the renewed surface charge density;
- (7) calculating the timestep;
- (8) determining if the space charge current density is too high or the timestep is too small, either of which will halt the program; and

(9) calculating electron trajectories.

Steps (4) through (9) are repeated until the specified number of timesteps are completed or the program is stopped in step (8). If the space charge current density is too high, the space charge effects of the emission current can no longer be neglected so the PIC code must be run if further calculations are needed. If the timestep is too small, the electric field is most likely running away.

The timestep for EFEE charging is calculated based on the rate of change of the dielectric surface charge density at the first impact point $x = d_1$. This can be expressed by neglecting the second term in Eqn. 2.1, reducing the equation to

$$\int_0^{d_1} \frac{d\sigma}{dt} dx = \int \left(\int_0^{d_1} P(x, y, t) dx \right) (\gamma_{ee} - 1) j_{ec}(y, t) dy. \quad (2.5)$$

The integral $\int_0^{d_1} P(x, y, t) dx$ is approximately unity since the point $x = d_1$ is the first impact point by emitted electrons. The equation then simplifies to

$$\frac{d\sigma}{dt} d_1 = (\gamma_{ee} - 1) j_{ec}(y, t) \sqrt{S}, \quad (2.6)$$

or

$$\Delta t = \frac{\Delta \sigma}{(\gamma_{ee} - 1) j_{ec}(y, t) (\sqrt{S}/d_1)}, \quad (2.7)$$

where S is the area of the emission site, as shown in Fig. 2.6. The potential difference between the triple junction ($x = 0$) and the impact point ($x = d_1$) can be expressed as

$$\phi_d = \frac{\sigma}{C_{diele}}, \quad (2.8)$$

where C_{diele} is the capacitance of the dielectric surface and σ is the surface charge density. The electric field, then, is approximately

$$E = \frac{\sigma}{C_{diele} d_1}. \quad (2.9)$$

The timestep can therefore be determined by solving

$$\Delta t = 0.02 \frac{\Delta E C_{diele} d_1}{(\gamma_{ee} - 1) j_{ec}(y, t) (\sqrt{S}/d_1)}, \quad (2.10)$$

where the empirical factor 0.02 is used so that the timesteps will be shorter than the actual timescale of arc initiation.

2.1.2 Analytical Model

The analytical model, which is used to calculate the arc rates, is drawn from the theory of Cho and Hastings [3, 9], discussed in Section 1.2. The arc rate is determined by

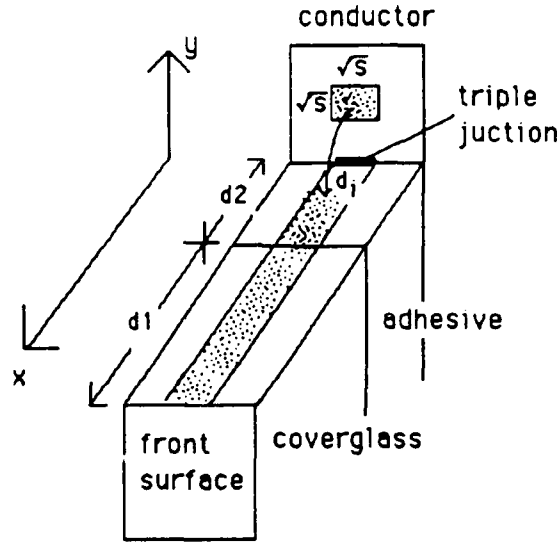


Figure 2.6: Geometry for EFEE charging

calculating the time between arcs, τ_{arc} , given by

$$\tau_{arc} = \min(\tau_{ion} + \tau_{efee}), \quad (2.11)$$

where τ_{ion} is the ambient ion charging time given by Eqn. 1.6 and τ_{efee} is the enhanced field electron emission charging time given by Eqn. 1.7. The analytical expression for τ_{efee} is determined by starting with Eqn. 2.6. A schematic of the geometry considered is shown in Fig. 2.6.

The electric field at the triple junction can be expressed as

$$E_{TJ} = \xi \frac{\phi_d}{d_i} = \xi \frac{\sigma}{C_{diele} d_i}, \quad (2.12)$$

where ξ is given by Eqn. 1.10 if the first impact site of the electrons emitted from the interconnector is on the coverglass side surface. If it is on the adhesive side surface, ξ is unity. The electric field at the emission site, E_e , can be very different from the electric field at the triple junction. To account for this, the factor η is introduced so that

$$E_e = \eta E_{TJ} = \eta \xi \frac{\sigma}{C_{diele} d_i}. \quad (2.13)$$

Substituting Eqns. 2.2 and 2.13 into Eqn. 2.6 results in

$$\frac{dE_e}{dt} = \eta \xi \frac{(\gamma_{ee} - 1) \sqrt{S_{real}}}{C_{diele} d_i^2} A' B^2 \exp\left(-\frac{B}{3E_e}\right). \quad (2.14)$$

This can be integrated, assuming the secondary electron yield is constant, to obtain

$$E_e(t) = \frac{E_{e_0}}{1 + \frac{3E_{e_0}}{B} \ln\left(1 - \exp\left(-\frac{B}{3E_{e_0}}\right) \left(\frac{B}{3}\right) Ct\right)}, \quad (2.15)$$

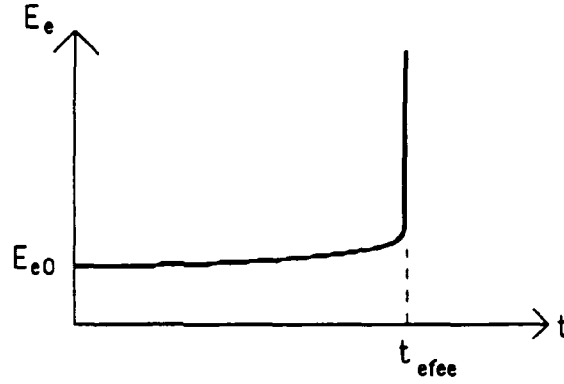


Figure 2.7: Typical electric field run-away versus time

where C is the constant given by

$$C = \eta \xi \frac{(\gamma_{ee} - 1) \sqrt{S_{real}}}{C_{diele} d_i^2} A' \beta^2 \quad (2.16)$$

and E_{e0} is the initial electric field at the electron emission site on the interconnector. From the numerical simulations it is known that the electric field E_e usually exhibits the behavior shown in Fig. 2.7. The field run-away to infinity corresponds to the denominator of Eqn. 2.15 reaching zero. This run-away time also corresponds to the time τ_{efee} , so τ_{efee} can now be determined:

$$\tau_{efee} = \frac{1 - \exp\left(-\frac{B}{\beta E_{e0}}\right)}{\exp\left(-\frac{B}{\beta E_{e0}}\right)} \left(\frac{B}{\beta}\right) C \quad (2.17)$$

$$\simeq \frac{\beta}{B} \exp\left(\frac{B}{\beta E_{e0}}\right) \frac{1}{C} \quad (2.18)$$

$$= \frac{C_{diele} d_i^2}{(\gamma_{ee} - 1) \sqrt{S_{real}} \eta \xi A' \frac{S_{EN}}{S_{real}} B \beta} \exp\left(\frac{B}{\beta E_{e0}}\right). \quad (2.19)$$

Eqn. 2.19 is the same as Eqn. 1.7 with E_{e0} expressed as the potential difference between the coverglass front surface and the triple junction:

$$E_{e0} = \eta \frac{V}{d} \xi_0. \quad (2.20)$$

Finding the minimum of the sum of the ion and EFEE charging times accounts for the fact that EFEE charging can initiate whenever the surface has a strong enough electric field, not just when the front surface current returns to zero. To find this minimum charging time, electron emission sites must be considered along the entire conductor as opposed to the numerical model which sets one emission site usually next to the triple junction. For each emission site a voltage V_e can be calculated at which the arc occurred by solving the differential equation

$$\frac{d\tau_{arc}}{dV_e} = 0, \quad (2.21)$$

or

$$\frac{d}{dV_e} \left[\frac{(V_e - (V_{arc} - \frac{\Delta Q}{C_{front}}))C_{front}}{en_e v_{ion} A_{cell}} + \frac{C_{diele} d_i^2}{(\gamma_{ee} - 1) \sqrt{S_{real}} \eta \xi A \frac{S_{EN}}{S_{real}} B \beta} \exp\left(\frac{Bd}{\beta V_e \eta \xi_0}\right) \right] = 0. \quad (2.22)$$

where V_{arc} is the voltage of the last arc discharge and C_{front} is the capacitance of the coverglass front surface.

In order to solve Eqn. 2.22, a number of properties must be known or determined. First, the following cell properties must be known: the thickness of the coverglass and cover adhesive (d_1, d_2), the dielectric constants of the coverglass and adhesive ($\epsilon_{d_1}, \epsilon_{d_2}$), the energy of incident electrons for maximum secondary electron yield for the coverglass and adhesive (E_{max_1}, E_{max_2}), the maximum secondary electron yield at normal incidence for the adhesive and coverglass ($\gamma_{max_1}, \gamma_{max_2}$), the interconnector work function (ϕ_w), and the solar cell frontal area (A_{cell}). Then, the following factors can be determined: A according to Eqn. 1.8; B from Eqn. 1.9; ξ and ξ_0 from Eqn. 1.10; $d = d_1 + d_2$; C_{front} which is approximated as

$$C_{front} = \frac{1}{(A_{cell} \epsilon_{d_1})/d_1 + (A_{cell} \epsilon_{d_2})/d_2}; \quad (2.23)$$

and γ_{ee} which is given by [8]

$$\gamma_{ee} = \gamma_{max} \frac{E_i}{E_{max}} \exp\left(2 - 2\sqrt{\frac{E_i}{E_{max}}}\right) \exp[2(1 - \cos \theta_i)]. \quad (2.24)$$

Here E_i is the incident energy of the emitted electrons impacting the dielectrics given by

$$E_i = e\phi_d = \frac{E_{TJ} d_i}{\xi} = \frac{\xi_0}{\xi} V \frac{d_i}{d} \quad (2.25)$$

and θ_i is the incident angle of those electrons at the first impact site given by

$$\theta_i = \arctan\left(\frac{d_i}{y}\right), \quad (2.26)$$

where y is the distance of the emission site from the triple junction. The mission parameters determine the ion velocity v_{ion} and the range of the ambient density n_e . If the array is orientated at 90° to the ram velocity, v_{ion} is the orbital velocity. Otherwise, v_{ion} is a sum of the orbital velocity and the mean thermal speed of ions $\bar{c}_i/4$, where

$$\bar{c}_i = \sqrt{\frac{8T_i}{\pi m_i}}. \quad (2.27)$$

Consequently, the ion mass and electron temperature must also be known. For each arc calculation, n_e is chosen randomly from a uniform distribution in $\log_{10} n_e$. Other

properties only known within a range include areas S_{eff} and S_{real} and enhancement factor β . Areas S_{eff} and S_{real} are randomly chosen from uniform distributions in $\log_{10} S_{eff}$ and $\log_{10} S_{real}$, respectively, between given minimum and maximum values. The enhancement factor β is randomly selected from the distribution $f(\beta) = f_o \exp(-\beta/\beta_o)$, where f_o is determined from the normalization: $\int f(\beta) d\beta = 1$. Finally, the three parameters left to be determined are C_{diele} , d_i , and η , all of which are functions only of the emission site distance y from the triple junction. To determine C_{diele} , the capacitance matrix scheme used with unit surface charge values must be run. The relevant values are the diagonal elements. Those that correspond to the lower side dielectric are non-dimensionalized by the normal capacitance

$$C_{norm} = \frac{1}{\frac{d_1}{\epsilon_{d_1}} + \frac{d_2}{\epsilon_{d_2}}} \quad (2.28)$$

and inverted. The corresponding distances from the triple junction are non-dimensionalized by the thickness of the two dielectrics, d . These values are plotted and fit to a five order polynomial:

$$C_{diele}^{-1} = \sum_{n=0}^{n=5} c_n \left(\frac{d_i}{d} \right)^{n-1} \quad (2.29)$$

To determine d_i and η , results from the orbit integration scheme of the numerical model are used to obtain functional forms. These are

$$\frac{d_i}{d} = \sum_{n=1}^{n=4} b_n \left(\frac{y}{d} \right)^{\frac{1}{2n}} \quad (2.30)$$

and

$$\eta = \frac{E_e}{E_{TJ}} \sum_{n=1}^{n=4} a_n ((\bar{y} - 1)^{2n} - 1), \quad (2.31)$$

where $\bar{y} = y/(d_{gap}/2)$.

The voltage V_e is determined to be in the range of V_i , the voltage differential between the front surface and conductor just after the arc, and V_{bias} . If τ_{efee} dominates to the point where τ_{ion} is insignificant, $V_e = V_i$. Likewise, if τ_{ion} dominates, $V_e = V_{bias}$. Otherwise, the arcing time is affected by both τ_{efee} and τ_{ion} , so V_e is determined by the Newton-Raphson method. After τ_{arc} is calculated for every emission site, typically numbering 1000, the smallest τ_{arc} is compared with the experiment time, τ_{exp} . If τ_{exp} is greater than τ_{arc} , another τ_{arc} is calculated until the sum of the arcing times is greater than τ_{exp} . The arc rate is then the number of arcs counted less one divided by the experiment time.

For a given solar array, the surface is divided into sections of area equivalent to the area covered by the arc discharge wave. Based on experimental measurements in Ref. [9], this area is chosen to be 0.012m². All arcs in a section are assumed to be

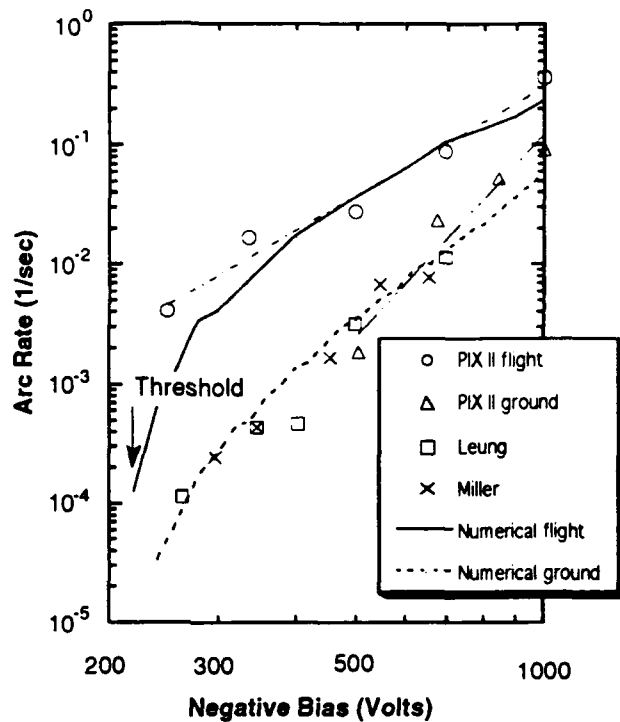


Figure 2.8: Experimental data for ground and flight experiments

correlated, but arcs are assumed to be uncorrelated between different sections. The arc rate is calculated for each correlated area independent of the other areas. If there is more than one correlated area, the actual arc rate for the array is the sum of the arc rates of each area.

Cho and Hastings use this procedure in Ref. [3] to calculate the arc rate numerically for the PIX II flight and ground experiments. As can be seen in Fig. 2.8, the results show excellent agreement with the data over the range that the data exists. They predict a threshold when the charging process is exponentially slow and also predict a saturation for high voltages. The lower parts of the curves cover the regime where the enhanced field electron emission charging is the slowest charging process in the system. The arc rate dependence on voltage here is exponential and enables a threshold voltage to be defined with a small uncertainty. This threshold voltage can be defined as the voltage at which the arc rate is decaying very rapidly. The upper parts of the arc rate curves cover the regime dominated by the ion recharging time. This leads to a decrease in the rate of change of arc frequency as can be clearly seen in the data. The fact that the arc rate scales with the density for the higher voltages can also be explained from the dominance of the ion recharging time since this scales directly with density.

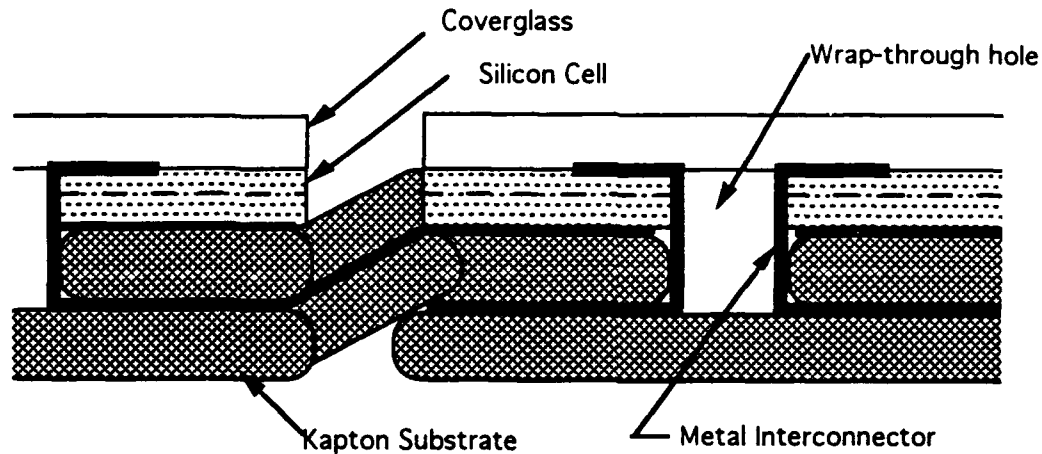


Figure 2.9: Schematic of a wrap-through-contact solar array

2.2 Wrap-Through-Contact Cells

A schematic of a wrap-through-contact (WTC) solar cell is shown in Fig. 2.9. Kapton covers the metal interconnector so it is not exposed to the ambient plasma environment like the interconnectors of conventional cells. One of the reasons for this design was to eliminate arcing at the interconnector-cell interface. On the edge of the cell, however, the semiconductor cell itself is exposed. Since the semiconductor is adjacent to both a dielectric coverglass and a dielectric substrate, arcing can occur. In ground tests, arcing occurred on WTC cells at bias voltages as low as -400V . Consequently, a model is needed to understand how arcing occurs on this type of cell.

As with the conventional cell, the area of interest for studying electric field buildup can be simplified to two dielectrics and a conductor. In this case, the conductor is situated between the two dielectrics as shown in Fig. 2.10. The numerical model for the conventional cells could be modified by a simple change of boundary conditions. The problem is more complex, however, as the conductor is now in the computational domain instead of being merely a boundary condition. In addition, the lower dielectric can not be treated as a simple boundary as the conductor was in the conventional cell model. To properly include the dielectric properties of the substrate, a dielectric of two grid cells thickness is added beneath the conductors and in the gap between the cells. The new geometry also has two triple junctions on each of the two conductor edges, making the previous grid clustering inadequate. The grid is therefore altered to again cluster near the triple junctions as well as along the side surfaces, as shown in Fig. 2.11.

In Section 2.1.1 the results of the ambient ion charging calculated by the PIC scheme

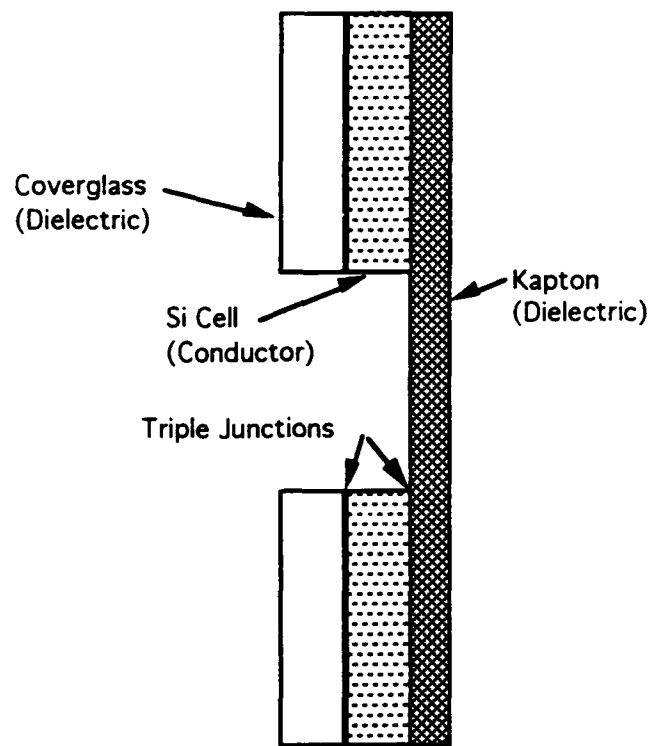


Figure 2.10: Wrap-through-contact solar array model used for numerical simulations

are represented by the electric potential plot (Fig. 2.3) and the surface charge density plot (Fig. 2.4). Corresponding plots for the WTC geometry are shown in Figs. 2.12 and 2.13. As expected, the highest potential value is on the conductor surface with gradients falling off quickly around this voltage source. The gap is sufficiently large that the gradients do not interfere but rather connect at the coverglass surface. The potential lines fall off uniformly beyond the coverglass surface. Above the substrate surface, the potential gradients concentrate near the conductor with potential lines peaking sharply in the center due to the grid configuration. In the coverglass, the potential gradients are curved near the edge of the cell but straighten away from the cell edge.

To simulate the electric field build up, the modified PIC code is run with the enhanced electron field emission (EFEE) charging processes included. The initial conditions are obtained from the results of the ambient ion charging calculations and the enhancement factor, β , for each conductor cell. Due to the high electric potential normal to the conductor surface, much lower enhancement factors ($\beta \approx 30-60$) are used to reduce the number of electrons emitted from the conductor. When too many electrons are emitted, the EFEE charging time is too small, making it less than or on the order of a capacitor charging time. The timestep also affects the number of particles injected into the domain,

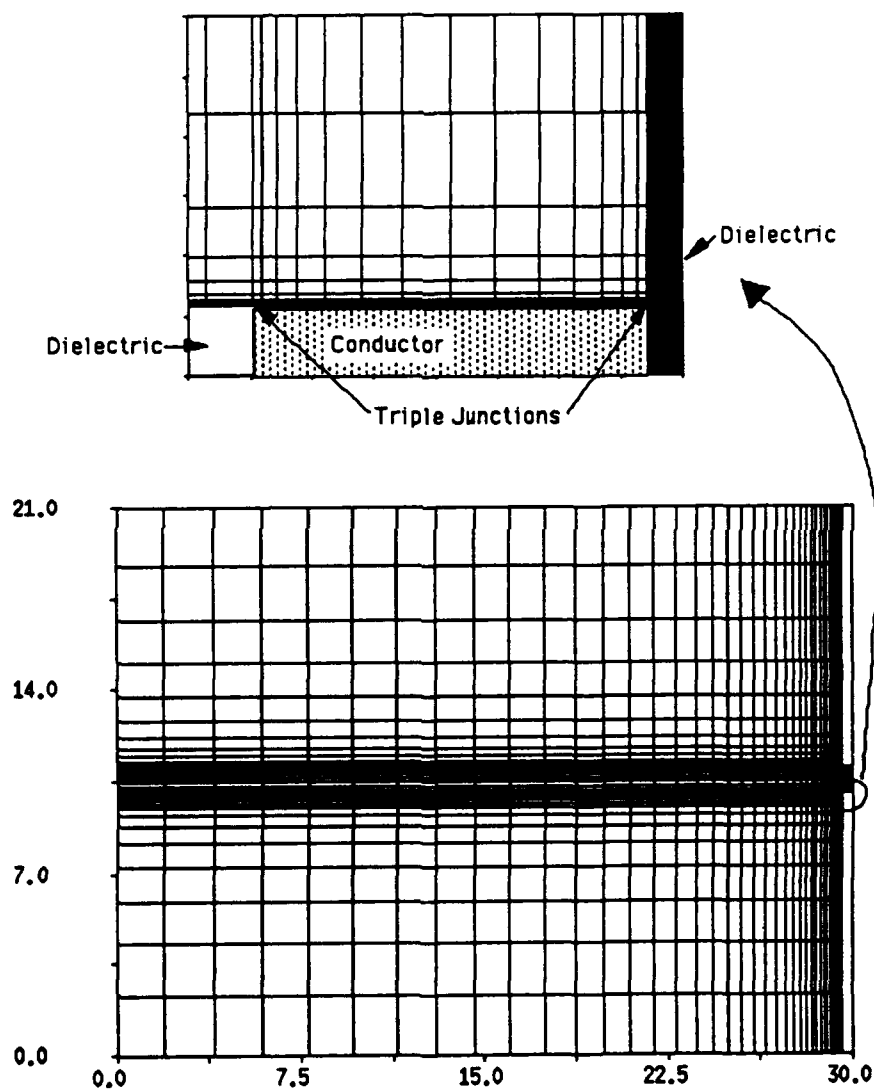


Figure 2.11: Typical grid structure for calculations

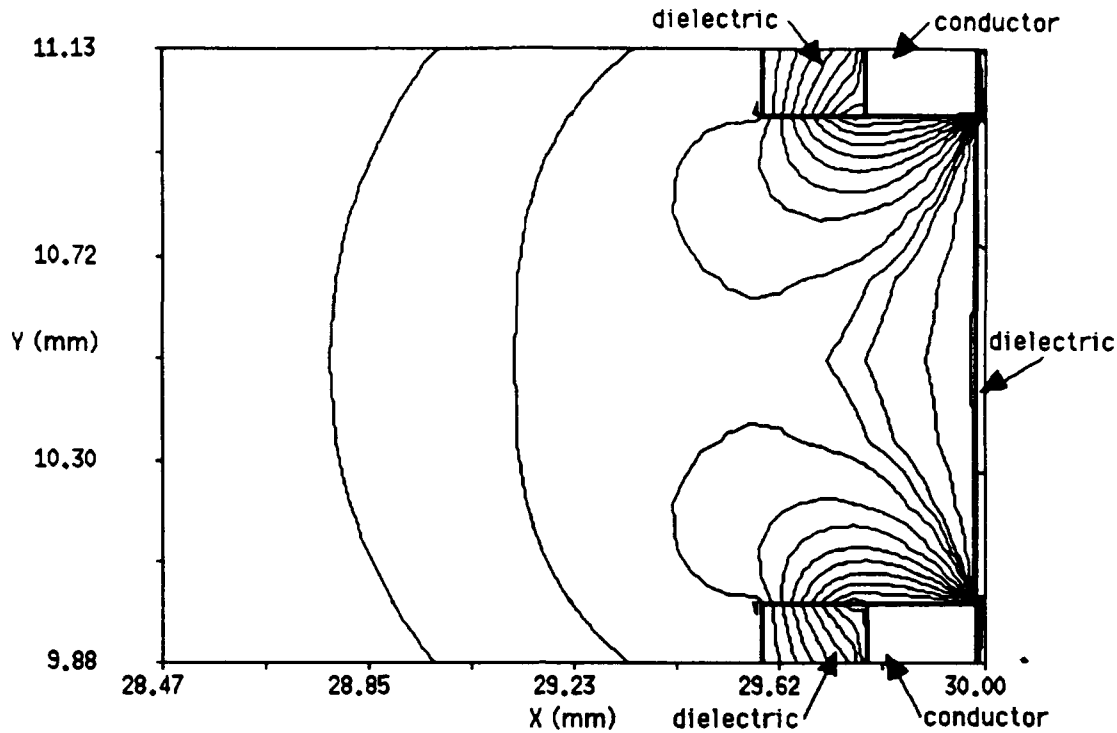


Figure 2.12: Typical electric potential for ambient ion charging of WTC cells

so it is typically chosen to be $\omega_{pe}\Delta t = 0.01$. Larger timesteps can be used when fewer particles are in the domain, which occurs when the electric field at the triple junction has not increased enough for EFEE charging to begin. The PIC code is run until the electric field runs away at one or both of the triple junctions. Since the PIC code automatically accounts for space charge effects, the simulation is often run beyond the electric field runaway into the space charge current limited regime, which limits the electric field magnitude.

The cell properties used for the WTC simulations are based on the Space Station Freedom WTC cell. The coverglass and semiconductor are each $203\mu\text{m}$ (8 mil) thick, and the cell gap is 1mm. The semiconductor is silicon, which has a work function of 4.85eV. The coverglass is assumed to be ceria-doped microsheet (CMX) with a dielectric constant of 4 and secondary electron properties of $E_{max} = 400\text{V}$ and $\gamma_{max} = 4$. The Kapton substrate has a dielectric constant of 3.5 and assumed secondary electron properties of $E_{max} = 300\text{V}$ and $\gamma_{max} = 3$.

The EFEE charging of the WTC cells over the range of 300-500V is distinguished by two classes of behavior, the first occurring with lower β (~ 30) values and the second occurring with higher β (~ 50 -60) values. As seen in Figs. 2.14 and 2.15, the electric

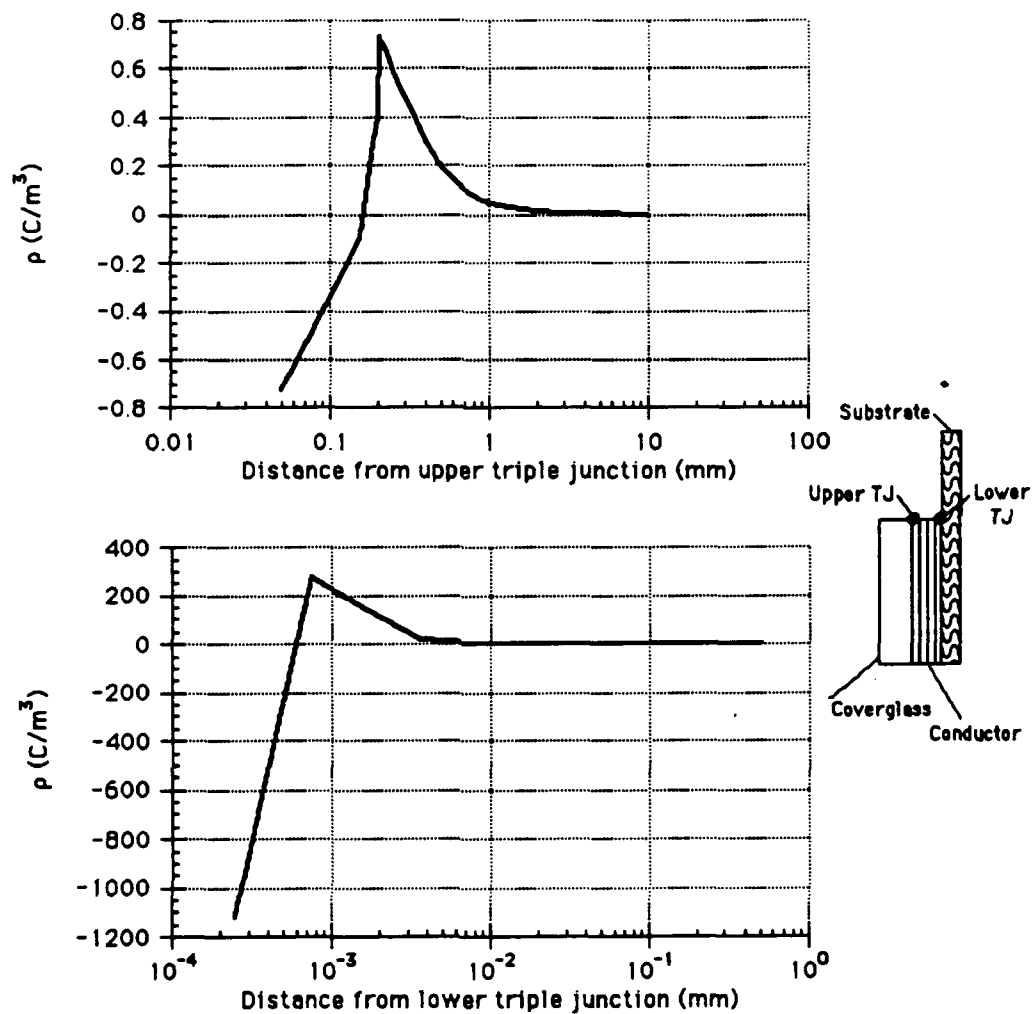


Figure 2.13: Typical surface charge density along the side dielectric surface after ambient ion charging of WTC cells

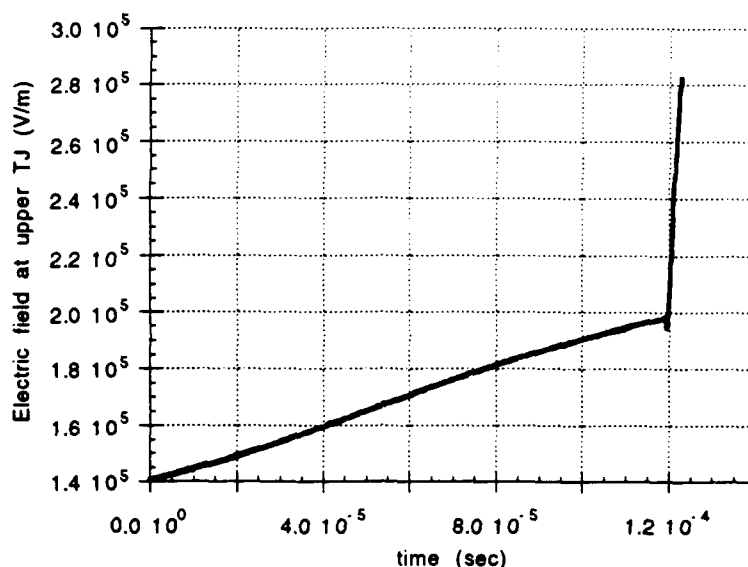


Figure 2.14: Class 1 electric field at upper triple junction versus time

field at the upper triple junction increases initially for the first class and decreases initially for the second class. No runaway occurs at the lower triple junction within this time.

In the first class, the ambient ion charging continues to build up the electric field at the upper triple junction until it is high enough to initiate EFEE charging. Once initiated, the high flux of electrons causes the field to decrease for a short time before the runaway. As shown in Fig. 2.16, the surface charge along the side of the coverglass does not change much during the ambient ion charging, as expected, but also does not change much during the electric field runaway. The surface charge along the front surface, however, does increase substantially, indicating that the electrons from the conductor are striking there and increasing the surface charge through secondary electron emission.

In the second class of behavior EFEE charging begins immediately, emitting many electrons into the domain. Although the surface charge density does increase, as shown in Fig. 2.17, most of the electrons quickly exit the domain without striking any of the cell surfaces. Just prior to runaway, the difference between the number of electrons emitted and the number of electrons impacting the dielectric increases substantially at the same time that the total number of electrons in the domain increases substantially. The electric field then runs away, and the surface charge density along the coverglass side and front surfaces increases significantly.

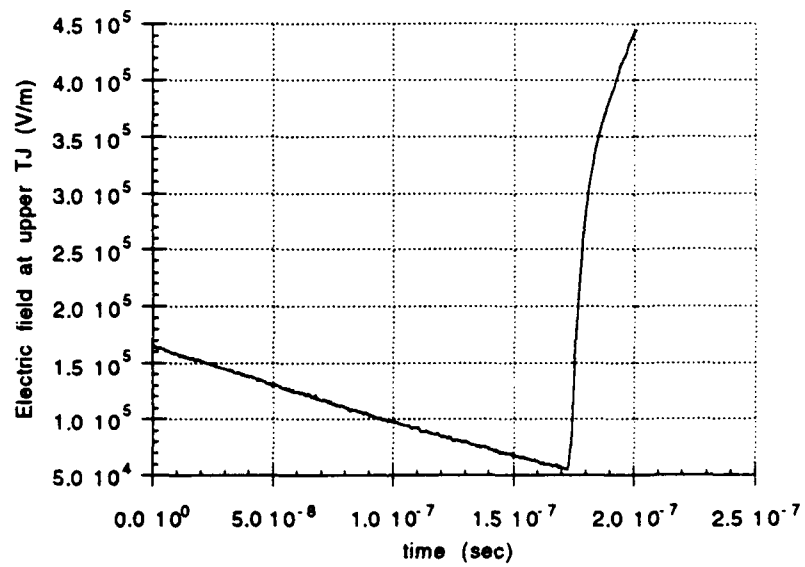
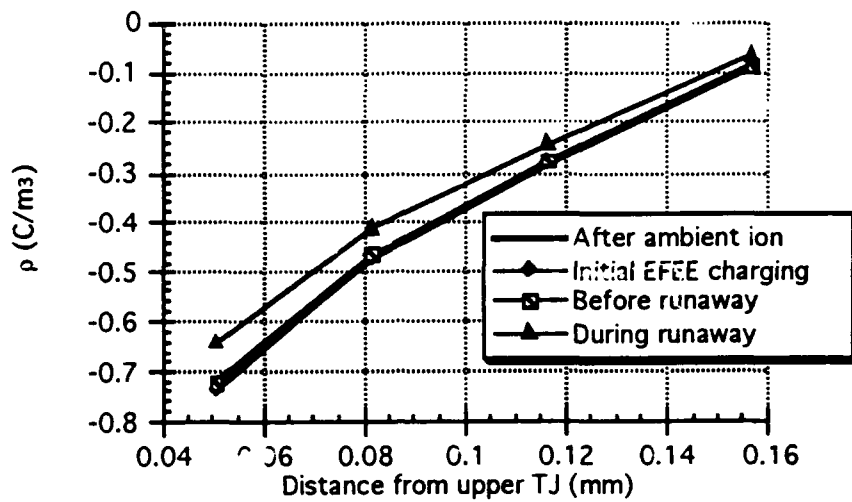
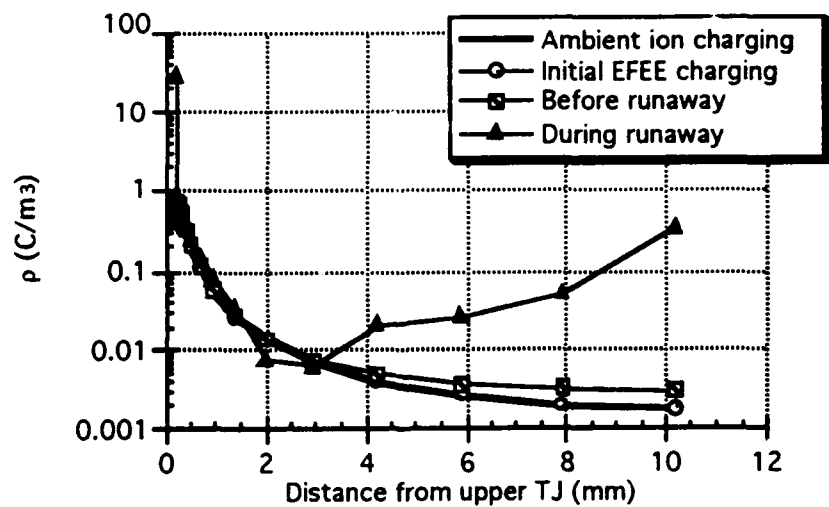


Figure 2.15: Class 2 electric field at upper triple junction versus time



(a) Coverglass side surface



(b) Coverglass front surface

Figure 2.16: Class 1 surface charge density over the coverglass (a) side surface, (b) front surface

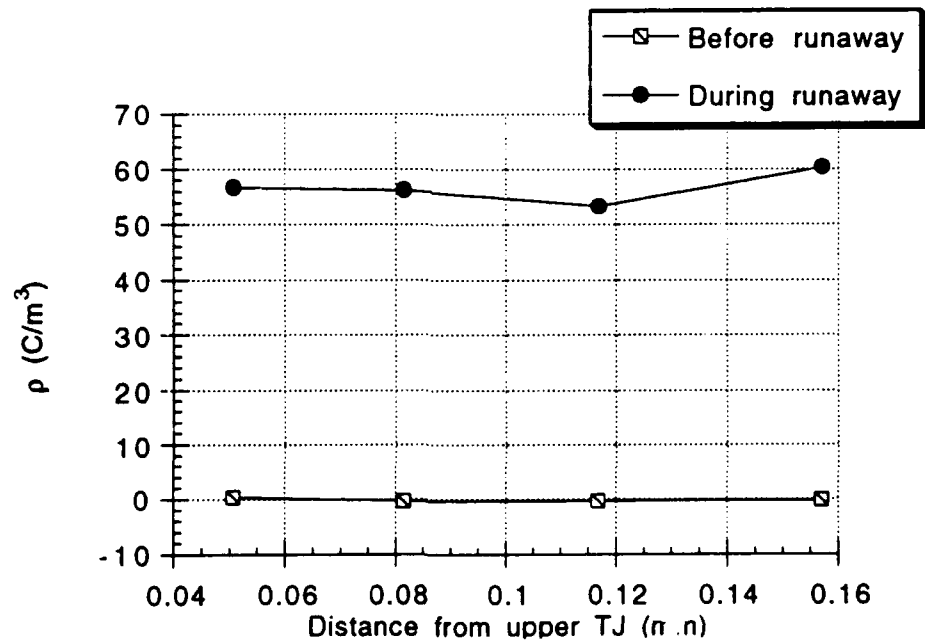
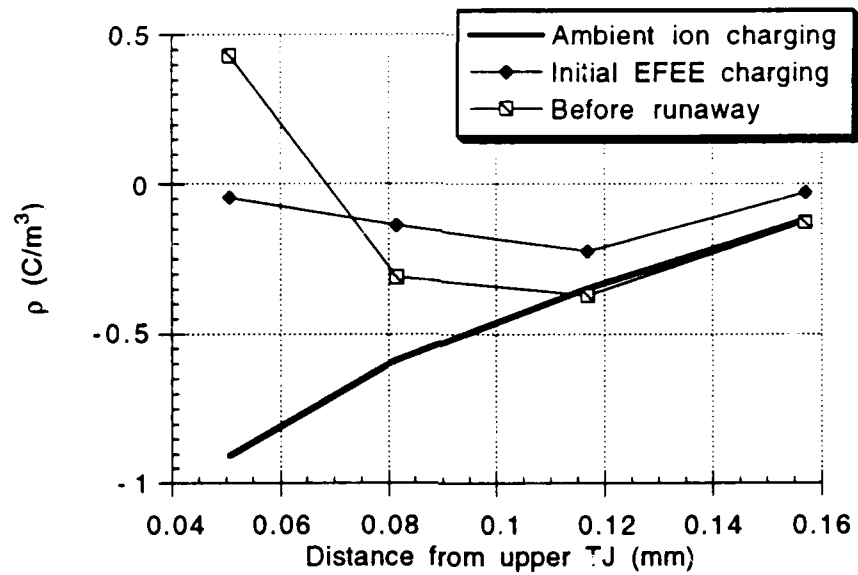


Figure 2.17: Class 2 surface charge density over the coverglass side surface

Chapter 3

Arc Mitigation Methods

In this research several methods of reducing the arc rate were studied. As expressed in Eqn. 1.5, the arc rate is the inverse of the sum of the two charging times, the ambient ion charging time τ_{ion} and the enhanced electron field emission (EFEE) charging time τ_{efee} . Since τ_{ion} is dependent mainly on mission parameters such as the ambient plasma density, arc rate mitigation can only be achieved by increasing τ_{efee} , which is affected by cell properties only. From Eqn. 1.7, the properties which affect τ_{efee} to the greatest extent are those in the exponential factor and the secondary electron yield γ_{ee} , which causes the time to be non-existent if it is equal to or less than unity. In addition, lengthening the coverglass over the interconnector to obstruct the electron trajectories should also increase τ_{efee} , if only by increasing the distance over which the surface charge must build up.

For all numerical simulations described in this chapter, the domain size used is 3mm in the x direction and 2.5mm in the y direction, which includes one-half of two 2mm wide cells and a 0.5mm gap in between them, as shown in Fig. 2.2. The simulations assumed the same environment of $n_e = 5 \times 10^{11} \text{m}^{-3}$, $T_i = T_e = 0.1 \text{eV}$, and a kinetic energy of incoming ions of 5eV, all typical of low earth orbit. A 90° orientation to the ram velocity was used for simplicity. In addition, the emission site on the conductor was set adjacent to the triple junction with an area of $S_{real} = 1.2 \times 10^{-13} \text{m}^2$, as determined by the grid cell length at that location. Since EFEE charging is dependent on an emission site near the triple junction, this condition should define the upper bound for τ_{efee} .

3.1 Control Case

The cell used as the control case for these arc rate simulations is the silicon conventional cell without a coverglass overhang. The input parameters chosen to simulate this cell are shown in Table 3.1. The dielectrics are a fused silica coverglass and DC 93500 adhesive,

Table 3.1: Conventional silicon cell data used in numerical simulations

d_1	0.153mm
d_2	0.037mm
ϵ_{d_1}	3.5
ϵ_{d_2}	2.7
γ_{max1}	3.46
γ_{max2}	3.0
E_{max1}	330V
E_{max2}	300V
d_{gap}	0.5mm
ϕ_w	4.76eV

and the interconnector material is Kovar. The interconnector work function is taken to be the weighted average of the work functions of the elements which compose it. The dielectric thicknesses are typical values.

To determine the effect of varying each parameter, two calculations are made. First, the numerical code discussed in Section 2.1.1 is used to determine τ_{efee} over a range of typically 5 values of βV . The charging time τ_{efee} is then plotted against βV since the analytic theory [9] indicates that τ_{efee} is a strong function of βV . This plot is shown in Fig. 3.1 for the control case over a relevant range. Times less than 1×10^{-8} sec are not useful as that interval is on the order of a capacitor build-up time. Times greater than 1×10^4 sec are also not useful as either the ion charging time would dominate or the orbit would be completed, causing the power system to regenerate. In the following property variations, however, the same range of βV is maintained where possible to simplify comparisons.

Second, the analytical model discussed in Section 2.1.2 is used to determine the arc rates. In this model, the arcing time is determined by the one emission site on a conductor of typically 1000 sites which has the shortest charging time of all the cells. This is a more realistic simulation than the numerical simulations in which only the effect of one site on one conductor was studied. Hence, the effects determined by the numerical simulations often do not have as much impact on the arc rate results as one might expect. The experiment time is also a consideration, particularly for lower voltages where arcing takes a longer time to occur. For the control case and the mitigation cases the experiment

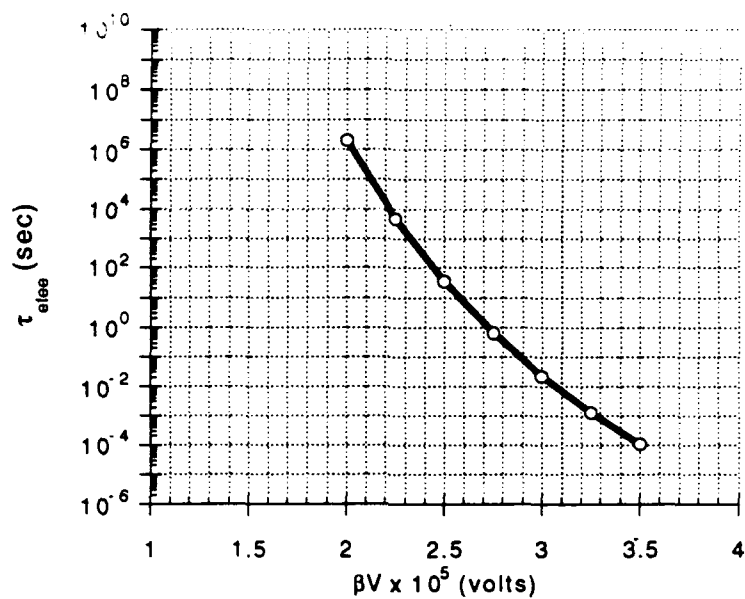


Figure 3.1: Enhanced field electron emission charging time, τ_{elec} , versus βV for the silicon conventional control case

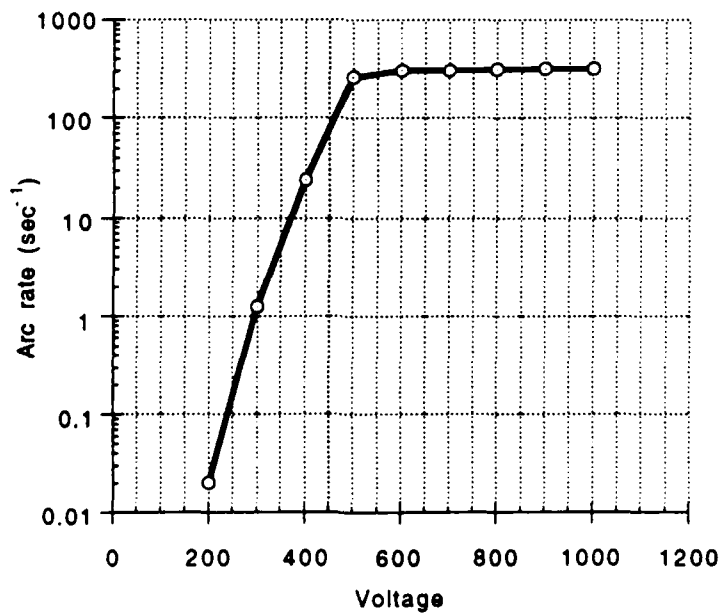


Figure 3.2: Analytic arc rates for the silicon conventional control case

time is arbitrarily chosen to be one second. Also, arc rates are calculated at intervals of -100V. The arcing rates for the control case are shown in Fig. 3.2. The curve clearly shows the two dominating regions of τ_{efee} and τ_{ion} . At lower voltages, τ_{efee} dominates and the arc rate is a strong function of the voltage. At higher voltages, τ_{ion} limits the arcing rate to the value determined by mission parameters, which is a weak function of the voltage. Consequently, the arc rate mitigation methods studied are intended to shift and alter the slope of the τ_{efee} dominated region. The τ_{ion} dominated region can also be shifted though it will remain at the same arc rate. The arc rate results are presented at the end of the chapter in a separate section so that comparisons may be made among all methods studied.

3.2 Interconnector Material

The work function of the electron emitting surface determines the ease with which electrons are released. If the number of electrons emitted from the interconnector is reduced, the time for the electric field at the triple junction to build up will be increased. In the analytical formula for τ_{efee} , the work function determines the value of the Fowler-Nordheim coefficients A and B given by Eqns. 1.8 and 1.9. Fig. 3.3 shows τ_{efee} plotted against βV over a range of significant values for varying work functions. As expected metals with work functions higher than the control case of 4.76eV have longer times for EFEE charging, and metals with lower work functions have shorter times.

These numerical simulation results can easily be predicted from the theory. To determine the effect of a different work function ϕ_{w_2} , we can solve the ratio $\tau_{efee}(\phi_{w_2})/\tau_{efee}(\phi_w)$ using Eqn. 1.7:

$$\frac{\tau_{efee}(\phi_{w_2})}{\tau_{efee}(\phi_w)} = \exp \left((\phi_{w_2}^{1.5} - \phi_w^{1.5}) \frac{6.53 \times 10^9 d}{\beta V \eta \xi_0} \right) \quad (3.1)$$

The only unknown variable is η , which is within the range 1.001-1.005 for emission sites adjacent to the triple junction. For the cases shown in Fig. 3.3; this expression is evaluated and plotted with the equivalent numerical values in Fig. 3.4. The predictions are all within the margin of error for the analytical and numerical values, except for the extreme case of $\phi_w = 5.9\text{eV}$ which is predicted about an order of magnitude too high. This is therefore a useful tool for predicting the effect of changing the exposed interconnector metal.

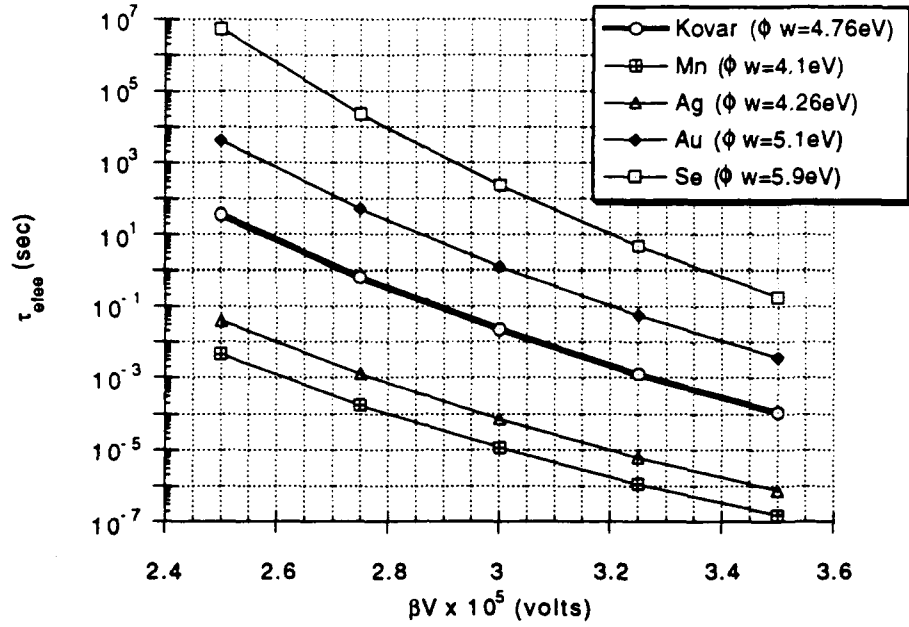


Figure 3.3: Enhanced field electron emission charging time, τ_{efe} , versus βV for different work functions, ϕ_w (eV)

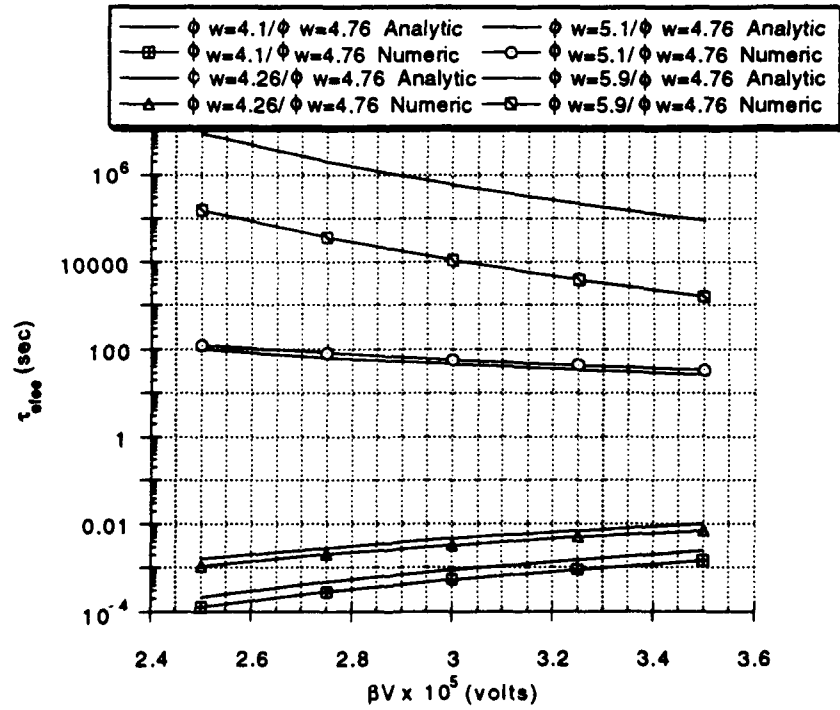


Figure 3.4: Analytic predictions and numerical results for $\tau_{efe}/\tau_{efe}(\phi_w = 4.76 eV)$ versus βV

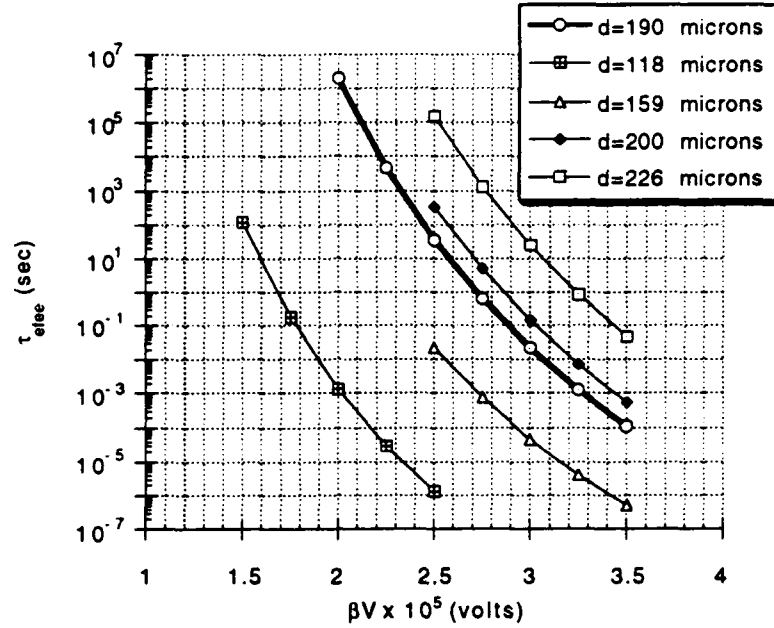


Figure 3.5: Enhanced field electron emission charging time, τ_{efee} , versus βV for different dielectric thicknesses, $d(\mu m)$

3.3 Dielectric Thickness

Another method of reducing the arc rate is to increase the dielectric thickness, $d = d_1 + d_2$. This increases the surface on which charge can accumulate and reduces the average charge density. The analytic theory [9] accounts for changes in thickness in the exponential factor of τ_{efee} . The exponential factor also includes ξ , which is dependent on the ratio of dielectric thicknesses, d_1/d_2 . In order to exclude this factor, the ratio is the same for each case studied. Further simulations which studied the effect of this ratio showed that it did not alter the results. Fig. 3.5 shows τ_{efee} plotted against βV for the control case and for four cases with differing thicknesses. As expected, increases in thickness increase τ_{efee} significantly.

By calculating the ratio of $\tau_{efee}(d + \Delta d)/\tau_{efee}(d)$ using Eqn. 1.7, the change in τ_{efee} can again be easily predicted:

$$\frac{\tau_{efee}(d + \Delta d)}{\tau_{efee}(d)} = \exp \left[\left(\frac{d + \Delta d}{d} \right) \left(\frac{B}{\beta V \eta \xi_0} \right) \right] \quad (3.2)$$

The analytic results are plotted with the numerical results in Fig. 3.6. The predictions are all within the accuracy of the numerical simulations. The prediction for the largest

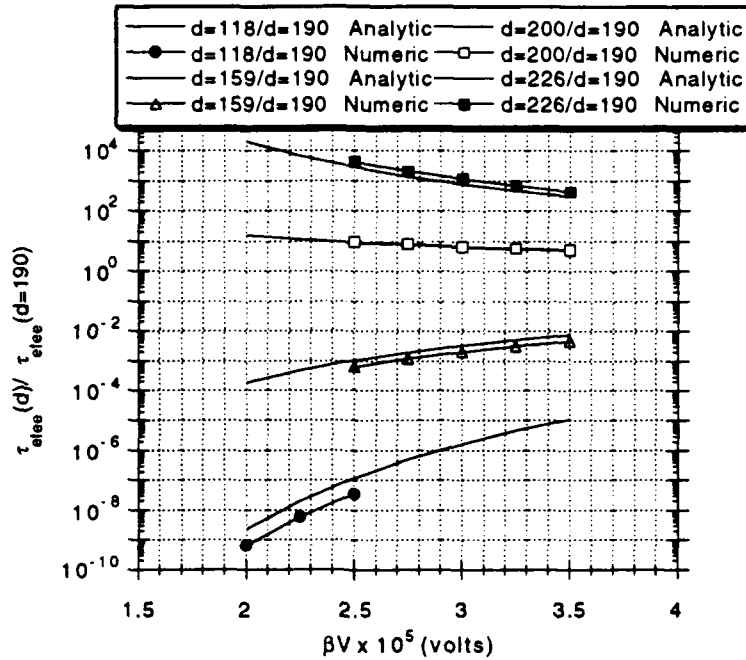


Figure 3.6: Analytic predictions and numerical results for $\tau_{e_{ree}}/\tau_{e_{ree}}(d = 190\mu m)$ versus βV

variation of $d = 118\mu m$ is only off by a factor of 3. Using the same control case, an increase in thickness to $250\mu m$ would result in an increase in $\tau_{e_{ree}}$ of nearly 6 orders of magnitude. This will effectively eliminate electric field run away. Meanwhile, a decrease in thickness to $50\mu m$ would result in a decrease in $\tau_{e_{ree}}$ of nearly 14 orders of magnitude. In this case the arcing rate will be dominated by the ion recharging time, τ_{ion} . These results indicate that the new thinner solar cells such as Advanced Photovoltaic Solar Array (APSA) will experience higher arcing rates at relatively low voltages.

3.4 Secondary Electron Yield

The secondary electron yield, γ_{ee} , from the dielectrics must be greater than unity for the electric field to build up and run away. If γ_{ee} is equal to unity, the electric field will assume a steady state and no charge accumulation will occur. If γ_{ee} is less than unity, the electric field will decrease as negative charge accumulates on the dielectrics. This is modeled in Eqn. 1.7 by the factor $(\gamma_{ee} - 1)^{-1}$.

A sensitivity scan of $\tau_{e_{ree}}$ over relevant values of βV for γ_{ee} values of actual materials is shown in Fig. 3.7. As in the previous sensitivity scans, only the property of interest, γ_{ee} , is varied from the control case. In these cases, γ_{ee} is the same for both dielectrics, although the control case has slightly different values of γ_{ee} for the two dielectric materials, fused

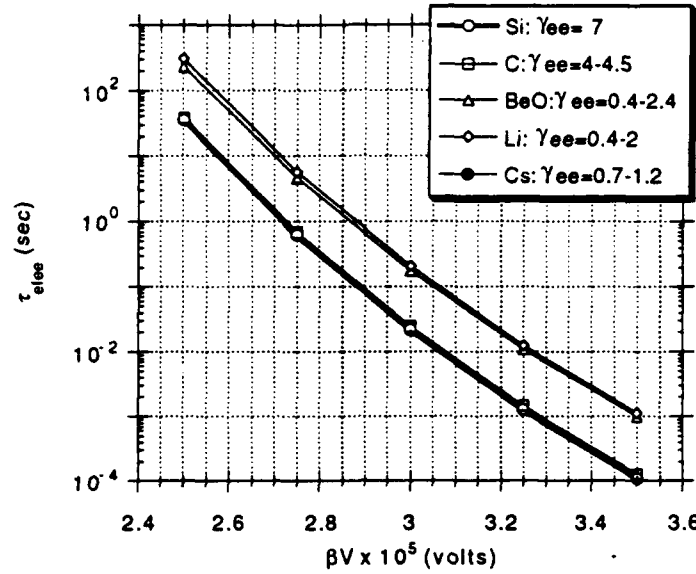


Figure 3.7: Enhanced field electron emission charging time, τ_{efee} , versus βV for different secondary electron yields, γ_{ee}

silica and DC 93500. In order to choose relevant values, the Eqn. 2.24 for γ_{ee} is evaluated for different γ_{max} and E_{max} values determined for actual materials. Since the ambient ion charging is not calculated with secondary electron effects, the initial conditions for EFEE charging are the same as for the control case for every γ_{ee} variation. Consequently, d_i must only be known for the control case to determine γ_{ee} for any other set of secondary electron parameters. From the numerical simulation of the control case, d_i is $35.6\mu\text{m}$, so θ_i is estimated to be 89° , and E_i is estimated to be 75V . For the control case the estimated γ_{ee} is 15, but the numerical results showed γ_{ee} to be 7. In the other cases studied the estimated values of γ_{ee} are also about a factor of 2 higher than the calculated values. The lowest estimated value studied is $\gamma_{ee} = 2.5$ for cesium's properties, but the calculated value is $\gamma_{ee} = 0.7-1.2$. The latter corresponds to the result of no electric field run away by the numerical simulation. The results are shown in Fig. 3.7 with the numerical values of γ_{ee} . As expected, cases with secondary electron yields near unity have much longer EFEE charging times, and the case (Cs) with γ_{ee} values near and less than unity has an infinite EFEE charging time since the electric field at the triple junction did not run away.

One difference between the analytical and numerical results is the effect of the dielectric surface charge, which is not taken into account in the analytical model. As shown in Fig. 3.8, the surface charge next to the triple junction is negative during EFEE charging

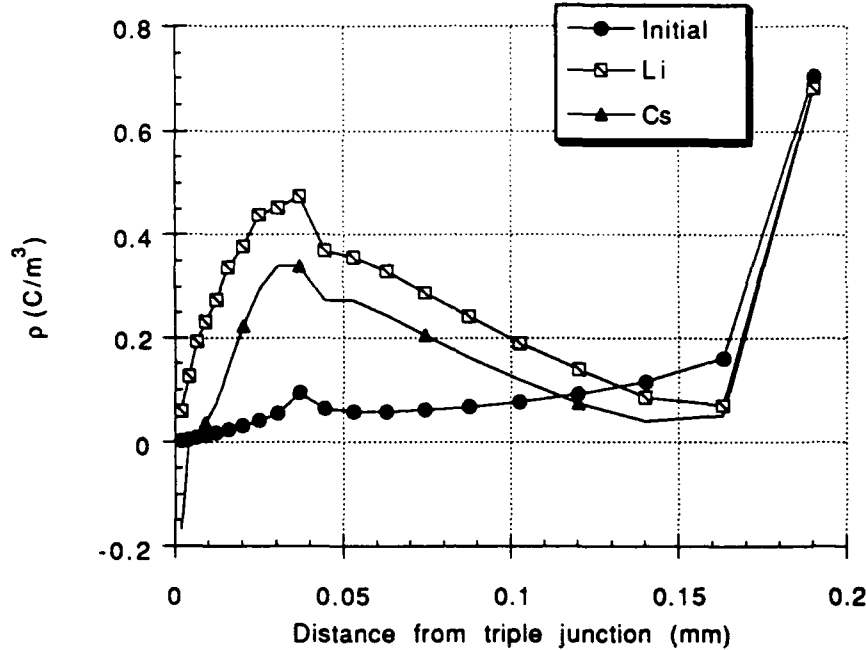


Figure 3.8: Surface charge density as a function of distance from the triple junction for different secondary electron yields, γ_{ee}

for the Cs case of $\gamma_{ee} = 0.7-1.2$, causing the electric field to be unable to run away. In the Li case of $\gamma_{ee} = 0.4-2$, the surface charge builds up over time as it must for the electric field to build up. This surface charge density effect is discussed further in the next section.

3.5 Dielectric Constants

The effect of different dielectric constants is not as apparent in the analytical formula for τ_{efee} (Eqn. 1.7) as for the other cell properties. In the analytical formula, the dielectric constants only directly affect ξ and ξ_0 . The ratio $\epsilon_{d_1}/\epsilon_{d_2}$ in Eqn. 1.10 determines whether ξ_0 is less than, equal to, or greater than 1. Although this does not significantly affect the exponential factor of τ_{efee} , it does affect γ_{ee} through E_i as shown in Eqn. 2.24.

The dielectric constants, however, significantly affect the surface charge density and consequently the secondary electron yield. Since $\epsilon_{d_1}E_1 = \epsilon_{d_2}E_2$, the ratio of dielectric constants, $\epsilon_{d_1}/\epsilon_{d_2}$, must equal the ratio of electric fields, E_2/E_1 . Therefore, if $\epsilon_{d_1}/\epsilon_{d_2}$ is greater than one, the electric field on the lower side surface will be higher. This

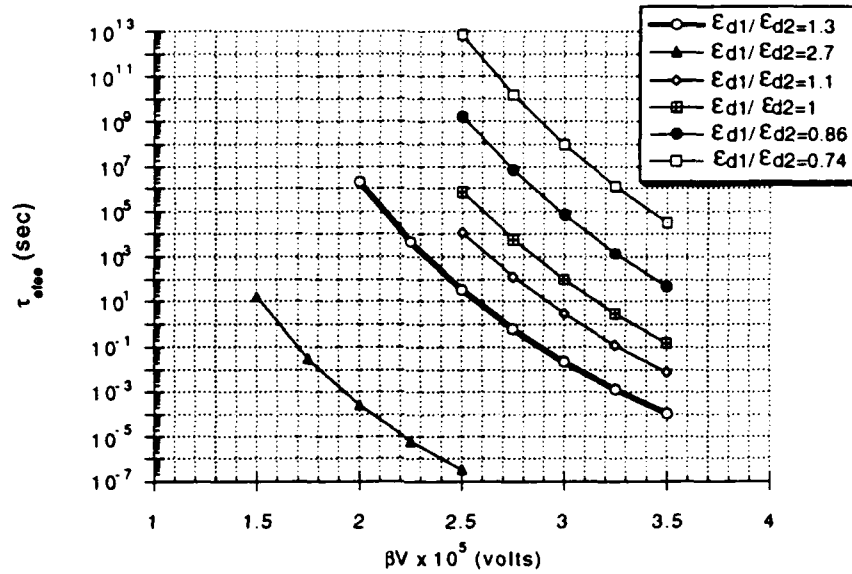


Figure 3.9: Enhanced field electron emission charging time, τ_{efee} , versus βV for different dielectric constant ratios

higher electric field results in a higher surface charge density causing more electrons to be attracted and many more secondary electrons to be emitted. The electric field at the triple junction should then build up quite rapidly causing τ_{efee} to be relatively short. If $\epsilon_{d1}/\epsilon_{d2}$ is less than one, the electric field on the lower surface will be lower than the electric field on the upper surface, causing it to be very difficult for the electric field to build up at the triple junction. The EFEE charging time should then be very long.

The effect of the surface charge density is not accounted for, however, as the analytic expressions do not predict the large variation of τ_{efee} calculated by the numerical simulations. The results are shown in Fig. 3.9. By increasing the ratio $\epsilon_{d1}/\epsilon_{d2}$ from the control case of 1.3 to 2.7, τ_{efee} decreases by about 7 orders of magnitude. By decreasing the ratio from 1.3 to 0.74, τ_{efee} increases by about 12 orders of magnitude. As expected, these results can be explained by the surface charge density. The numerical results of the surface charge density calculations are shown in Fig. 3.10. For higher values of $\epsilon_{d1}/\epsilon_{d2}$, the surface charge density is correspondingly high over the lower dielectric side surface. This attracts electrons, as shown in Fig. 3.11, causing the electric field to run away in a short time. For the control case, the surface charge density does not build up as high before EFEE charging so τ_{efee} is longer. Correspondingly, the electron trajectories are not as concentrated near the triple junction, as shown in Fig. 3.12. For cases with

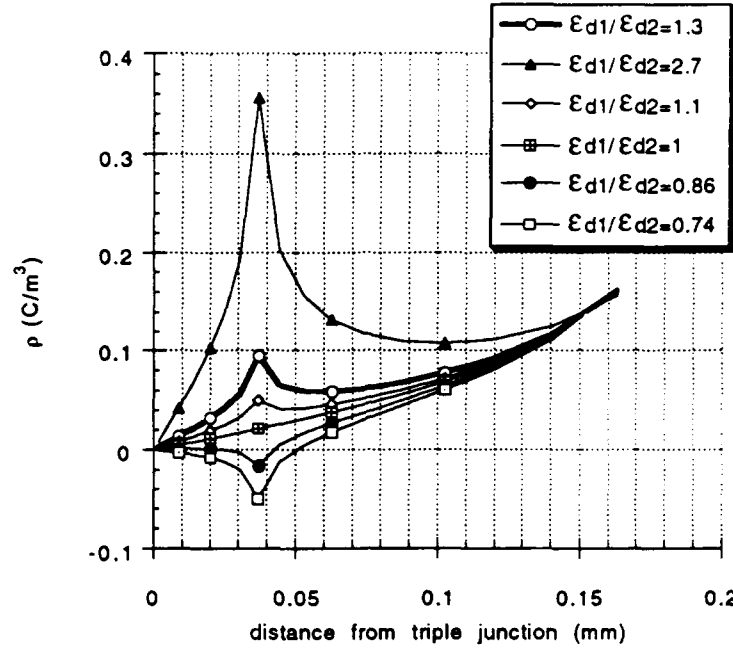


Figure 3.10: Dielectric side surface charge density before EFEE charging for different dielectric constants

$\epsilon_{d1}/\epsilon_{d2} < 1$, the surface charge density over the lower dielectric side surface is negative before beginning EFEE charging so that electrons are repelled from the adhesive, as shown in Fig. 3.13, causing secondary electron emission to be substantially reduced. For these latter cases the useful secondary electron yield is near or below 1, so that the electric field assumes a steady state which does not run away in any reasonable time.

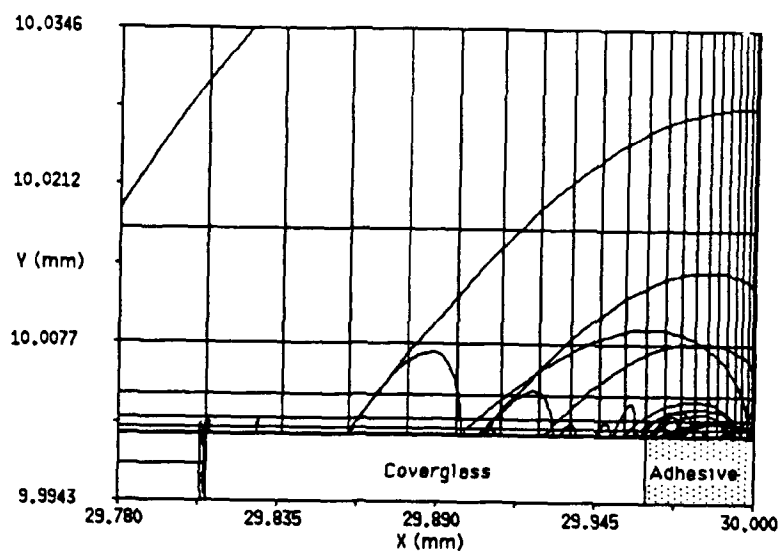


Figure 3.11: Electron trajectories for $\epsilon_{d1}/\epsilon_{d2} = 2.7$

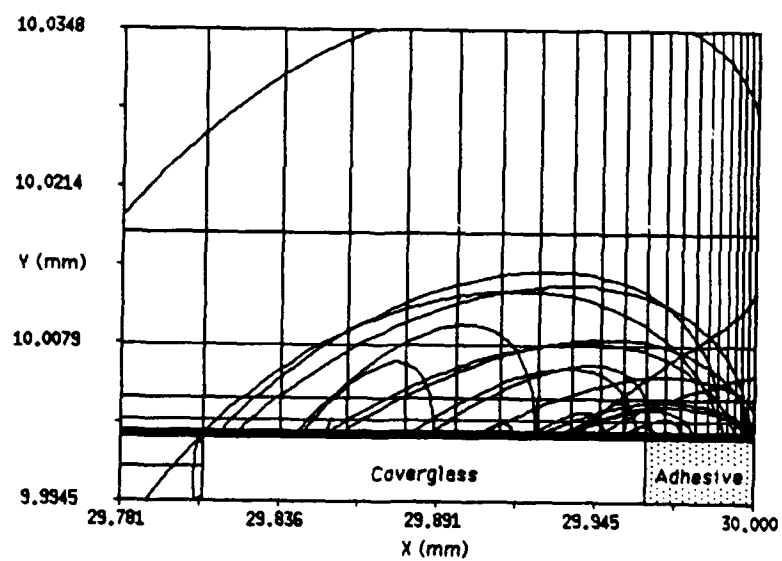


Figure 3.12: Electron trajectories for the control case of $\epsilon_{d1}/\epsilon_{d2} = 1.3$

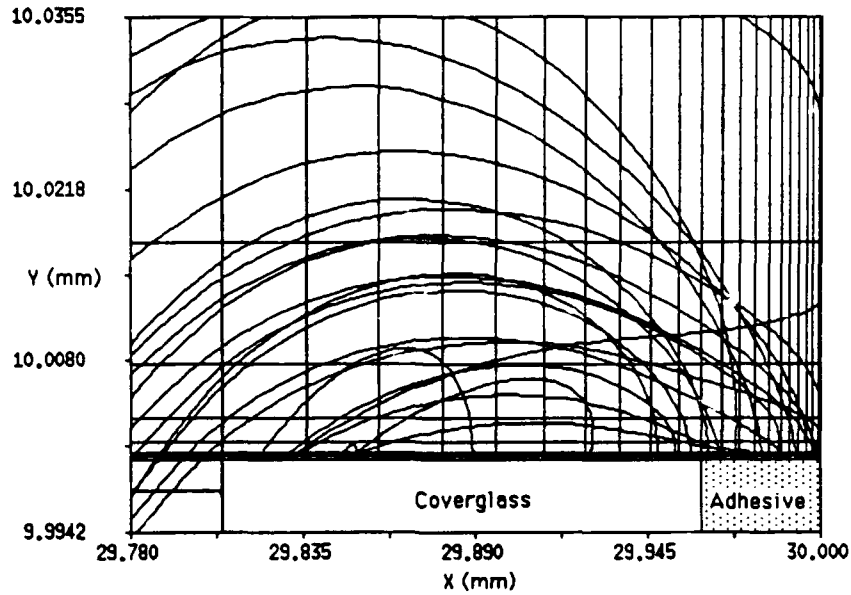


Figure 3.13: Electron trajectories for $\epsilon_{d1}/\epsilon_{d2} = 0.74$

The effects on the secondary electron yield as calculated by the numerical simulations can be seen in Fig. 3.14. As expected from the surface charge density results, γ_{ee} for cases with $\epsilon_{d1}/\epsilon_{d2} < 1$ is significantly lower than for the other cases.

3.6 Overhanging the Coverglass

The final mitigation strategy studied involves lengthening the coverglass into an overhang over the interconnector to create a back surface, as shown in Fig. 3.15, on which charge can accumulate. This method was expected to increase τ_{efee} since the overhang creates an additional surface over which the charge must build up for the electric field to run away.

3.6.1 Numerical Results

As shown in Fig. 3.16, the results confirm this expectation. As the overhang is increased in length up to $30\mu\text{m}$, τ_{efee} is increased uniformly. In the βV range studied, this pattern changes for overhangs longer than $30\mu\text{m}$, indicating a different physical effect of the overhang on the EFFE charging time.

The difference between these two classes is clearly shown in Fig. 3.17. The electric field at the triple junction E_{TJ} increases with time for the the first class, indicating a

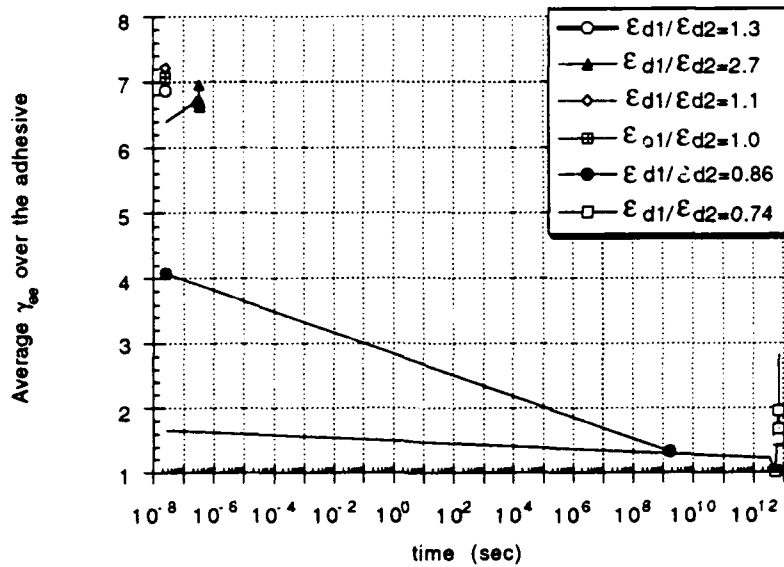


Figure 3.14: Average secondary electron yield over the adhesive versus time for different dielectric constants

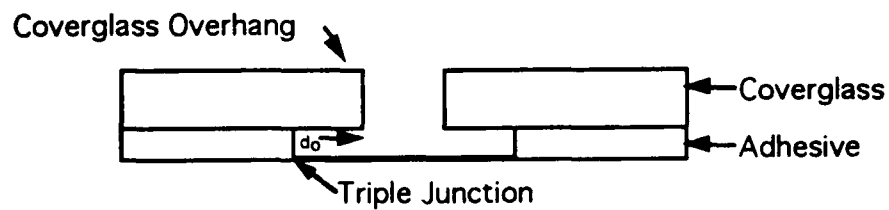


Figure 3.15: Model of coverglass overhang

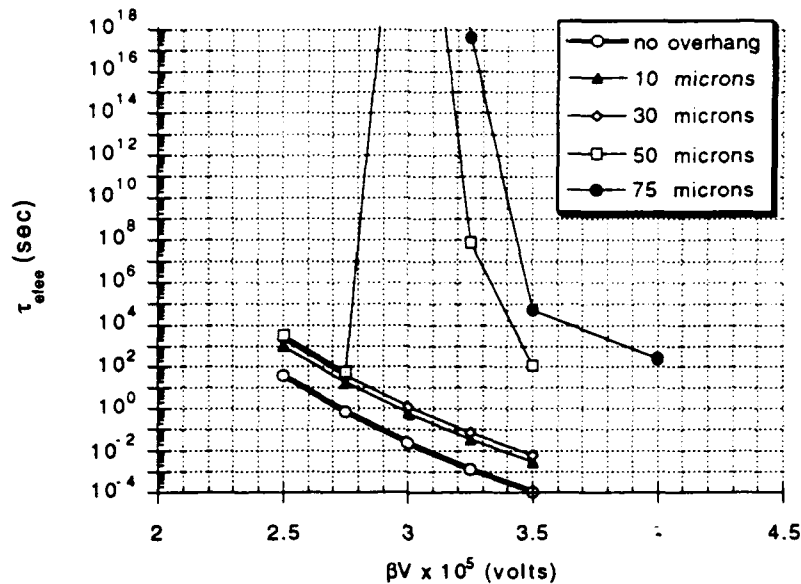


Figure 3.16: Enhanced field electron emission charging time, τ_{efe} , versus βV for different overhang lengths

build up of charge due to EFEE and secondary electron emission. However, it decreases initially before increasing, often drastically, for the second class, indicating an initial build up of negative charge from electron accumulation before electron emission from the side surface becomes high enough to create the positive charge build up necessary for runaway.

The corresponding effects of these differing electric fields on the electron trajectories can be seen in Figs. 3.18 and 3.19. The first shows that the electrons in the first class of simulations are merely diverted by the overhang. The second shows that the electrons in the second class are mainly confined to the back surface with few arriving at the side surface of the coverglass. This shows that the first class of overhangs are acting as additional surface area while the second class are obstructing the electron trajectories to the side surface.

The potential along the surface reflects these electron trajectories. Fig. 3.20 shows that for the first class the potential along the back surface increases with time, which causes the electric field at the triple junction to increase with time as well. For the second class, shown in Fig. 3.21, the back surface potential initially decreases with time until it eventually increases at very large times. This initial potential decrease corresponds to

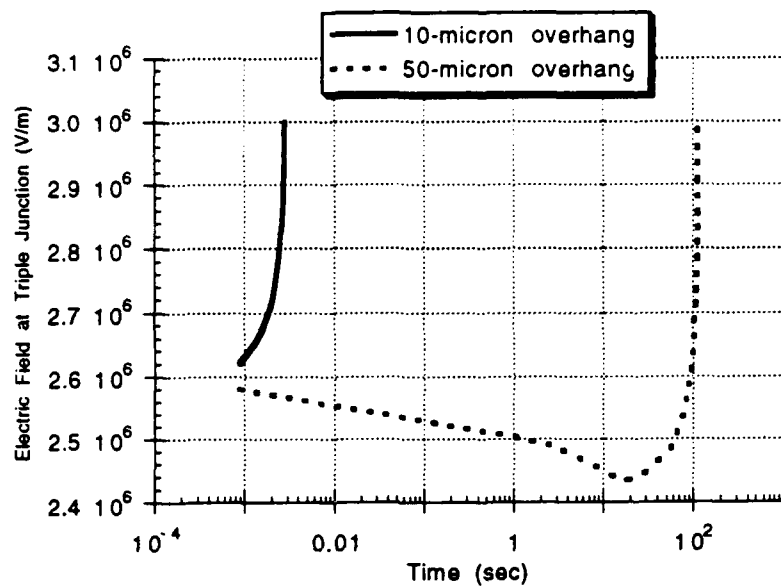


Figure 3.17: Class comparison of τ_{efe} versus E_{TJ} for $\beta V = 3.5 \times 10^5 V$

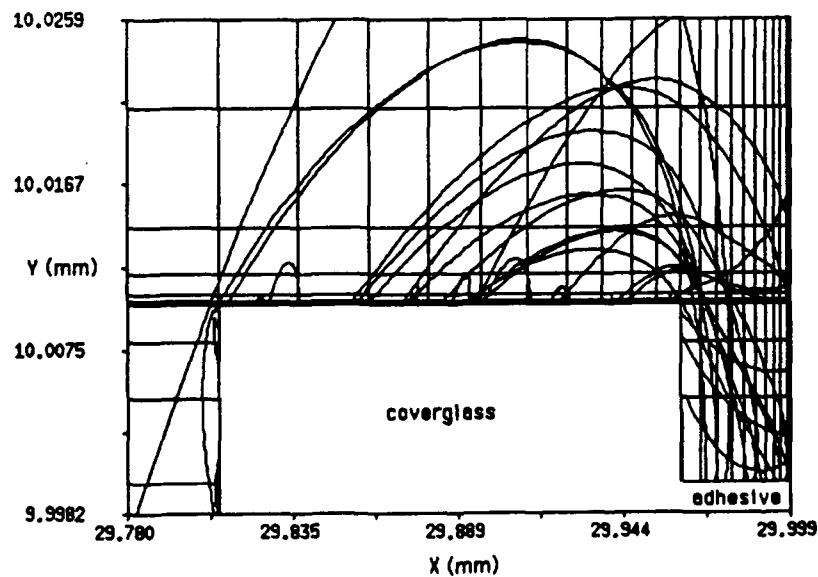


Figure 3.18: Electron trajectories for 10 μm overhang; $\beta V = 3 \times 10^5 V$

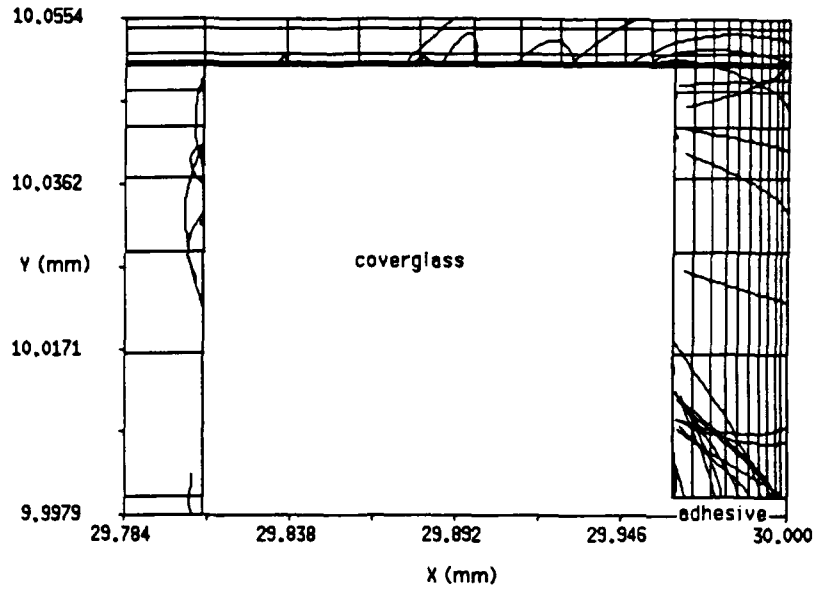


Figure 3.19: Electron trajectories for 50 μm overhang; $\beta V = 3 \times 10^5 \text{V}$

the initial electric field decrease, indicating that the surface is charging negatively due to electron build-up rather than positively due to high secondary electron emission. This is clearly the case as shown in Fig. 3.19, in which almost all of the electrons strike the back surface while very few reach the side surface. Hence the large negative charge on and near the back surface suppresses the electric field, causing it to decrease rather than increase.

3.6.2 Analysis

The results above suggest that there is a critical overhang which determines the behavior of the solution. Below this critical overhang, the electric field runaway is similar to the case of no overhang but at a lengthened time. Above it, the field initially decreases for a long time before building up to the runaway. Hence, coverglasses made longer than this critical overhang will have substantially reduced arcing.

Using the geometry shown in Fig. 1.2, a simple calculation can determine the approximate critical overhang. Since the electric field is only orthogonal to the conductor and approximately orthogonal to the back surface, the free electron force balance is

$$m_e \frac{dv_x}{dt} = eE_x \quad (3.3)$$

and

$$m_e \frac{dv_y}{dt} \simeq 0, \quad (3.4)$$

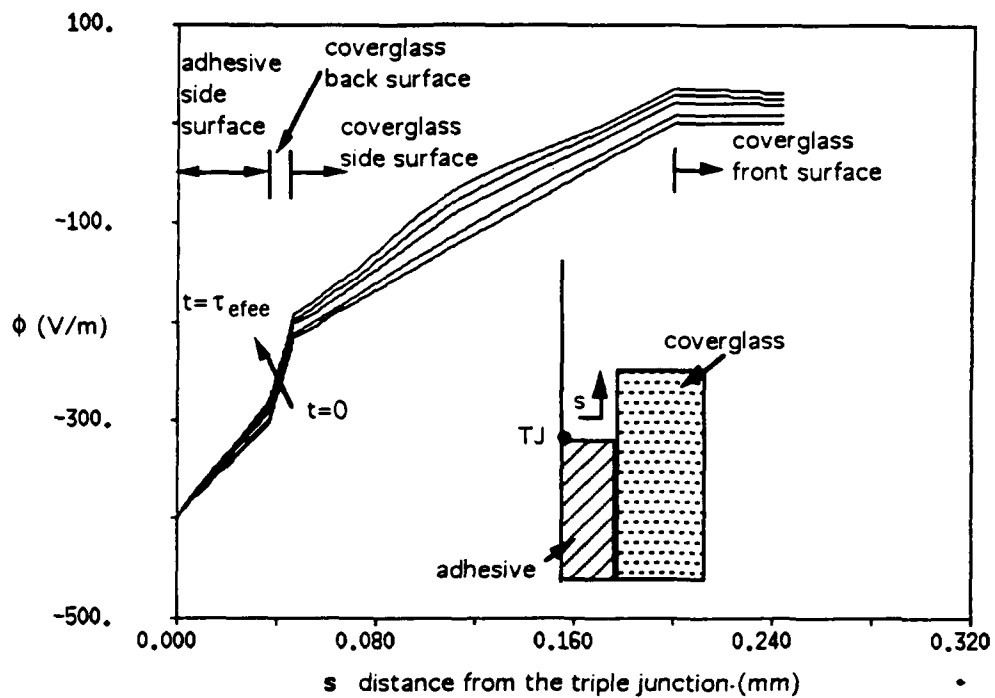


Figure 3.20: Class 1 dielectric surface potential; $\beta V = 3 \times 10^5 \text{ V}$, $d_o = 10 \mu\text{m}$

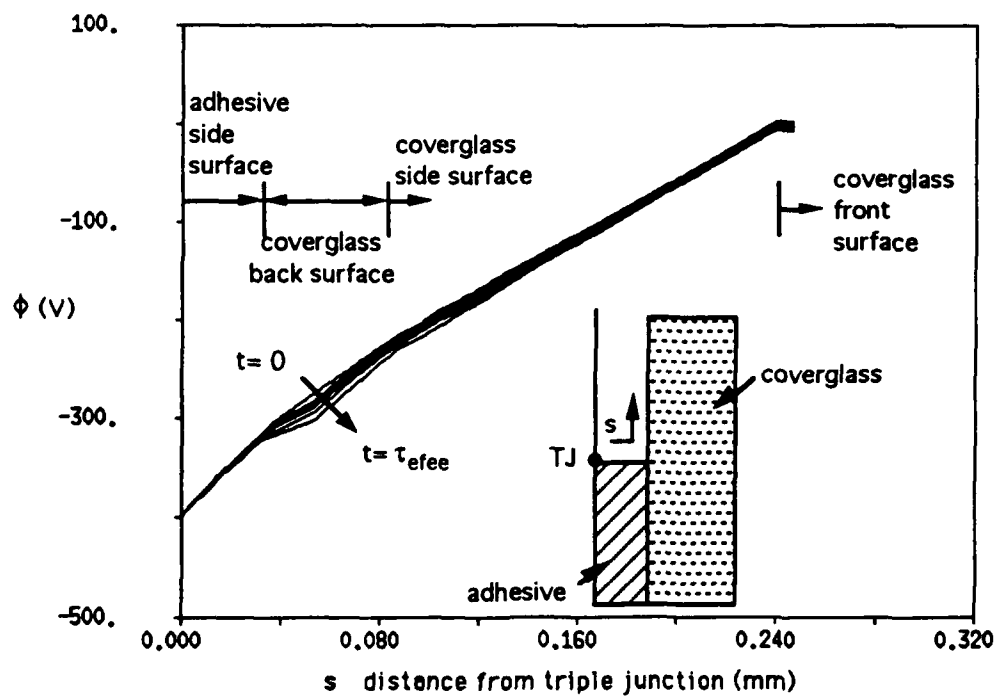


Figure 3.21: Class 2 dielectric surface potential; $\beta V = 3.25 \times 10^5 \text{ V}$, $d_o = 50 \mu\text{m}$

where m_e is the electron mass, v_x and v_y are the electron velocities in the x and y directions respectively, and E_x is the electric field in the x direction.

Electrons emitted from the back surface follow ballistic trajectories according to this electric field. The time to the peak of each ballistic trajectory is

$$t = \frac{v_{x0}}{eE_x/m_e}, \quad (3.5)$$

where v_{x0} is the initial electron velocity in the x direction. The distance the electron travels along the back face before re-impacting the surface is

$$y_t = \frac{2v_{y0}v_{x0}}{eE_x/m_e}, \quad (3.6)$$

where v_{y0} is the initial electron velocity in the y direction.

The electric field E_x can be found from the potential difference between the conductor and the back surface. Assuming the potential of the front surface is zero, the electric fields of the coverglass and adhesive can be expressed as

$$E_1 = \frac{\phi_i}{d_1} \quad (3.7)$$

and

$$E_2 = \frac{\phi_c - \phi_i}{d_2}, \quad (3.8)$$

where ϕ_i is the potential along the interface of the coverglass and adhesive and ϕ_c is the potential of the conductor, or interconnector. At the interface, $\epsilon_{d1}E_1 = \epsilon_{d2}E_2$. By substitution to eliminate ϕ_i and E_1 , both of which are unknown, the following expression is derived for E_2 , or E_x :

$$E_x = \frac{\phi_c}{d_2} \left(\frac{\epsilon_{d1}d_2/\epsilon_{d2}d_1}{1 + \epsilon_{d1}d_2/\epsilon_{d2}d_1} \right). \quad (3.9)$$

Since the critical overhang determines the behavior of the system, the differences between the two classes should be reviewed. For the first class, the electric field at the triple junction increases with time. This means that positive charge is accumulating on the back surface of the coverglass, as shown in Fig. 3.20. Therefore the secondary electrons are escaping from the back surface, as shown in Fig. 3.18. In contrast, in the second class of solutions the electric field is initially decreasing with time; therefore, negative charge is accumulating on the back surface of the coverglass, as shown in Fig. 3.21, so secondary electrons cannot immediately escape the back surface, as shown in Fig. 3.19.

Hence the critical overhang that separates the two solutions can be bounded by requiring that the distance $y_t < d_o$ so that electrons cannot immediately escape and by requiring that the energy $m_e/2v_{y0}v_{x0}$ be bounded by the secondary electron emission energy for

unity yield, \mathcal{E}_1 . This latter requirement means that an electron striking the back surface never has enough energy to release more than one electron. Therefore, the back surface must charge negatively. These two bounds give

$$\frac{d_o^c}{d_2} \leq \frac{4\mathcal{E}_1}{e\phi_c} \frac{1 + \epsilon_{d_1} d_2 / \epsilon_{d_2} d_1}{\epsilon_{d_1} d_2 / \epsilon_{d_2} d_1}. \quad (3.10)$$

For the conditions in Table 3.1, $\mathcal{E}_1 \simeq 40\text{eV}$ and with $\phi_c = 400\text{V}$, Eqn. 3.10 gives $d_o^c \leq 67\mu\text{m}$. This corresponds well with what is observed in Fig. 3.16 where the $50\mu\text{m}$ overhang shows the characteristics of both classes while the $75\mu\text{m}$ overhang shows only the characteristic of the second class.

This approximate expression can be further simplified in the limit $d_2 \ll d_1$ (which is usually the case). Eqn. 3.10 then simplifies to

$$d_o^c \leq \frac{4\mathcal{E}_1}{e\phi_c} \frac{\epsilon_{d_2}}{\epsilon_{d_1}} d_1. \quad (3.11)$$

This shows that one can obtain the smallest critical overhang by reducing d_1 as much as possible, consistent of course with the need to maintain radiation protection, and by modifying the secondary electron emission properties of the coverglass so as to reduce the energy at which the yield is unity.

3.7 Arc Rate Results

The arc rates are determined by using the analytical model discussed in Section 2.1.2, as explained for the control case. This model is limited by the analytic expressions, which are only approximations of real processes and effects. For the results in the previous section which are consistent with the analytic predictions, the model is used with the varying parameters. For the secondary electron yield, dielectric constant, and overhang effects on τ_{efee} , which are not fully accounted for in the analytic expression, the model is used with τ_{efee} modified according to the results from the numerical simulations.

The results are shown in Figs. 3.22-3.26. In all cases the curves saturate around 350sec^{-1} , where the arc rate is limited by τ_{ion} which is not as dependent on voltage as is τ_{efee} . The goal of the mitigation strategies can clearly be seen, then, as increasing the voltage range of τ_{efee} dominance.

The effect of different work functions on the arc rate is shown in Fig. 3.22. None of the work functions significantly affect the arc rate, although the higher work functions do not arc at -200V . Also, little difference is seen between the arc rates of commonly used Kovar and silver interconnectors.

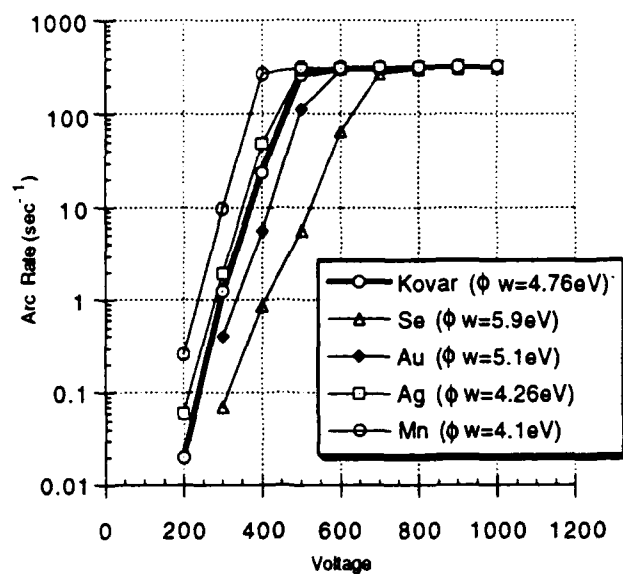


Figure 3.22: Analytic arc rates for varying interconnector work functions, ϕ_w

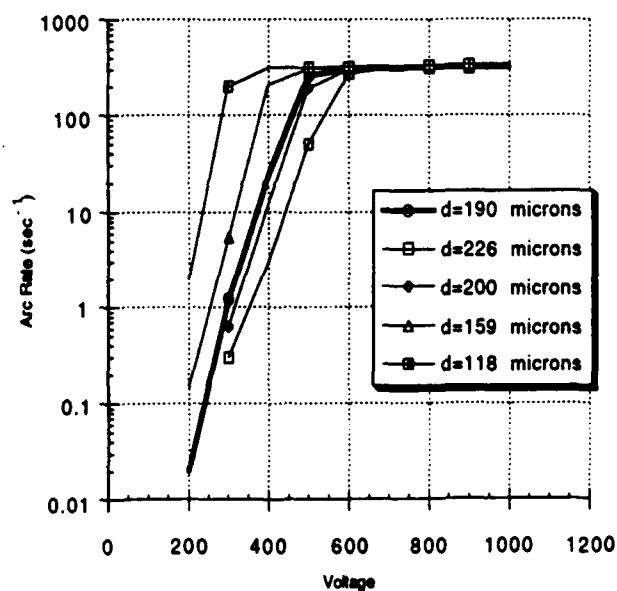


Figure 3.23: Analytic arc rates for varying dielectric thicknesses, d

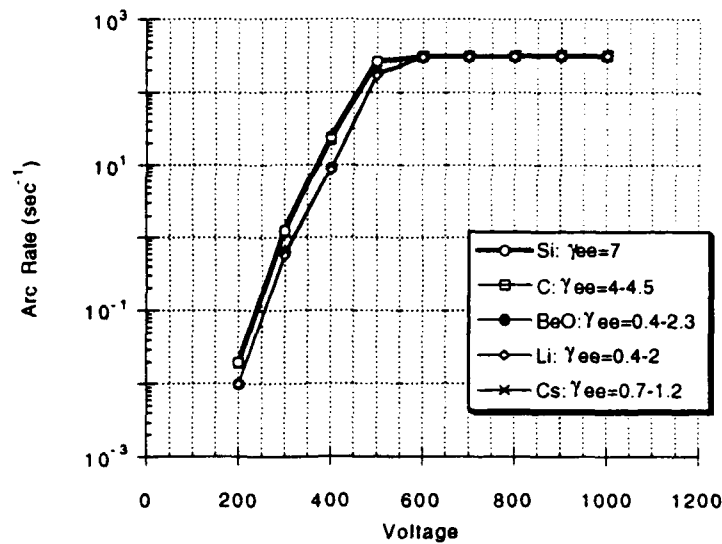


Figure 3.24: Predicted arc rates for varying secondary electron yields, γ_{ee}

The thickness variations show a greater effect on the arc rate, especially for the smaller thicknesses between -200V to -400V. For a $118\mu\text{m}$ thickness of the coverglass and adhesive dielectrics, the arc rate is almost saturated at -300V, while the control case thickness of $190\mu\text{m}$ does not saturate until -600V. Increasing the thickness to $200\mu\text{m}$ or even $226\mu\text{m}$ eliminates arcing at -200V but does not reduce arcing significantly at higher voltages.

The effect of the secondary electron yield on the arc rate is shown to be significant only when the electric field does not run away, as in the $\gamma_{ee} = 0.7-1.2$ case. Even for the two cases (BeO and Li) which have secondary electron yields near and below unity, the arc rate is just barely reduced from the control case. Any secondary electron yield not near unity, such as that of carbon ($\gamma_{ee} = 4-4.5$), did not change the arcing rates at all from the control case of $\gamma_{ee} = 7$.

The dielectric constant variations and coverglass overhang cases show the largest effect on the arc rate. For the $\epsilon_{d1}/\epsilon_{d2} = 2.7$ case, the arc rate is almost saturated at -300V. For the case of equal dielectric constants, however, the arc rate does not saturate until -900V. For variations of $\epsilon_{d1}/\epsilon_{d2} < 1$ the arc rate is reduced significantly. No arcing is predicted until -600V for the $\epsilon_{d1}/\epsilon_{d2} = 0.74$ case.

For the coverglass overhang arc rates, the two different classes can be seen clearly in Fig. 3.26. The arc rates of the first class do not decrease much even with an overhang

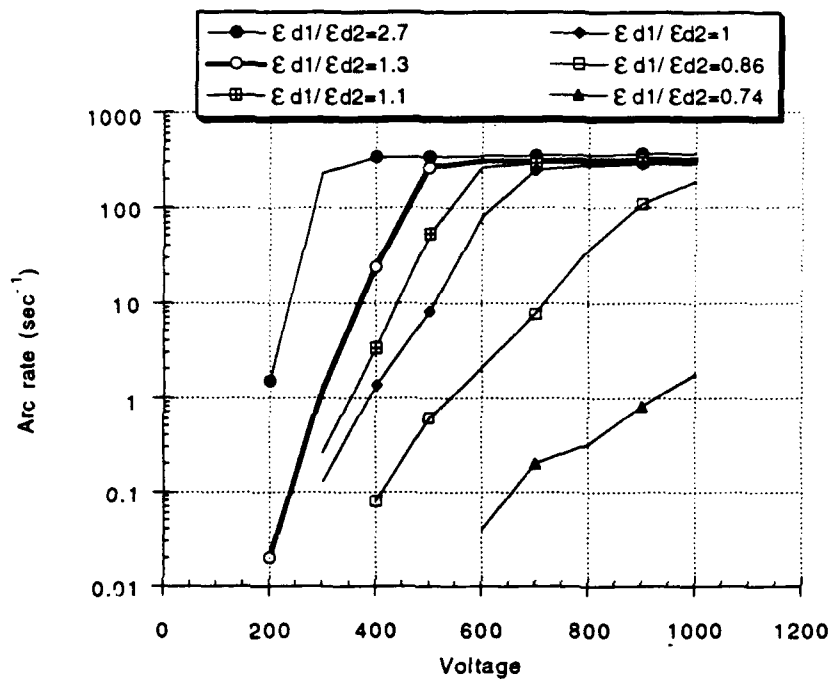


Figure 3.25: Predicted arc rates for varying dielectric constant ratios, $\epsilon_{d1}/\epsilon_{d2}$

of $30\mu\text{m}$, but the arc rates of the second class are significantly reduced. The $75\mu\text{m}$ case, which is beyond the critical overhang for the cell studied, shows no arcing until -600V and does not reach the saturation level in the range of voltages examined.

These predictions will be tested in the upcoming Air Force Photovoltaic and Space Power Plus Diagnostics (PASP Plus) space experiment and the NASA Space Shuttle SAMPIE flight which will overhang the coverglass as well as apply a coating over the triple junction. These experiments are discussed in the next chapter.

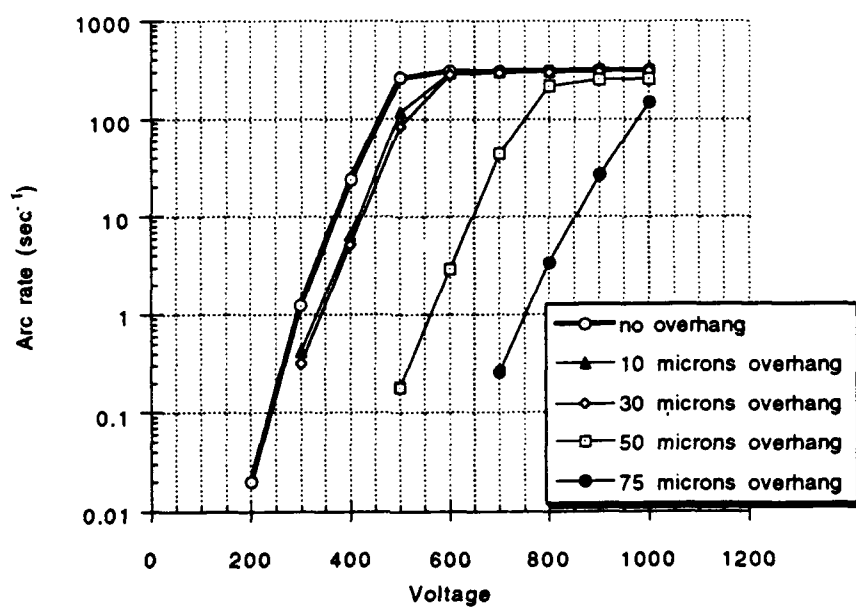


Figure 3.26: Predicted arc rates for varying coverglass overhang lengths, d_o (μm)

Chapter 4

PASP Plus and SAMPIE Predictions

In the next few years, four space missions are planned to study high voltage solar arrays. Two of these are the Photovoltaic and Space Power Plus Diagnostics (PASP Plus) experiment and the Solar Array Module Plasma Interactions Experiment (SAMPIE). By using the numerical and analytical models for the conventional and wrap-through-contact cells, arcing predictions can be made for these missions to aid in their preparation and to further check the validity of these models.

4.1 PASP Plus

PASP Plus is designed to provide the Air Force with important information regarding higher power space systems. Since greater spacecraft power will be required, the Air Force anticipates using advanced high voltage solar arrays and power distribution systems. The environmental interaction hazards of these systems therefore need to be determined to improve the reliability of future missions. To accomplish its task, the PASP Plus experiment includes both advanced solar arrays and a number of diagnostic instruments. PASP Plus has four main objectives[20]:

- (1) characterize the electrical performance and the environmental interaction of advanced solar array designs operating at high voltages in the ionosphere and magnetosphere;
- (2) determine the long-term radiation degradation effects of several advanced solar arrays;
- (3) determine the impact of the space environment on solar array operation for various solar cell technologies; and
- (4) obtain flight performance data for advanced array designs never before flown.

4.1.1 Experiment Description

The PASP Plus experiment will be flown on the Advanced Photovoltaic and Electronics Experiments (APEX) satellite, scheduled to be launched in the summer of 1993 aboard the Pegasus launch vehicle. The satellite should reach an orbit of 1850km apogee, 350km perigee, and 70° inclination. This polar orbit allows the payload to be continuously sun pointing. The experiment is expected to last one year minimum and three years nominal.

The APEX spacecraft in its deployed configuration is shown in Fig. 4.1. The arrays are located on the top shelf and on one of the deployed panels. The other three panels are the solar arrays needed for the spacecraft power system. Beneath the payload shelf is the avionics shelf, where most of the diagnostic instruments are located. There are three types of sensors to obtain array performance data and five types of sensors to characterize the space environment around the spacecraft. To calibrate the performance of the solar arrays, the following instruments will be used: a sun sensor to measure the incidence angle, meters to measure the current and voltage, and sensors near each array to measure the temperature. Instruments which characterize the space environment include a transient pulse monitor for measuring electromagnetic interference, a langmuir probe with sense potential capability for measuring the thermal plasma temperature and density, a dosimeter for measuring ion and electron radiation, an electrostatic analyzer to determine electron and ion spectra of moderate energy (10eV - 30keV), and five monitors for determining the amount of degradation due to radiation and the amount due to contamination. The spacecraft also contains a voltage generator capable of biasing the arrays at multiple high voltage levels, an electron emitter which will enable the satellite's potential to be altered, and an electronics controller for satellite operation.

Seventeen arrays of twelve different types will be mounted on the payload shelf and the deployed panel. Since there are only 16 electrical channels, one of the arrays will not be used. Ten of these arrays will be subject to multiple voltage biasing. The arrays, as well as the instruments described above, are all numbered for identification. They will be therefore introduced in order of their instrument numbers, and the biased arrays will then be described in further detail, with the exception of the concentrator arrays which are not included in this research. Arrays #0, #1, and #2 contain silicon conventional cells. The silicon WTC cells designed for Space Station Freedom make up array #3. Arrays #4 - #6 are Applied Solar Energy Corporation's (ASEC) gallium arsenide/germanium (GaAs/Ge) conventional cells, but array #5 will not be used so that its channel can be used by the APSA cell array. The advanced solar cells of AlGaAs/GaAs Monolithic MBG are on array #7. Spectrolab's WTC GaAs/Ge cells are located on array #8. Array #9 contains

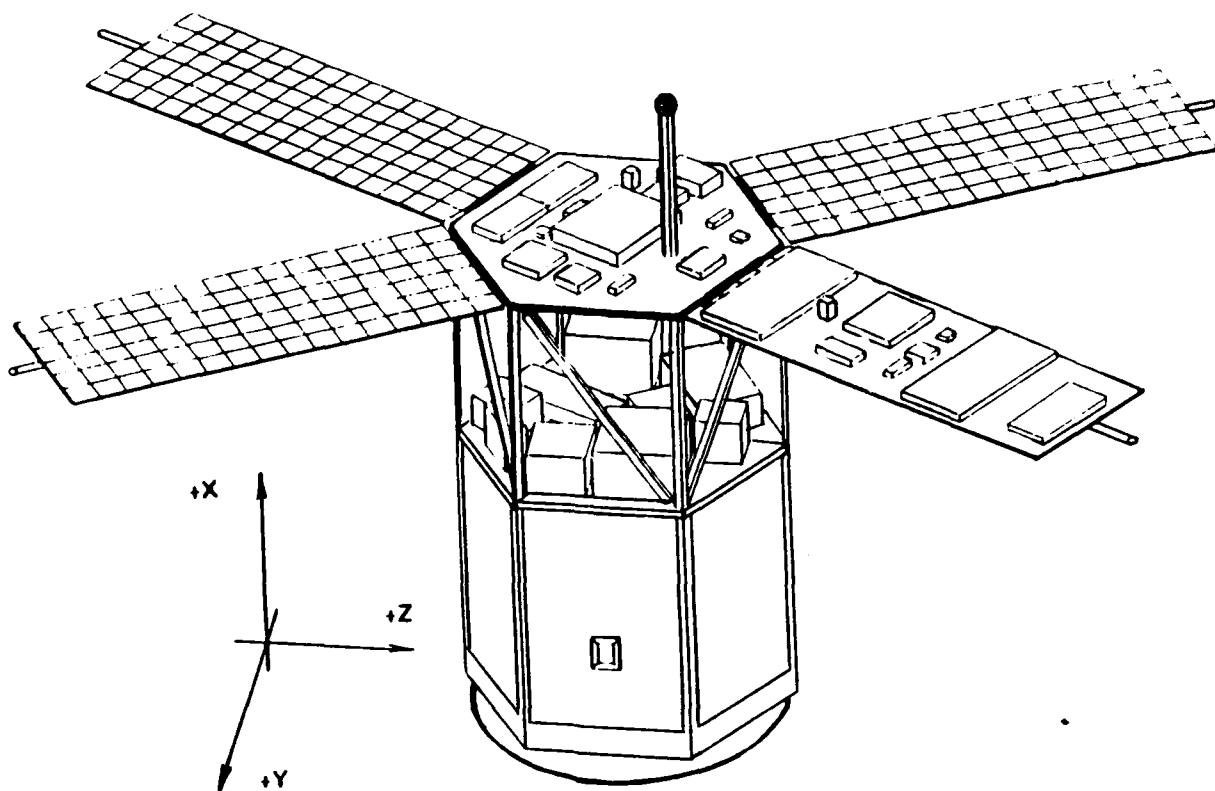


Figure 4.1: Deployed APEX spacecraft with PASP Plus experiment payload

the amorphous silicon cells developed by TRW and Solarex. Another advanced solar cell, indium phosphate (InP), is on array #10. The conventional GaAs/Ge cells made by Spectrolab are on array #11. Another MBG cell, Boeing's GaAs/CuInSe solar cell, make up arrays #12 and #13. The Mini-Cassegrainian GaAs cell created at TRW will be on array #14 to accompany the newer Mini-Dome Fresnel Concentrator created at Boeing which is on array #15. Finally, the APSA cell was added late to the list so its array is #36.

The silicon conventional arrays #1 and #2 are the first biased arrays, containing 10 and 20 cells respectively. Originally built by RCA in 1984, these cells are included to be representative of present operational space flight solar cells. Also, they were not designed to withstand high voltage operation. The cells are $2\text{cm} \times 4\text{cm}$ and $203\mu\text{m}$ (8mil) thick. The coverglass is fused silica and the cover adhesive is DC 93500, of estimated thickness $153\mu\text{m}$ (3mil) and $37\mu\text{m}$ (1.5mil) respectively. The interconnector is assumed to be Kovar, which has an estimated work function 4.76eV.

The Space Station Freedom array of 4 cells (#3) will also be biased. These WTC cells were designed to operate in low earth orbit at a 160V nominal operating voltage. The $8\text{cm} \times 8\text{cm}$ cells are $203\mu\text{m}$ (8mil) thick. As discussed in Section 2.2, the cells are

covered with a ceria-doped borosilicate coverglass and a Kapton substrate.

Arrays #4 and #6 of ASEC's GaAs/Ge conventional cell design are comprised of 20 and 12 cells respectively, and both will be biased. These cells were designed to have high radiation resistance and high cell efficiency, making them representative of the standard for the next generation of satellite photovoltaic power. The 4cm×4cm cells have a thickness of 76 μ m (3.5mil) and CMX coverglasses of 102 μ m (4mil). The interconnector is silver-plated invar so the relevant work function is that of silver, which is 4.26eV.

Both of Spectrolab's arrays, #8 and #11, will be biased. The first array is their WTC design, which is expected to operate better than conventional cell designs at high voltages. The 4cm×4cm cells, which are 177 μ m (7mil) thick, are covered by a 152 μ m (6mil) thick coverglass and mounted on a Ge substrate. The second array contains a similar cell of conventional design. The dimensions of both the cell and coverglass are the same, and the adhesive is estimated to be 76 μ m (3mil) thick. Like the ASEC GaAs/Ge cells, these cells also have a silver-plated invar interconnector.

The Advanced Photovoltaic Solar Array (APSA) is the final high voltage biased array studied. These thin-film silicon cells are expected to be the cells of the future, based on the mass cost savings they yield. Built by TRW, they are 2.6cm×5.1cm of only 56 μ m (2.2mil) thickness. More importantly for arcing considerations, the cell CMX coverglass thickness is merely 51 μ m (2mil) thick and the DC 93500 cover adhesive is estimated to be 76 μ m (3mil) thick. The interconnector is again silver-plated invar.

The voltage biasing will be performed in pre-set sequences from -500V to +500V, usually in increments of 25V. Each voltage level will be maintained for twenty seconds so that the array can attain steady state conditions.

4.1.2 Predictions

To predict the arcing rate of the biased arrays, the analytic arc rate method described in Section 2.1.2 is used. Table 4.1 shows the given and assumed cell properties necessary for the arc rate calculations. To determine C_{diele} and the offset of τ_{efee} due to the surface charge density (see Section 3.4), the numerical model must be run initially. Only the first scheme, the capacitance matrix method, is necessary to determine the polynomial fit for C_{diele} . Since the surface charge density is not incorporated into the analytic model, an offset of $\tau_{efee(numerical)}$ versus $\tau_{efee(analytical)}$ must be accounted for. The case chosen by Cho [3] closely matches the numerical and analytical τ_{efee} values. Since τ_{efee} versus βV curves have the same shape, the best technique is to determine the offset of each curve from the case that can be accurately predicted analytically. Therefore, the

Table 4.1: PASP Plus data used for arc rate predictions

Instrument No.	1, 2	3	4, 6	8	11	36
Cell Type	Si	Si WTC	GaAs/Ge	GaAs/Ge WTC	GaAs/Ge	APSA
Manufacturer	RCA	NASA	ASEC	Spectrolab	Spectrolab	TRW
Cell Size (cm ²)	2x4	8x8	4x4	4x4	4x4	2.6x5.1
No. of Cells	20, 60	4	20, 12	4	8	12
Cell Gap (μm)	500	1000	500	1000	500	635
d_{cell} (μm)	203	203	89	178	178	56
d_1 (μm)	153	203	102	152	152	51
d_2 (μm)	37	N/A	51	N/A	76	76
ϵ_{d_1}	3.5	4	4	4	4	4
ϵ_{d_2}	2.7	3	2.7	3	2.7	2.7
γ_{max_1}	3.46	4	4	4	4	4
γ_{max_2}	3	2	3	2	3	3
E_{max_1} (eV)	330	400	400	400	400	400
E_{max_2} (eV)	300	200	300	200	300	300
ϕ_w (eV)	4.76	4.85	4.26	4.5	4.26	4.26

entire numerical model is used at a specified voltage with the orbit integration scheme run for several β values, typically five, to determine this offset.

The orbital data for the analytical model requires a different approach. Since the orbit is neither circular nor of constant altitude, the orbital parameters must be determined for each point along the orbit at which the arc rate is to be calculated. The International Reference Ionosphere (IRI) program, developed at Goddard Space Flight Center in June 1987, can calculate the ambient density n_e , the electron temperature T_e , and the ion mass m_i if given the altitude, month, hour, sunspot number, and the geodetic coordinates. Since the exact time of the biasing is unknown, the parameters are averaged over the entire year by hour and by month. The times that gave the lowest and highest ambient densities are also used to define the lowest and highest arcing rates which might be observed. The variation due to different sunspot numbers is within the variation due to ambient densities. To determine the coordinates, as well as the altitude and orbital velocity, a separate calculation is necessary. Orbital mechanics are used to find the state vector in inertial coordinates of a given altitude. These are then converted to the earth-fixed coordinates. By using the orbit inclination, longitude of the ascending node and

the orbital eccentricity, the equations of motion can be integrated using a fourth-order Runge-Kutta method to obtain other positions along the orbit.

At altitudes higher than 1000km, the IRI model is useless for obtaining particle densities. At these altitudes, however, the following formula developed by Al'Pert [1] has been shown to agree well with experimental measurements:

$$n_e(z) = n_{e_o} \frac{z_o}{z} \exp \left[\frac{g_o M_o z_o}{2kT_{e_o}} \left[\frac{1}{1 + \frac{R_o}{z}} - \frac{1}{1 + \frac{R_o}{z_o}} + \ln \left(\frac{1 + \frac{R_o}{z}}{1 + \frac{R_o}{z_o}} \right) \right] \right]. \quad (4.1)$$

In this equation R_o is the Earth's mean radius, n_{e_o} is the electron density at 1000km, g_o is the gravitational acceleration at 1000km, M_o is the mass of hydrogen at 1000km, T_{e_o} is the electron temperature at 1000km, and z_o is the altitude of 1000km. Finally, the arc rate program requires the input of a range of electron densities. Since each voltage bias will be held for 20sec, the electron densities at either end of that range along the orbit are used to define the maximum and minimum densities expected.

For each array arc rates are predicted for voltages up to -500V in 25V increments at intervals of 600sec around the orbit. Near apogee, the spacecraft slows and the arcing rates have less variation due to the lower ambient densities so the intervals are increased to 1200sec.

The arc rate results for the conventional arrays are presented in Figs. 4.2-4.13. For each array, the first figure shows representative arc rates around the spacecraft orbit for the entire voltage range. Standard deviation error bars included on these figures are based on typically 100 calculations for each voltage. The arc rates at lower voltage biases are identical since τ_{fee} is dominant. The diverging curves at higher voltages indicate τ_{ion} is beginning to affect the arc rates. To distinguish the arc rates at these higher voltages, a second figure for each array shows all of the arc rate curves in the τ_{ion} range. As shown in Fig. 4.2, the arc rates for the silicon conventional array with 20 cells range from an average of 0.004sec^{-1} at 200V to 211sec^{-1} at 500V. At 500V bias, the arcing rates are as low as 8.75sec^{-1} , which is calculated at apogee. The addition of 40 more solar cells to the array increases the number of emission sites where arcing can occur, thus decreasing the time between arcs. This is clearly seen in Fig. 4.4, which shows that arcing begins at voltages as low as 175V for array #2. The highest arcing rate calculated is 366sec^{-1} at perigee for a voltage bias of 500V, while at apogee the arcing rate is 33sec^{-1} . For ASEC's GaAs/Ge array of 20 cells (#4), arcing is predicted at 125V, as shown in Fig. 4.6. Accordingly, the arcing rates are much higher at 500V, with a maximum of 1382sec^{-1} and a minimum of 50sec^{-1} . The slightly smaller array of only 12 cells (#6) is also predicted to experience arcing at 125V, but its arcing rates at 500V range from 918sec^{-1} to only

33sec⁻¹. The arc rate predictions, shown in Fig. 4.10, for Spectrolab's GaAs/Ge array of 8 cells are significantly lower than predictions for ASEC's GaAs/Ge array. Arcing is not predicted until 175V, and arc rates at 500V are at most 69sec⁻¹ (at perigee) and at least 15sec⁻¹ (at apogee). The thin APSA is predicted to experience arcing at the low voltage of 100V in the lower altitudes. The high arcing rates, however, are not nearly as high as for arrays #4 and #6. The lower arc rates are much higher, indicating a higher τ_{fee} , but the arc rates saturate around 300V by τ_{ion} . Consequently at 500V, the highest arc rate is predicted to be only 413sec⁻¹ and the lowest is predicted to be 15sec⁻¹.

To compare these results, Fig. 4.14 shows the arc rate predictions for each conventional array at perigee. The GaAs/Ge arrays and APSA only differ in τ_{fee} properties in dielectric thickness (See Table 4.1). As expected, the thin APSA has the highest arc rate predictions in the τ_{fee} -dominated range, with only 127 μ m dielectric thickness. Spectrolab's GaAs/Ge cells with 228 μ m thick dielectrics have the lowest predicted arc rates, and ASEC's GaAs/Ge cells with 153 μ m thick dielectrics are predicted to experience arcing of intermediate intensity. All of these arrays have silver-plated interconnectors, in contrast with the Kovar interconnectors of the silicon cells. From the arc rate sensitivity study of different interconnector work functions in Chapter 3, however, the difference in arc rates between these two metals is negligible (see Fig. 3.22). The silicon cells also have 190 μ m thick dielectrics, which is between the thicknesses of Spectrolab's GaAs/Ge cells and ASEC's GaAs/Ge cells. The predicted arc rates of the silicon arrays also fall between the arcing rates of those arrays, so the dielectric thicknesses must be the discriminating factor among all of the arrays for the range dominated by τ_{fee} . For the range dominated by τ_{ion} , the major difference between the arrays is the cell frontal area, A_{cell} . According to Eqn. 1.6 the smaller APSA cells increase τ_{ion} , thus decreasing the arc rate saturation level from that of the larger cells.

To predict the arc rates of the WTC cell arrays, an analytical model similar to the one for the conventional cell arrays should be used. This model has not yet been determined so the arc rate predictions for this cell design are left for future work.

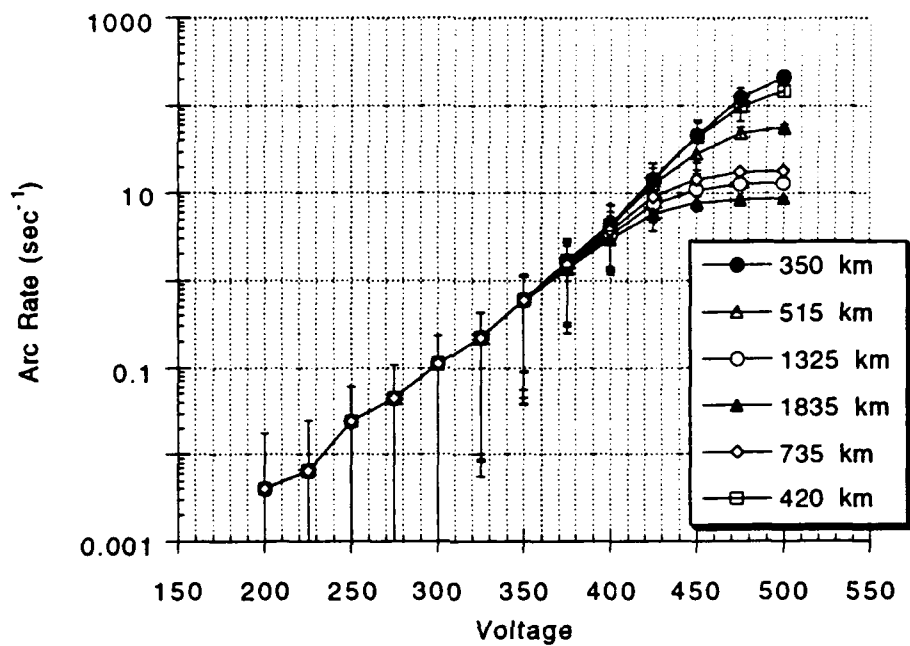


Figure 4.2: Selected arc rate predictions with standard deviation errors for Si conventional array #1

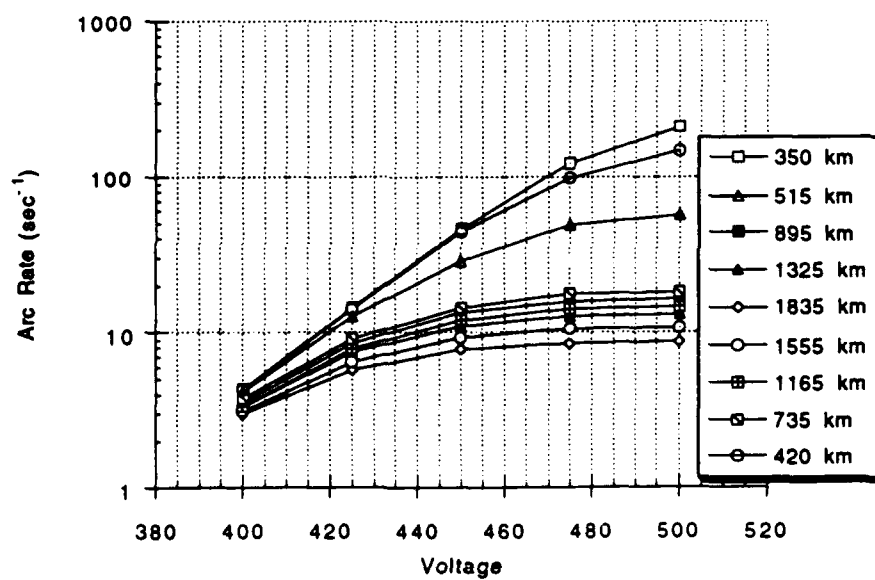


Figure 4.3: Complete arc rate predictions in the differentiating voltage range for Si array #1

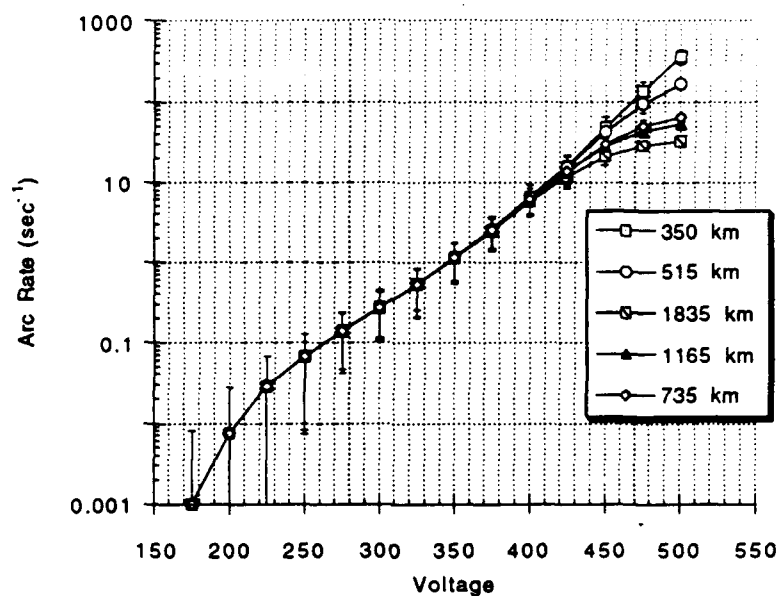


Figure 4.4: Selected arc rate predictions with standard deviation errors for Si conventional array #2

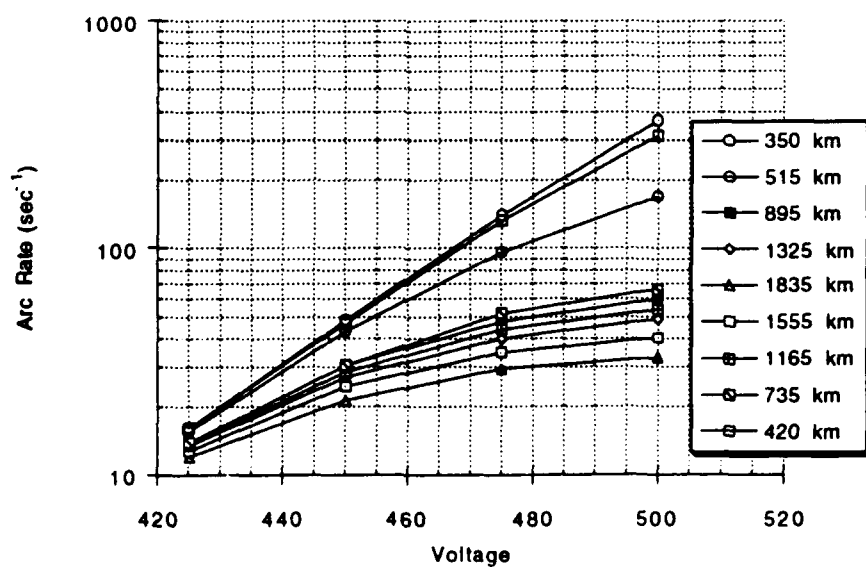


Figure 4.5: Complete arc rate predictions in the differentiating voltage range for Si array #2

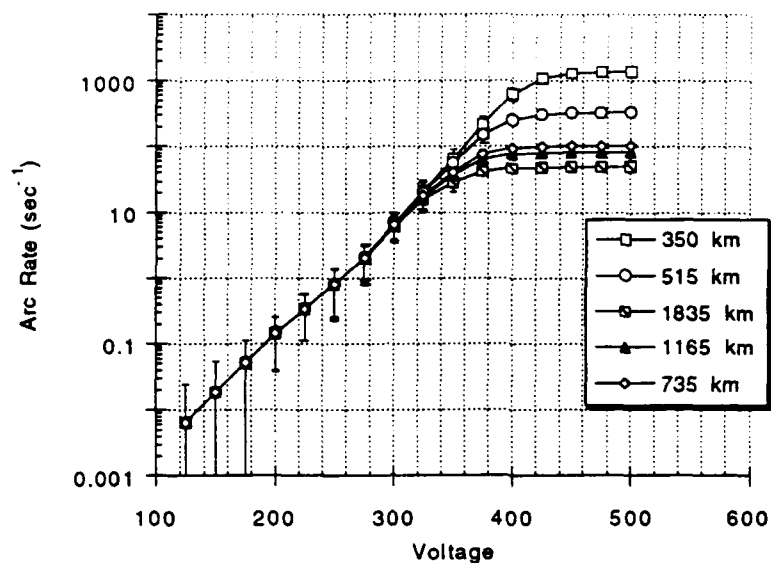


Figure 4.6: Selected arc rate predictions with standard deviation errors for GaAs/Ge conventional array #4

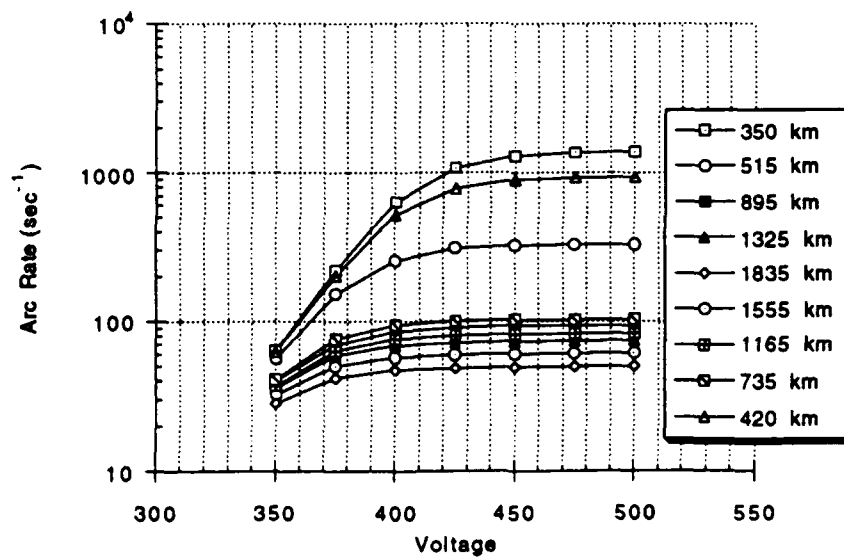


Figure 4.7: Complete arc rate predictions in the differentiating voltage range for GaAs/Ge array #4

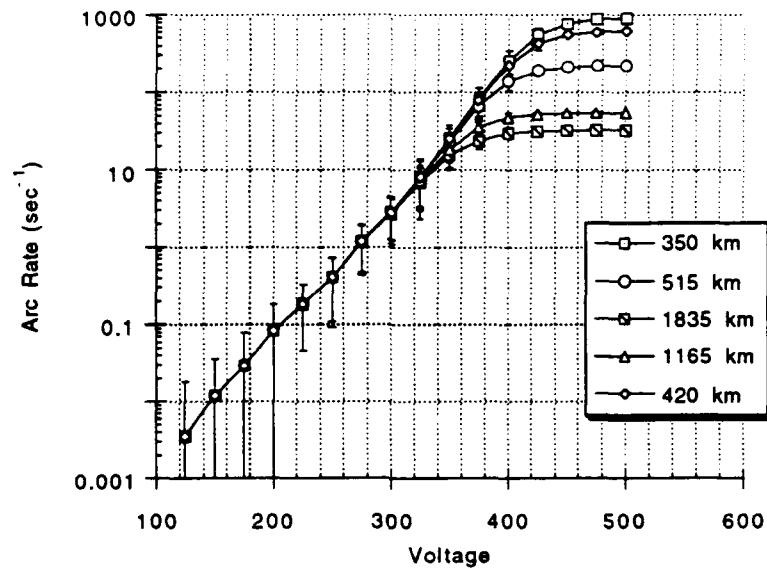


Figure 4.8: Selected arc rate predictions with standard deviation errors for GaAs/Ge conventional array #6

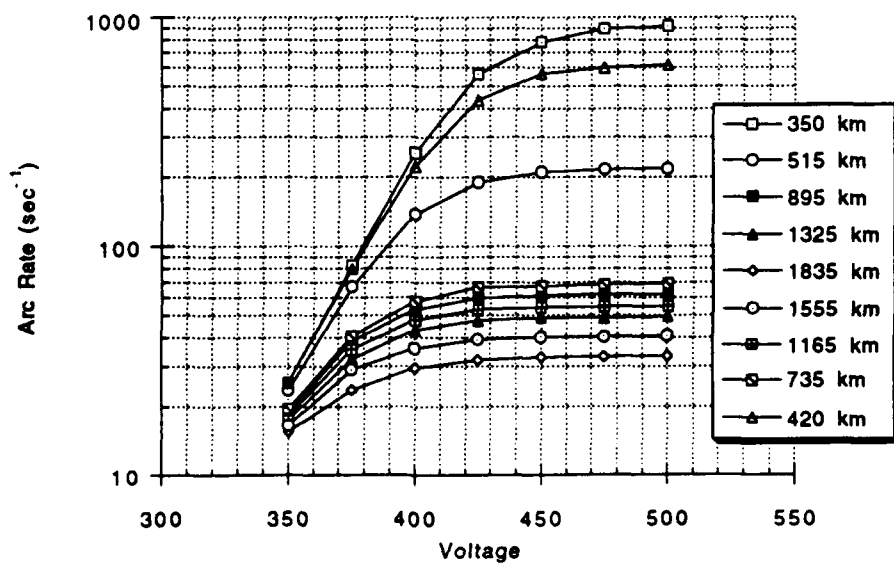


Figure 4.9: Complete arc rate predictions in the differentiating voltage range for GaAs/Ge array #6

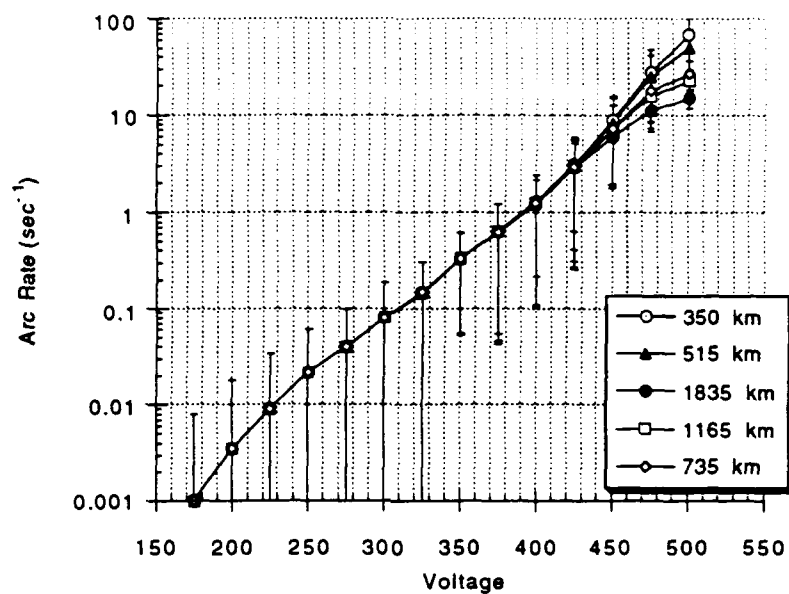


Figure 4.10: Selected arc rate predictions with standard deviation errors for GaAs/Ge conventional array #11

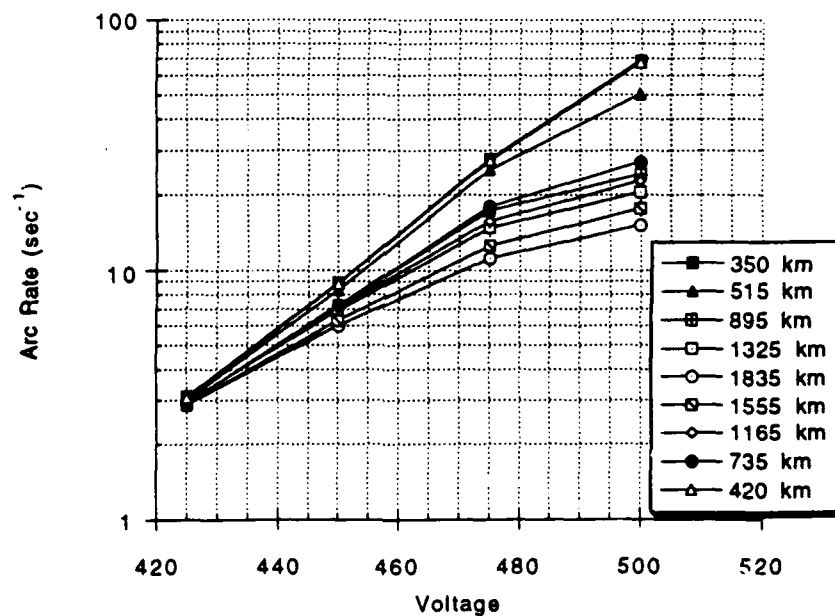


Figure 4.11: Complete arc rate predictions in the differentiating voltage range for GaAs/Ge array #11

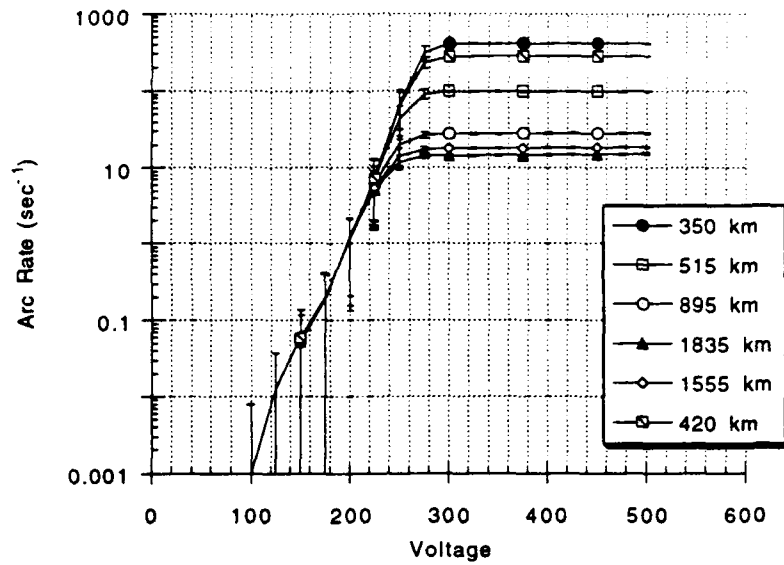


Figure 4.12: Selected arc rate predictions with standard deviation errors for APSA (#36)

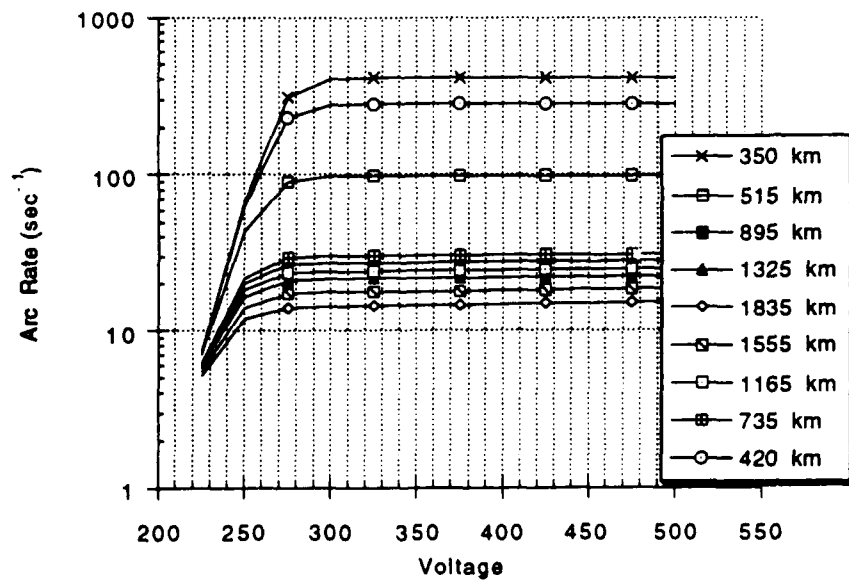


Figure 4.13: Complete arc rate predictions in the differentiating voltage range for APSA (#36)

4.2 SAMPIE

The Solar Array Module Plasma Interactions Experiment (SAMPIE) is designed to provide NASA with data on the interaction of high voltage space power systems with the ambient plasma environment of low earth orbit (LEO). The experiment will focus on the investigation of the arcing and current collection of typical materials and geometries likely to be a part of future high voltage power systems in LEO. The objectives SAMPIE is intended to accomplish, fully described in its Technical Requirements Document [12], are the following:

- (1) characterize arcing on selected solar cell technologies by determining the magnitude of the arc currents, the arc rates, and the arcing thresholds;
- (2) measure the collected plasma current versus the applied bias of these solar cell arrays;
- (3) test a pre-determined arc mitigation strategy for a selected solar cell design;
- (4) measure the current collection on simple metal/insulator geometries;
- (5) determine the dependence of arcing characteristics on the metal of the interconnector;
- (6) time permitting, study basic phenomena related to arcing and its effects such as arcing from pinholes in coated conductors, arcing from anodized aluminum typical of alloys and anodization processes being considered for large space structures, and sputtering and degradation of metals biased at high negative potentials;
- (7) characterize the space environment for use in data reduction and analysis; and
- (8) validate computer models.

4.2.1 Experiment Description

SAMPIE is to be carried on a shuttle flight currently scheduled for launch in early 1994. The layout of SAMPIE is shown in Figs. 4.15 [13]. This metal box will mount on one of the four top mounting positions of a Hitchhiker-M carrier, which is located in the shuttle bay. Most of the instruments are located inside the box. These include the electronics necessary for experiment control and data storage, a pressure gauge to measure background pressure, a langmuir probe to monitor plasma density and temperature, and a V-body probe to monitor the shuttle potential with respect to the ambient environment. The latter probe is crucial for determining the bias voltage since the power supply can only apply voltage with respect to the shuttle ground, which will shift during SAMPIE operations. In addition, the bias voltage needs to be with respect to the ambient en-

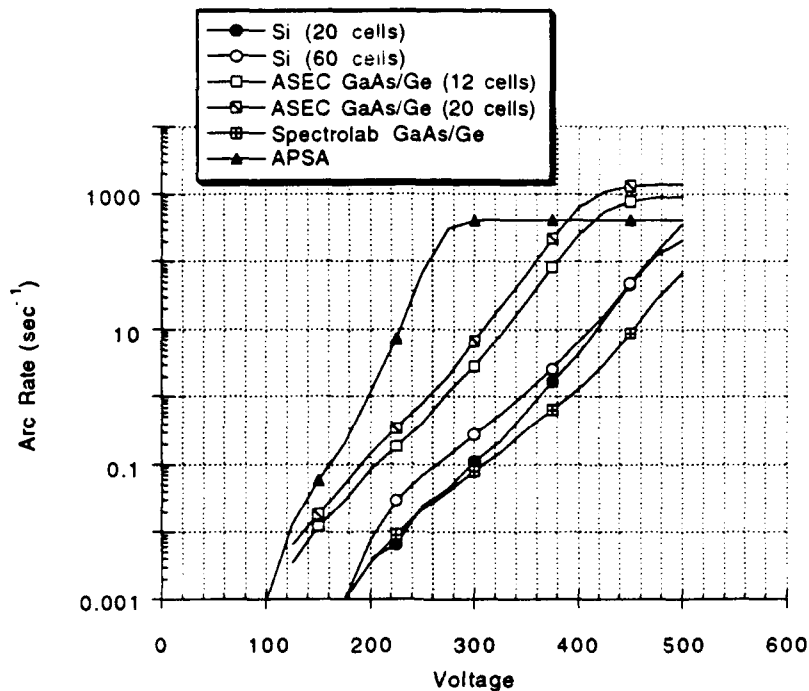


Figure 4.14: Arc rate prediction comparison for all PASP Plus conventional arrays at 350km

vironment so the actual voltages applied need only be determined with the data of the shuttle potential. This problem was accounted for in mission planning through extensive modelling, and it is expected that the offset of the ground will be in the range of 10 to 25V. A sun sensor to measure the incidence angle is located on top of the box along with the test modules.

A more detailed schematic of the positioning of the test modules on the experiment plate is shown in Fig. 4.16. Three solar cell designs have been chosen to accomplish objectives (1) and (2): the silicon conventional cells, a Space Station Freedom cell, and the Advanced Photovoltaic Solar Array (APSA). Two of the modified Space Station Freedom cells will test arc mitigation strategies to meet objective (3). The first will test the effect of creating an overhang of the coverglass over the 8mil silicon cell. The four exposed cell edges will have overhangs of 0, 4, 7, and 11mil respectively. The second modified SSF cell will have its excess adhesive removed in a special treating process to test the theory [10] that the arc discharge is actually a breakdown in water vapor desorbed from the adhesive. The third SSF cell will test the computer prediction that current collection is linear with exposed cell area. Multiple breakdown tests are designed to determine the effects on arcing due to the metal material. The five metals chosen are gold, silver, copper, aluminum, and tungsten. The first test consists of strips

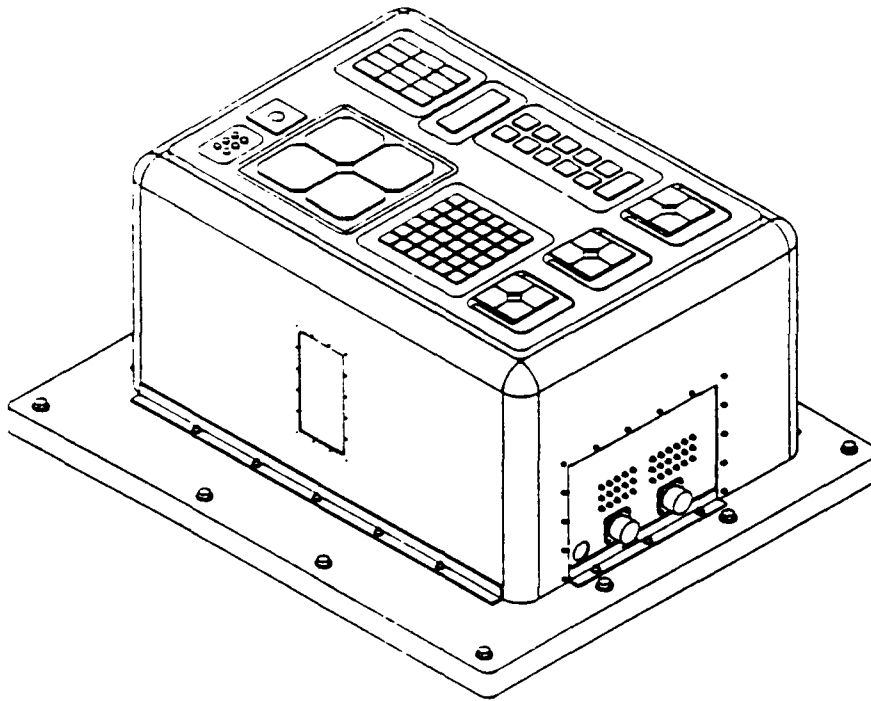


Figure 4.15: SAMPIE experiment package

of Kapton 1mil thick, 0.0625in wide, spaced 0.0625in apart on the metal. This simple metal/insulator configuration is typical of many space power applications including the solar cell/interconnector geometry. However, affixing the Kapton to the metal requires the use of an adhesive bond, which complicates the arc process. The second test was therefore designed to eliminate the dielectrics from the charging process. For these tests, a stainless steel rod of 1mm diameter is suspended 1mm above the metal surface. These rods are grounded, acting as anodes. Both tests are included as the first test is a better model of real space systems while the second test isolates the metal's effect on the arcing process. The three final experiments combine to fulfill objective (6). The first is included on the multiple breakdown coupon, though it is not designed to test arcing. This aluminum sample is coated with Z93, a thermal coating often applied to spacecraft which has been found to collect electrons when biased positively under some conditions. The second is the single breakdown test which will test a sample of anodized aluminum, currently planned for the SSF main structure, for dielectric breakdown and arcing at high voltage biases. The third is the snapover and current collection test. This includes 6 copper disks of 1cm diameter covered with Kapton 3mil thick. A pinhole is centered in the Kapton of each disk with hole sizes of 1-30mil.

The tests relevant to this research involve those concerning the actual solar cells: silicon conventional, SSF, and APSA. The silicon cells are 2cm×2cm, but otherwise are

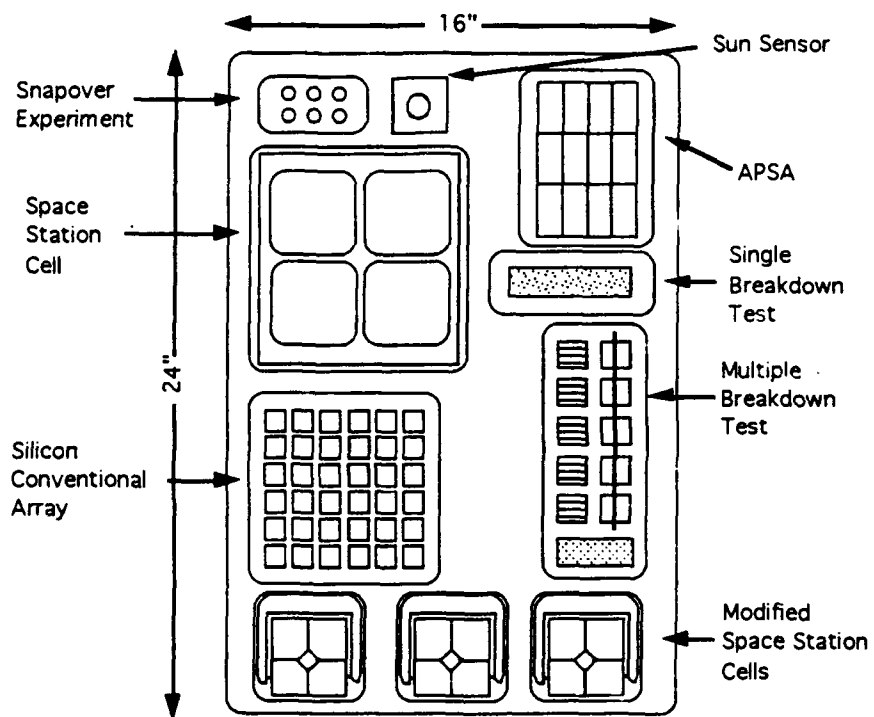


Figure 4.16: SAMPIE experiment plate layout

assumed to have the same characteristics as the PASP Plus cells in arrays #0-2. These cells are planned to be used for 3 different tests, only one of which involves arcing. In this test, only the four innermost cells will be used. The SSF cell is again 8cmx8cm, and the APSA includes twelve 2cmx4cm cells. The material properties of these cells are described in Section 4.1.1 and tabulated in Table 4.1.

The entire space experiment is expected to be completed during 12 hours facing the ram velocity and 6 hours facing the wake. Each sample will be biased individually while all others are held at the ground potential. The power supply will bias the solar cell samples from 0 to -600V for the arcing tests. The bias time varies significantly with the voltage since the arc rate is known to increase substantially as the bias voltage becomes more negative. The experiment times are expected to be the following: 40min (2400sec) at -120V; 20min (1200sec) at -150V; 5min (300sec) at -180V; 2min (120sec) at -210V; 60sec at -240V, -270V and -300V; 30sec at -400V; 5sec at -500V; and 2sec at -600V.

4.2.2 Predictions

Arc rate predictions for SAMPIE are determined in the same manner as for the PASP Plus predictions. The analytical model discussed in Section 2.1.2 is again used for the conventional cell arrays, and the IRI model also is used to determine the ionospheric conditions necessary for the analytical model. The shuttle orbit is assumed to be circular with an altitude of 250km and an inclination of 28.5°.

The arc rate predictions for the silicon conventional array and APSA are shown in Fig. 4.17. Arcing is not predicted until the 210V step for the silicon array, but the thin APSA is expected to experience arcing at 120V. These arc rate curves have the general characteristics of the two dominating regions of τ_{free} and τ_{ion} ; however, the curves are not as smooth due to the irregularity of the voltage and time intervals. The arc rates are also significantly lower at the higher voltages than those predicted for the PASP Plus experiment. This is mostly due to the much shorter experiment time of only a few seconds compared to the 20sec experiment time of the PASP Plus tests. In addition, only 4 silicon cells are used for arc rate measurements in this experiment compared to the 20 and 60 cells of the PASP Plus silicon arrays.

The arc rate predictions for the SSF cell is left for future work. These predictions can be made from an analytical model developed from the results of the numerical model presented in Section 2.2, with experimental results used for model verification.

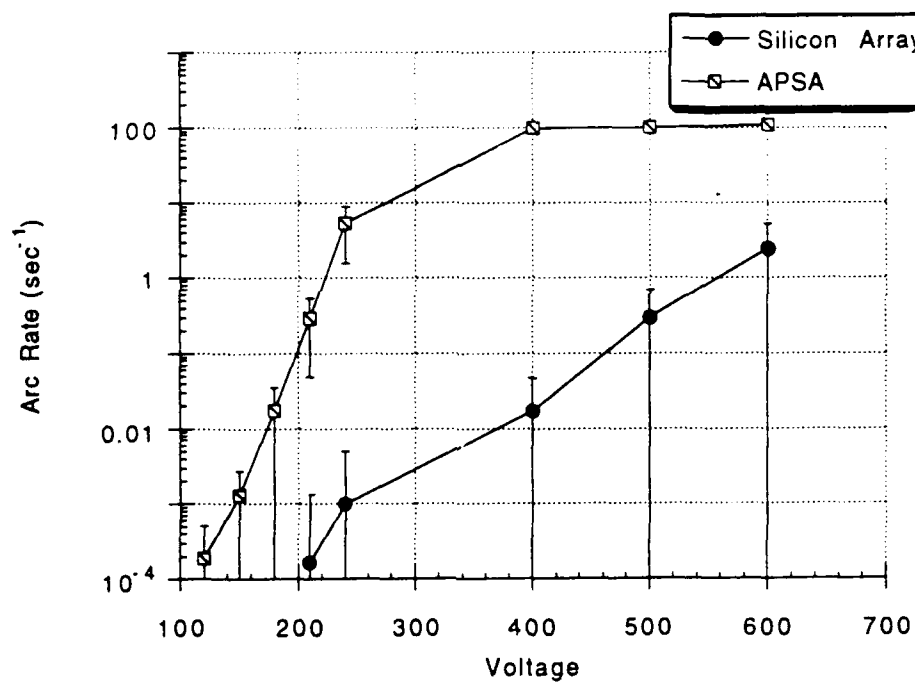


Figure 4.17: SAMPIE arc rate predictions with standard deviation error bars for the silicon conventional array and APSA

Chapter 5

Conclusions

The emergence of high voltage solar arrays has been driven by recent space system designs which require high power levels. Consequently, only recently has the negative interaction of arcing on high voltage solar arrays in low earth orbit been a concern. Since arcing can eventually destroy solar cells, it is imperative to investigate methods to reduce or even eliminate it as well as to develop methods to predict it for existing solar cells which might be used on future high voltage solar arrays. This research has addressed both of these needs.

5.1 Summary of Results

All of the research presented in this thesis has been based on the numerical and analytical models discussed in Chapter 2. These models accounted for the ambient ion charging and enhanced electron field emission (EFEE) charging processes which were previously determined to be the two main factors leading to arc initiation. The numerical model simulates this arc initiation process by integrating the particle trajectories self-consistently with the dielectric surface charge. Electrons emitted from the conductor that hit the dielectric surface released secondary electrons, creating a positive surface charge which further enhances the electric field at the triple junction. With an EFEE charging site on the conductor near the triple junction, the exponential dependence of the EFEE current on the electric field causes the electric field to run away. This gives rise to arc initiation. The analytical model represents the time to arc initiation by the sum of the ambient ion charging time and the EFEE charging time. The numerical model was also modified to represent the wrap-through-contact geometry using the same charging processes. The electric field runaway, signifying arc initiation, occurs at the triple junction including the semiconductor and the coverglass. Two different dielectric charging behaviors are exhibited for relatively low and high field enhancement factors.

The models for conventional solar cells were used to determine methods of arcing mitigation in Chapter 3. Based on the analytical model, five cell properties were varied to determine their effect on the arc rate: the coverglass and adhesive dielectric thickness, the interconnector work function, the secondary electron yield, the ratio of the dielectric constants, and the length of the coverglass overhang above the interconnector. The dielectric thickness was found to affect the arc rate, but significant reduction could only be attained by large thicknesses which would be costly in mass addition. The interconnector work function did not affect the arc rate much for typical metals, though very high work functions decreased the arcing rates and very low work functions increased the arcing rates at lower voltages. Secondary electron yields below unity eliminated arcing since the electric field could not run away; yields just above unity, however, did not reduce the arc rate significantly. Coverglass to adhesive dielectric constant ratios of less than unity caused the surface charge near the triple junction to remain negative for a considerably long time, thus significantly reducing the arcing rates. Overhanging the coverglass above the interconnector also caused the dielectric surface to charge negatively if the overhang was longer than the critical overhang. Overhangs less than the critical overhang only acted as thicker dielectrics with no negative surface charging. Shorter overhangs did not affect the arc rate much, but longer overhangs significantly reduced arcing rates. Therefore, arcing rates can be best reduced by increasing the dielectric thicknesses, selecting dielectric materials with coverglass to adhesive dielectric constant ratios near unity, and overhanging the coverglass above the interconnector. Dielectric secondary electron yields lower than unity will eliminate arcing at all voltage biases.

Arcing rates for actual solar cells were predicted in Chapter 4 for two near future space experiments, Photovoltaic and Space Power Plus Diagnostics (PASP Plus) experiment and the Solar Array Module Plasma Interactions Experiment (SAMPIE). Using the numerical and analytical models, the high voltage biased conventional cell arrays were studied. The most significant factors which discriminated the arcing rates in the EFEE charging-dominated voltage range were the cell thickness and number of cells in the array. As expected from the sensitivity scans, the cells with thinner dielectrics had higher arcing rates at the low voltages. In addition, the increased number of EFEE emission sites due to a higher number of cells increased the arcing rates.

5.2 Recommendations for Future Work

The numerical model for wrap-through-contact (WTC) cells should be involved in future work. The model should be used to investigate the effects of different properties on the EFEE charging time and to further study the two different charging behaviors seen. A modified orbit integration scheme might be necessary to determine EFEE charging times longer than 10^{-3} sec. To be successful, this may require a re-evaluation of the timestep calculation. Also, an analytical model for WTC cells based on numerical and experimental work would be very useful, particularly for future designs. With both numerical and analytical models, mitigation strategies other than overhanging the coverglass could be studied. When experimental data becomes available, the charging times and processes can be compared to determine any necessary modifications. The PASP Plus and SAMPIE missions should provide data for various types of WTC cells as well as for various coverglass overhang lengths for the Space Station Freedom cell.

For arc rate mitigation on conventional solar cells, experimental work should be done to confirm the results of this research and to develop optimum cell designs for high voltage solar array operation. This work should include tests of different coverglass overhang lengths, which would confirm the critical overhang length hypothesis, and tests of different coverglass to adhesive dielectric constant ratios to determine the effects of material choice on the arc rate. In addition, doping procedures could be used to reduce the dielectric secondary electron yield below unity to test the hypothesis of no arc discharge under these conditions. From these tests, a solar cell could be designed to optimize the mass, efficiency, and arcing rate trade-off.

The arc rate predictions for the PASP Plus and SAMPIE will be useful in verifying and possibly improving the numerical and analytical models. Since these experiments will be launched in the next year or two, data will soon be available to compare with the predictions presented in this thesis. Of particular interest should be whether the modifications used to account for the surface charge density variations were necessary and whether the assumed value for β_o is always near 200. The latter is noted since in Ref. [2] Cho indicated that this value was the only variable of freedom but it had to be chosen in each case to match the slope of the arc rate curve in the lower voltage region. Additional research with the aid of the experimental results should be able to determine these points.

Bibliography

- [1] YA. L. Al'Pert. *The Near-Earth and Interplanetary Plasma*. Vol. 1, Cambridge University Press, 1983, pp. 22-24.
- [2] M. Cho, "Arcing on High Voltage Solar Arrays in Low Earth Orbit: Theory and Computer Particle Simulation," Ph.D. Thesis, M.I.T., 1992.
- [3] M. Cho and D. E. Hastings, "Dielectric Charging Processes and Arcing Rates of High Voltage Solar Arrays", *Journal of Spacecraft and Rockets*, Vol. 28, pp. 698-706, 1991.
- [4] Ferguson D. C., "The Voltage Threshold for Arcing for Solar Cells in LEO-Flight and Ground Test Results", NASA TM-87259, March 1986.
- [5] H. Fujii, Y. Shibuya, T. Abe, K. Ijichi, R. Kasai, and K. Kuriki, "Laboratory Simulation of Plasma Interaction with High Voltage Solar Arrays", *Proceedings of the 15th International Symposium on Space Technology Science*, Kanagawa, Japan, 1986.
- [6] N. T. Grier and N. John Stevens, "Plasma Interaction Experiment (PIX) Flight Results", *Spacecraft Charging Technology 1978*, NASA CP-2071, pp. 295-314.
- [7] N. T. Grier, "Plasma Interaction Experiment II: Laboratory and Flight Results", *Spacecraft Environment Interactions Technology Conference*, 1983, NASA CP-2359, pp. 333-348.
- [8] O. Hachenberg and W. Brauer, "Secondary Electron Emission from Solids", *Advancement in Electronics and Electron Physics*, Vol. 11, pp. 413-499, 1959.
- [9] D. E. Hastings, M. Cho, and H. Kuninaka, "The Arcing Rate for a High Voltage Solar Array: Theory, Experiments and Predictions", *Journal of Spacecraft and Rockets*, Vol. 29, pp. 538-554, 1992.
- [10] D. E. Hastings, G. Weyl and D. Kaufman, "The Threshold Voltage for Arcing on Negatively Biased Solar Arrays", *Journal of Spacecraft and Rockets*, Vol. 27, pp. 539-544, 1990.

- [11] B. G. Herron, J. R. Bayless and J. D. Worden, "High Voltage Solar Array Technology", *Journal of Spacecraft and Rockets*, Vol. 10, pp. 457, 1973.
- [12] G. B. Hillard and D. C. Ferguson, "The Solar Array Module Plasma Interaction Experiment: Technical Requirements Document", NASA TM-105660, 1992.
- [13] G. B. Hillard and D. C. Ferguson, "The Solar Array Module Plasma Interactions Experiment (SAMPIE): Science and Technology Objectives", to be published in the *Journal of Spacecraft and Rockets*.
- [14] R. W. Hockney and J. W. Eastwood. *Computer Simulation Using Particles*. McGraw-Hill, USA, 1981.
- [15] G. T. Inouye and R. C. Chaky, "Enhanced Electron Emission from Positive Dielectric/Negative Metal Configurations on Spacecraft", *IEEE Trans. Nuc. Sci.*, Vol. NS-29, No. 6, December 1982, pp. 1589-1593.
- [16] G. A. Jongeward, I. Katz, M. J. Mandell and D. E. Parks, "The Role of Unneutralized Surface Ions in Negative Potential Arcing", presented at the 1985 IEEE 22nd Annual Conference, NSRE.
- [17] R. V. Latham, *High voltage Vacuum Insulation: The Physical Basis*. Academic Press, London, England, 1981.
- [18] R. V. Latham, "Prebreakdown Electron Emission", *IEEE Transactions on Electrical Insulation*, Vol. EI-18, June 1983.
- [19] P. Leung, "Characterization of EMI Generated by the Discharge of a 'Volt' Solar Array", Technical Report CR-176537, NASA, November 1985.
- [20] "PASP Plus Experiment Specification," Phillips Laboratory, US Air Force, Jan 17, 1991.
- [21] D. E. Parks, G. Jongeward, I. Katz and V. A. Davis, "Threshold-Determining Mechanisms for Discharges in High-Voltage Solar Arrays", *Journal of Spacecraft and Rockets*, Vol. 24, pp. 367-371, 1987.
- [22] D. B. Snyder, "Discharges on a Negatively Biased Solar Cell Array in a Charged Particle Environment", *Spacecraft Environment Interactions Technology Conference*, 1983, NASA CP-2359, pp. 379-388.
- [23] D. B. Snyder and E. Tyree, "The Effect of Plasma on Solar Cell Array Arc Characteristics", Technical Report TM-86887, NASA, 1985.

- [24] N. J. Stevens, "Review of Interactions of Large Space Structures with the Environment, Space Systems and their Interactions with Earth's Space Environment", Progress in Aeronautics and Astronautics", Vol. 71, AIAA, Washington D. C., pp. 437-454, 1980.
- [25] H. Thiemann and K. Bogus, "Anomalous Current Collection and Arcing of Solar-Cell Modules in a Simulated High-Density Low-Earth-Orbit Plasma, ESA Journal, Vol. 10, pp. 43-57, 1986.
- [26] H. Thieman, R. W. Schunk and K. Bogus, "Where do negatively biased solar arrays arc?", Journal of Spacecraft and Rockets, Vol. 27, pp. 563-565, 1990.